Winter 2019

Microchannel Plates in Mass Spectrometer Instruments for Spacecraft

Nicholas Kenneth Lubinsky
University of New Hampshire, Durham

Surface Response and Applications of Microchannel Plates in Mass Spectrometer Instruments for Spacecraft

December 19, 2019

BY

Nicholas K. Lubinsky

B.S. in Physics, Renssalaer Polytechnic University, 2012

Dissertation

Submitted to the University of New Hampshire

in Partial Fulfillment of

the Requirements for the Degree of

Doctor of Philosophy

in

Physics

December, 2019

This thesis/dissertation was examined and approved in partial fulfillment of the requirements for the degree of Doctor of Philosophy in Physics by:

Dissertation Director, Harald A. Kucharek
Research Professor of Physics

Lynn M. Kistler
Professor of Physics
Director of Space Science Center

James M. Ryan
Professor of Physics

Mark L. McConnell
Professor of Physics

Karsten Pohl
Professor of Physics
Physics Department Chair

On August 30, 2019

Original approval signatures are on file with the University of New Hampshire Graduate School.

Acknowledgments

I'd like to thank each member of my committee for keeping this wild train ride on course: Harald Kucharek, Lynn Kistler, James Ryan, Karsten Pohl, and Mark McConnell.

My stint in graduate school would not have been possible without the help of my friends and co-students within the Physics Department and beyond. David Hilton, Anthony Saikin, Sambid Wasti, Tyler Bennett, Jason Schuster, Cristian Ferradas, Banafshe (Bashe) Ferdosi, Shan Wang, Gen Li, Philip Quinn, Thomas Fenton, Nick Ferreri.

I'd like to extend my thanks to the project help given from Zain Abbas, Philip Diffley, Mark Popecki, and Cole Hamel. The project wouldn't have been possible without the whole engineering staff onboard with the projects: Stan Ellis, Todd Jones, John Gaidos, Chris Bancroft, Mark Granoff, Phil Demaine, and Aaron Bolton.

Finally, all this work was made possible under the High Res. Mass Spectrometer NASA Grant #NNX14AJ30G. Additional support was given in NASA Space Grant NIFs funded through The New Hampshire Space Grant Consortium, Grant #NNX15AH79H.

Contents

List of Figures

List of Tables

Nomenclature

ALD Atomic Layer Deposition

AMPTE Active Magnetospheric Particle Tracer Explorer

CIS Cluster Ion Spectrometry

CODIF Ion Composition and Distribution Function analyzer

CoM Center of Mass Frame

ESA Electrostatic Analyzer

FAST Fast Auroral Snapshot Imager

HPCA Hot Plasma Composition Analyzer

L/D Ratio Length to Diameter Ratio

MCP Microchannel Plate

MHD Magnetohydrodynamics

MMS Magnetospheric Multiscale Mission

PAC Post Acceleration Voltage

SEY Secondary Electron Yield

SMS Suprathermal Mass Spectrometer

SRIM/TRIM Stopping and Range of Ions in Matter / Transport of Ions in Matter

TOF Time of Flight

Microchannel Plates in Mass Spectrometer Instruments for Spacecraft

BY

Nicholas K. Lubinsky

Advisor: Harald Kucharek Coadvisor: Lynn Kistler

University of New Hampshire, December, 2019

Abstract

Earth's magnetosphere contains plasma originating both from the solar wind and from the ionosphere. While H^+ is the dominant ion from both sources, the solar wind contains high charge state ions such as He^{++}, and O^{6+}, while the ionosphere contributes singly ionized heavy ions including He^+, N^+ and O^+. Measuring the composition gives information on the source and mass dependent entry, heating and acceleration mechanisms. However, most ion composition instruments are not able to clearly distinguish between some of the heavy ions involved in these processes, particularly N^+ and O^+. This thesis aims to test a new design of a Time-of-Flight mass spectrometer that should improve the mass resolution by reducing scattering. In this new design, the carbon foil that is normally used to generate a "Start" signal is replaced by a single straight-channel Microchannel Plate (MCP). These changes are implemented in the engineering copy of the Ion Composition and Distribution Function analyzer (CODIF) instrument, allowing us to investigate the effects of the change on spectra and flux for different MCP geometries as well as different thin film coatings. We demonstrate that all tested MCP geometries with or without coatings significantly reduce the energy lost from the ion when compared against the carbon foil, but only for ions heavier than carbon; this improves separation of the heavier ion species close in mass, characterized by the transit time of the Gaussian-distributed centroid in time and the Full Width Half

Max of the spectra. Geometry effects are the most significant, with the narrower pores having the largest reduction in energy transferred from the ion. However, MCP response is heavily dependent on impinging angle and comes at the cost of severely decreased ion flux for the narrower pore sizes. Thin film coatings of Al_2O_3 on the MCPs result in smooth surfaces that increase the probabilities of specular reflection occurring and reduce the energy required to emit an electron, resulting in slightly increased scattering while improving the detection efficiency. Additionally, the instrument using MCPs can accurately determine mass at energies far lower than where the carbon foil's energy losses cause the spectra to be too broad to be distinguished. This demonstrates that an MCP-based instrument would not require a Post Acceleration voltage (PAC). Results from this work culminate in a future detector design, capitalizing on the advantages offered by the MCP and carbon foils.

1 Introduction

Plasma streaming off the sun or energized in Earth's upper atmosphere faces a complex slew of magnetohydrodynamic mechanisms that affect both the plasma fluid equation of state, as well as the dynamics of the geomagnetic field. Differences in relative composition of this plasma directly affect the overall geomagnetic structure, causing perturbations in both magnitude and redistribution of energy[37, 35]. Motion of the plasma and its interactions with terrestrial magnetic fields act to perturb the magnetic field equilibrium, and give rise to phenomena like geomagnetic storms, aurorae, etc. while the large scale structure this forms is called the magnetosphere.

The magnetosphere around Earth contains plasma from two sources: the solar wind, or the ionosphere. Solar wind particles are injected into the magnetosphere from magnetic reconnection events. Originating directly from the sun, this plasma contains very high charge states like O^{6+}, indicative of the source region temperature. Competing with the solar wind source are ionospheric particles, which are particles ionized in the upper atmosphere and subsequently swept up by the presence of electromagnetic forces[77, 37]. For plasma in the energy range typical of this region, accurate determination of mass per charge allows for the investigation of the origins of the different ion constituents, particularly these sources. By extension, this means the mass dependent heating and acceleration mechanisms can be distinguished between these two prominent plasma sources. At present, the available studies capable of distinguishing nitrogen from oxygen are limited, with most instruments flown being unable to make this distinction due to design.

1.1 Magnetospheric Science Overview

The interplanetary space in our solar system is home to a constantly changing magnetized plasma environment, host to a multitude of phenomena that collectively govern the dynamic system. Charged particles constantly stream off the corona of the sun, and is known as the

solar wind. Solar wind is constituted predominantly of protons and electrons, but alpha particles are also present to an extent, along with trace amounts of heavier elements. Due to the effects of flux freezing, the constant stream of charged particles carries the interplanetary magnetic field (IMF) along with it. Interactions between the solar wind and Earth's magnetic field forms a region around Earth where the Earth's magnetic field becomes dominant; this is called the magnetosphere[41].

The plasma that concerns us the most is that within the Earth's magnetosphere. The magnetosphere is a complicated system with a strange topology, distorted magnetic fields, currents and significant electric fields, all of which will affect particular ions differently. The magnetosphere is constantly being distorted and varies due to the highly dynamic solar wind environment, which subsequently generate geomagnetic storms.

Interactions between the solar wind and the interstellar medium form the heliosphere. Solar wind's magnetized plasma interacting with the (respective) planet's magnetic fields gives rise to magnetospheric structures. Interactions between the heliosphere and the magnetosphere couple down to the planet's upper atmosphere environment (the ionosphere), which induce electromagnetic currents and radiation to compensate[41, 46, 95, 101]. With the high variability of both the Earth's upper atmosphere and the local solar wind, the resulting magnetospheric environment is complex and volatile.

Magnetohydrodynamics (MHD), which treats the bulk plasma as a magnetized fluid constituted of the different ions and electron populations, currently best describe the interactions of the bulk magnetosphere plasmas. Subsequently, the MHD equations of state depend heavily on the respective ion population mass and number densities; any one dominant ion population significantly governs the available mechanisms of energy redistribution, and transport of ions[37].

1.1.1 Magnetospheric Interactions

A magnetospheric cavity structure forms when the pressure exerted by solar wind becomes balanced by the magnetic pressure exerted from the Earth. The solar wind pressure is time dependent due to the processes within the sun. Planetary magnetic fields in the solar system remain relatively constant but perturbed, so as the solar wind exerts more pressure on the magnetosphere, the boundary location and shape moves inward to where the combined plasma pressure and magnetic pressure from the magnetosphere reach equilibrium[41].

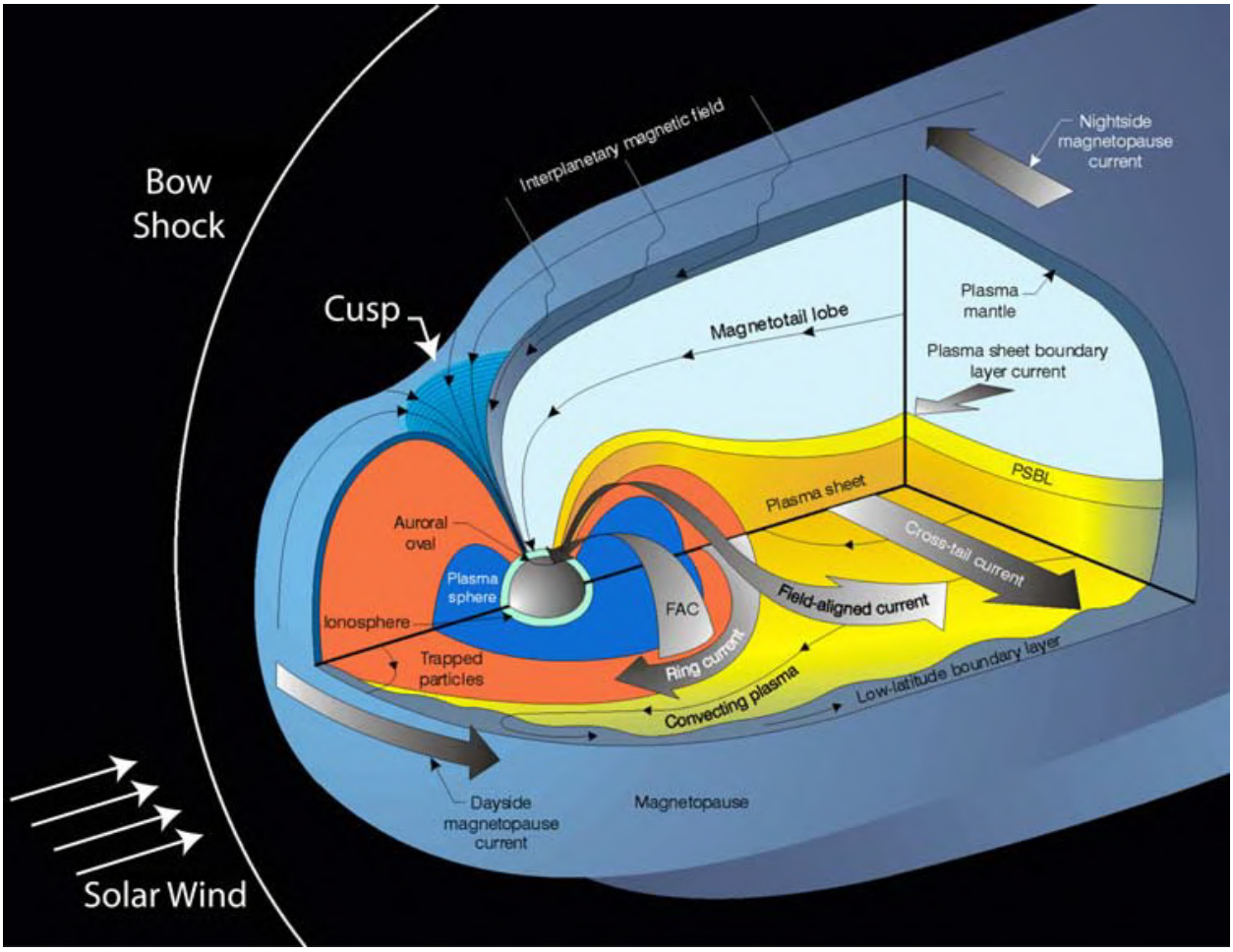

Figure 1.1: Diagram of Earth's magnetospheric cavity. Plasma interactions with the magnetic field give rise to a highly complex structure comprised of many different regions.Adapted from McCollough et al. (2008).

Basic cavity structure of the magnetosphere is depicted in Figure 1.1. As can be seen, it is a complex and dynamic cavity, producing many different sub-regions of interest. As solar

wind approaches the Earth, the plasma fluid is slowed from supersonic speeds (~ 450 km/s) by the exerted magnetic pressure originating from the Earth's dipole magnetic field. Once the solar wind plasma slows to subsonic speeds, a collisionless shock is formed due to the low densities and large mean free paths between collisions involved[41, 36]. Now slowed, the solar wind plasma continues Earthward, through a region named the magnetosheath, which is bounded on both ends by the bow shock, and the magnetopause. The magnetopause marks a distinct boundary where the ram pressure of the solar wind is balanced by the magnetic pressure from the Earth's magnetic field. As this relies on the pressure balance with the constantly fluctuating solar wind ram pressure, the boundary constantly fluctuates and undulates.

Planetary magnetic field lines and their magnitudes severely inhibit solar wind plasma from penetrating the magnetopause, and as a result a current sheet is formed in the magnetosheath as the electron and ion fluid is deflected around the planet. Within the Earth-side of the magnetopause, the magnetosphere develops a complex internal structure. Some regions of interest in current studies include the plasmasphere, plasma sheet, and magnetotail.

The plasmasphere is the region extending from the planet's ionosphere, up to about $7R_E$ (Earth radii) and bounded by the plasmapause. This region also encompasses another structure scheme: the ring current. Ring current consists of an energetic plasma comprised of electrons and ions, each drifting about the Earth's equator in opposite directions. Ranging from about $2-7R_E$, this ring current is exposed to the forces of curvature drift and gradient drift stemming from the Earth's non-homogeneous magnetic field. Due to these effects, positive ions travel westward, while electrons travel eastward. Within the ring current are typically two radiation belts. One is the inner ring, containing highly energetic ($\sim 100 - 700\,keV$) electrons and ($\sim 10 - 100\,MeV$) protons from approximately $1.2 - 2.5\,R_E$. Then, the outer ring consists of primarily relativistic electrons ($\sim 0.1 - 10\,MeV$) around $4 - 8\,R_E$[17, 31]. Large scale convection of the plasma sheet occurs due to the presence of a significant electric field. During times of highly disturbed geomagnetic fields, the plasma originating from the

plasma sheet can be injected into the ring current[47]. Current research suggests this region is also populated by ions able to escape the gravitational pull of Earth, originating in the upper ionosphere[31, 17].

At the boundaries between the heliosphere and magnetosphere are flux tubes of magnetic field lines undergoing reconnection. Magnetic reconnection is not currently well understood, yet it is a significant source of particle injection and energization within the Earth's magnetosphere as it provides the main means in which these distinct plasma environments can exchange mass, momentum, and energy. In some cases, the imparted energy can accelerate particles to near the speed of light[9, 93, 92].

Finally, the magnetotail and plasma sheet are intertwined. The magnetotail is comprised of two large bundles of nearly parallel magnetic field lines, called magnetotail lobes. One is located north of the equatorial plane, and one is south of the plane. Density of particles in each of these lobes are very small; this observation and some *in-situ* measurements of magnetic fields determined these field lines actually connect with those of the solar wind and interplanetary magnetic field. The two lobes are separated by the plasma sheet, which is fed from both of these lobes. Plasma within this sheet varies in energy, but consist of hot plasma around $5-10\,keV$ for ions and $1-5\,keV$ for electrons. Earthward convection occurs from the diffuse magnetic fields and local electric potential, and can be injected into the ring current. Magnetic reconnection on the dayside and nightside of Earth further resupply the sheet with solar wind ions[41]. Consequently, this plasma sheet is a direct source of hot ions being injected into the magnetosphere.

1.1.2 Ionospheric Dynamics

The Earth's ionosphere is a dynamic region of the upper atmosphere, encapsulating a region of ionized particles from approx. 60 km to 1,000 km above the Earth's surface, and forms the innermost edge of the magnetosphere. Figure 1.2 depicts the general ionospheric dynamics involved. Higher latitudinal magnetic field lines extend out into the magnetosphere and

eventually connect to those emanating from the sun, which is particularly significant during magnetic reconnection events. Due to the Lorentz force experienced by the plasma, particles flow along the magnetic field lines. Boundaries at the dayside magnetosphere as well as the magnetotail require termination in a closed electric circuit; the ionosphere completes this circuit of the solar wind-magnetosphere system with Birkeland Field-Aligned Currents (FAC) and Pedersen Currents.

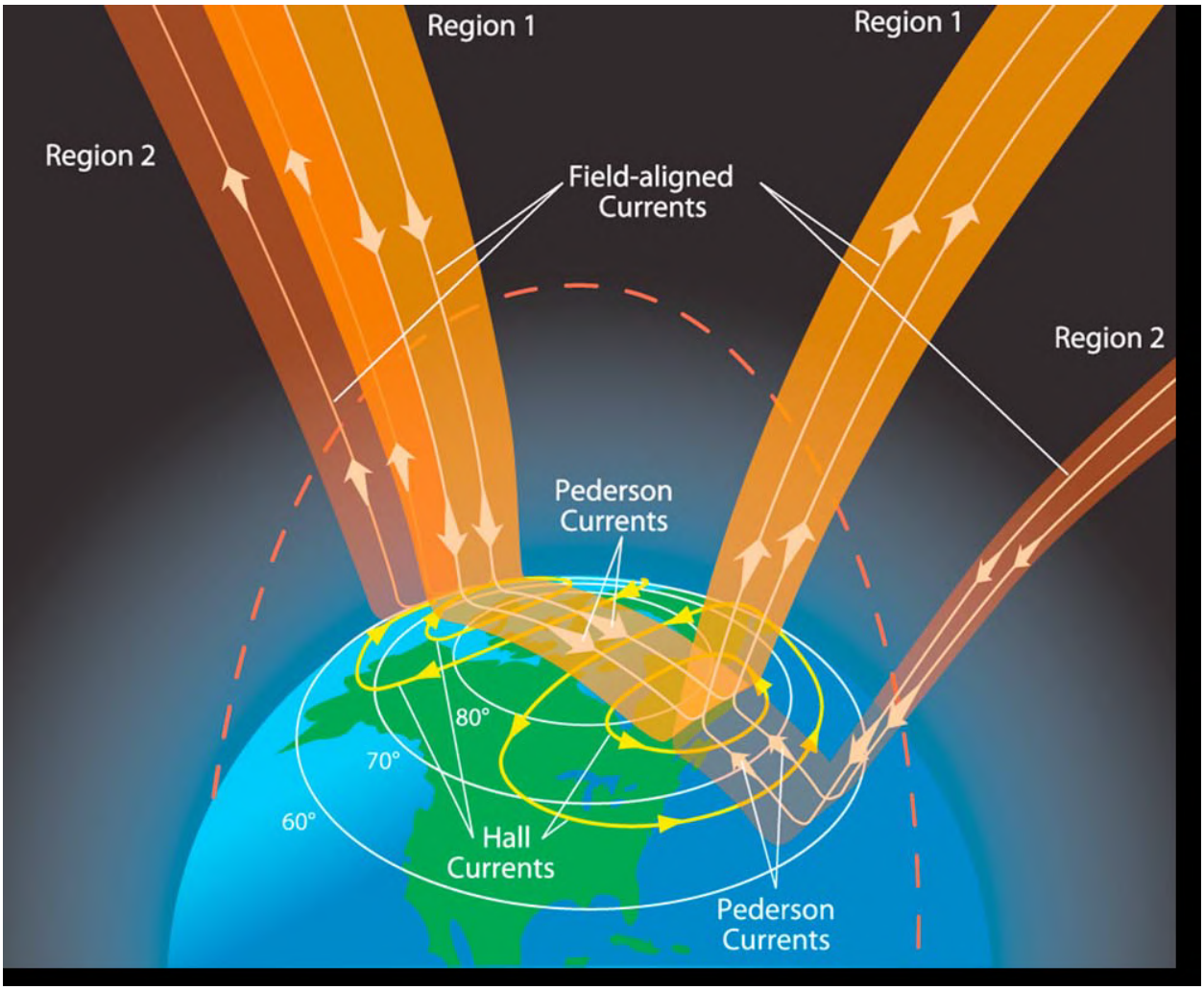

Figure 1.2: Diagram of ionospheric processes. Interactions of particles with the magnetic environment at high latitudes induces various plasma currents within the upper atmosphere. The Field Aligned Currents are coupled to the larger scale magnetosphere structure. Adapted from Le et al. (2010).

Coupling the Polar Cap to the magnetic field lines comprising of both the magnetotail and

the dayside boundaries induce a large scale electric potential across the entire polar region, producing a significant dawn-to-dusk electric field[95]. This extends down the entire circuit, resulting in a net magnetospheric electric field from dawn to dusk and inducing convection of the plasma sheet. With the particle fluxes and energies within the magnetosphere system, substantial currents are induced in the auroral-zone fields of the ionosphere, reaching $0.1\,MA$ typically and spiking to $1\,MA$ during times of geomagnetic storms and substorms[46].

Further structure is created within the ionosphere to compensate the drifts observed as ions flow through the magnetic field. Streaming particles are always subject to the Hall effect, and Hall currents indeed form in the upper ionosphere along these open field lines.Total azimuthal drift of the ions and electrons is the sum of the gradient drift and curvature drift effects. Gradient drift is encountered as a charged particle interacts with a magnetic field which has a gradient in magnitude. Curvature drift occurs when a particle attempts to follow a curved magnetic field line: following the curvature of the field line itself requires a drift velocity out of the plane of curvature to compensate the experienced centripetal force. As a result, the azimuthal drift is charge and mass dependent, leading to a charge separation effect in the ionosphere and giving rise to two distinct Field-Aligned Current (FAC) regions (Region 1 and Region 2). Connecting these regions are multiple current pathways called Pedersen currents arching through the auroral zone.

FACs couple to the magnetosphere-solar wind system, and information between them are exchanged in interactions. Current is flowing; there is an outflow of ions from the Earth's ionosphere counter-streaming against solar wind particles. Components of the outflow directly affect the magnetospheric system, where all of these plasma dynamics are very sensitive to the composition of the plasma[37, 28, 101, 50, 95]. Production of ionospheric source ions varies per particle. Photo-ionization in the upper atmosphere depends on the molecule binding energies as well as by depth of penetration of these photons.

1.2 Magnetospheric Phenomena Observations

Evidence for the topics in the previous section comprise of *in-situ* measurements of plasma composition, density, and fields taken by many dedicated spacecraft and missions over the years. A handful of key missions and instruments will be outlined in the following section for their contributions and instrument design.

1.2.1 Influential Missions and Instrumentation

Magnetospheric Multiscale Mission Magnetospheric Multiscale Mission (MMS) was launched on March 12, 2015 to investigate magnetic reconnection in detail throughout the magnetosphere. Cluster proved it was possible to coordinate four spacecraft into a spatial structure in orbit, and MMS took advantage of the predecessor's logistical rocket launch. Similarly to Cluster, MMS has a tetrahedral formation of four identical spacecraft. However, the orbit of MMS differs from Cluster, with MMS orbiting around the equator in a highly elliptic orbit so that it frequently passes through areas of active magnetic reconnection[57].

Onboard are two more ToF based mass spectrometer instruments, one called the Hot Plasma Composition Analyzer (HPCA) and the other the Energetic Ion Spectrometer (EIS). While the bulk of the other instruments aboard MMS were designed for fast samplings of ambient plasma, they can accommodate large fluxes of charged particles at the expense of the lack the capability to distinguish the different ion masses. Subsequently, the HPCA was included to further characterize the sampled plasmas.

Fast Auroral Snapshot Imager Geomagnetic behavior is influenced by the interaction with solar wind plasma and can generate intense plasmas in the upper ionosphere, and precipitating particles produce aurorae. The Fast Auroral SnapshoT Imager (FAST) was developed to investigate the particle dynamics in quick, high resolution bursts during these events. This inquiry takes FAST through a highly elliptical and polar orbit about the Earth and through the auroral regions, resulting in a perigee (apogee) of 350 km (4175 km) and

$\sim 83^\circ$ inclination. With an orbital period of approx. 133 minutes, this allowed FAST to cross over the auroral ovals four times per orbit[66]. Launched August 21, 1996, the FAST satellite mission investigates the auroral ionospheric phenomena with *in-situ* measurements.

Particularly, the mission was launched to further our understanding of the auroral mechanisms. Visible aurorae are observed between 100-200 km above the surface, while the acceleration of the particles that produce the aurorae themselves are contained in a region at much higher altitudes of 2000 - 10000 km, in the high latitudes of Earth[66]. Investigation of the microphysics involved requires high resolution measurements of both fields and particles, and subsequently FAST incorporates a high resolution mass spectrometer among its instrument suite.

With the goal of characterizing 3-D ionospheric ion distributions, it shares many heritage components with the other ToF instruments, like CODIF and Active Magnetospheric Particle Tracer Explorer (AMPTE)[42]. Onboard, the Time-of-Flight Energy Angle Mass Spectrograph (TEAMS) simultaneously determines the 3-D distribution function of plasma as well as the mass composition[42].

Equator-S Launched on December 2, 1997, Equator-S was a low-cost mission to fill in the gaps of observations in the magnetosphere surrounding the Earth's equatorial plane. At the time of launch, data in the Earth's equatorial plane was sparse, so a scientific payload very close to Cluster and WIND was put into an eccentric orbit, eventually covering all the regions of interest in the equatorial plane. This orbit flies the satellite through the day-side magnetopause, and the boundary layer. On the apogee of the orbit, the near-Earth magnetotail is sampled by Equator-S[42].

The satellite includes composition instruments onboard, including the ToF-based Ion Composition Instrument (ICI) which was set up identical to CODIF on the Cluster mission, while the accompanying ESAs are different between the missions. ICI measures the 3D distribution functions of the major ion species, H^+, He^+, He^{++}, and O^+. ICI utilizes a

retarding-potential analyzer (RPA) along with a toroidal ESA to expand the energy-per-charge range to 15 V - 40 kV without applied RPA voltage, and down to spacecraft potential with the RPA. Approximately 20 kV post-acceleration is used to facilitate the transmission of ions through the carbon foils of the ToF section.

Cluster Mission Cluster is a mission comprised of a group of four identical spacecraft designed to answer the ESA and NASA scientific inquiries on small-scale structure of the Earth's nearby plasma environment *in-situ*, and how all the different plasma populations interact. To this end, the four identical satellite suites were launched in July 2000, orbiting within the magnetosphere in a tetrahedral formation for a full 3D view of the ambient plasma. The orbits of the spacecraft pass through key regions of interest in magnetospheric physics, including areas of interaction with the solar wind[73, 72].

Cluster was outfitted with the Cluster Ion Spectrometry (CIS) scientific suite, which includes 11 different instruments to study the local plasma environment. The focus of this thesis has to deal with improvement to one of these onboard spectrometry instruments: the Ion Composition and Distribution Function analyzer (CODIF) which incorporates a top-hat style ESA. CODIF is a typical heritage ToF mass spectrometer, utilizing a thin carbon foil as the initial scattering surface. ToF mass spectrometry basics are covered in Section 2.1 while CODIF is discussed in greater detail in Section 2.1.4.

We will focus on CODIF for this experiment as an engineering copy was available for use with our proposed modifications. CODIF is discussed in greater detail in Section 2.1.4 and our modifications outlined in Section 4.

1.2.2 Observations and Contributions

Of the missions explicitly capable of observing nitrogen, the Suprathermal Mass Spectrometer (SMS) on AKEBONO compared cold ion outflow between oxygen and nitrogen. Yau A. W. and Whalen B. A. (1992) found a magnetic storm dependence of the minor ion species

from $\sim 5 - 20\,eV$, ranging from ${}^{N^+}/_{O^+} < 0.1$ during quiet geomagnetic time periods, and increasing to about ${}^{N^+}/_{O^+} \approx \{0.5 \sim 1.0\}$ in active periods. [98, 99]. For reference, the escape energy for a nitrogen ion at Earth is $\sim 9\,eV$. Additionally, Schunk et al. (1980) also observed with Atmosphere Explorer the second most prevalent ion in the upper F region of the ionosphere was N^+[77]. Convection electric fields, solar cycle activity, geomagnetic activity, etc. can also produce conditions favorable for the growth of a N^+ dominated plasma. Hamilton et al. (1988) with the Active Magnetospheric Particle Tracer Explorer (AMPTE) found a high energy enhancement of nitrogen in the ring current, at energies $> 30\,keV$. During a magnetic storm, they observed that these ions undergo an enhancement in energy similar to oxygen, and N^+ can be the second strongest enhancement of all the ions[31].

In fact, Ilie et al. compounded many independent studies into a case study on the dynamics of O^+ in the magnetosphere which support this MHD perspective. These studies all find that O^+ can dominate both these densities, and by extension control the large scale redistribution of energy and mass[36, 35, 37, 77, 101, 31, 27, 28, 17, 44, 63, 95].

Oxygen outflow is fairly well understood, and can be linked to oxygen production rates. Nitrogen outflow is not understood well, but correlates to how much nitrogen remains 'locked in' solid compounds on Earth like nitrates, etc. Ionospheric outflow of ion species are different; the mechanism for escape of N^+ is vastly different for that of O^+ and are both different of their respective neutral particles' mechanism of escape. For example, the photoionization and binding energies are vastly differing.

Shortcomings However, almost all the instruments making O^+ observations fail at resolving N^+ from O^+. As a result, the data collected that is often tagged as "oxygen" is actually the sum of both the nitrogen and oxygen populations[37].

1.3 Thesis Research Objectives: Science Motivation

Improving the resolution of mass spectrometry is an active area of detector development for *in-situ* spacecraft. NASA science objectives impose an inherent limit to both the mass of the detectors onboard, as well as the power the instrument can draw. As a result, novel detector methods are investigated and older heritage instruments continually improved upon to reduce both the mass and power requirements.

Carbon foil-based Time of Flight (ToF) entrance systems cause a significant amount of energy dispersion for the plasma ions the instrument is detecting. In addition, the particles require a significant acceleration boost to promote successfully traversing the carbon foil, referred to as the Post Acceleration voltage (PAC). Precision measurements are necessary for some recent ESA-NASA space mission objectives, some of which aim to be able to distinguish between N^+ and O^+ at fast timing resolution. Utilizing carbon foils incorporates unavoidable energy loss as these ions scatter in the carbon foil. Scattering must be significantly reduced to reasonably distinguish these ions at a 95% confidence level. Using acceleration voltages ensures particles continue forward after the carbon foil, but induce some variance in the spectra. Additionally, these require a large high voltage power supply, which occupies a large portion of spacecraft mass and onboard power requirements.

To alleviate the loss in resolution imposed by carbon foils and improve separation of ions species that are close in mass, like N^+ and O^+, we investigate methods to reduce scattering and energy loss at the entrance system. Primarily, we focus on Microchannel Plates' (MCPs) response to incoming ions, building onto the work by Fraser et al. (2002)[26]. We replace the entrance carbon foils of an existing engineering prototype of the time-of-flight Ion Composition and Distribution Function analyzer (CODIF) with straight-channel MCPs. Straight-channel MCPs are chosen to replace the carbon foils under the premise that the entering particles will collide with the walls of the MCP pores under grazing-incidence angles, generating an appreciable electric cascade while negligible energy is lost from the ion[20]. Since the ion is losing less energy than it would had it passed through a carbon foil, the need

for a Post Acceleration Voltage (PAC) would largely diminish, if not vanish, as demonstrated by Cadu et al. (2012)[11].

In particular, we investigate ion time-of-flight spectra response for different geometries of MCPs as well as thin film coatings on the MCP channel walls contrasted against the standard thin carbon foil. The works of Cadu et al. (2012) and Devoto et al. (2008) demonstrated MCPs facilitate grazing incidence detection, but as a proof of concept; the effects of MCP geometry and emissive coatings were not investigated[11, 20]. MCP geometries and thin film coating composition selection for this experiment were chosen by performing simulations with the software package Stopping Range of Ions in Matter (SRIM) and TRansport of Ions in Matter (TRIM) 2008, incorporating the respective effects. Ultimately, by the simulation results given in Section 5, four MCPs were selected: a set of standard uncoated MCPs and one set coated with the best performing thin film of aluminum oxide, where each set is comprised of two relatively low Length to Diameter ($^{L}/_{D}$) ratios of 20 and 40. This way, both surface composition and geometrical effects can be studied separately and in tandem.

A selection of ions were chosen to cover a broad range of masses as well as energies typical for a space-based spectrometer, and include:

$$H^+,\ H_2^+,\ He^+,\ N^+,\ H_2O^+,\ N_2^+,\ Ar^+$$

Each of these ions are evaluated to determine the following:

1. Direct comparison of mass spectrometry Time of Flight (ToF) spectra, energy/timing resolution, and efficiency between a carbon foil, uncoated $PbSiO_3$ MCPs, and Al_2O_3 coated MCPs.

2. Impacts of MCP characteristics and other parameters, such as Length per Diameter (L/D) ratio, Open Area Ratio (OAR), depth of coating, and ion angles of incidence.

3. Agreement with simulations of the above using SRIM/TRIM 2008 for carbon foils and the various coated MCPs.

2 Overview of Current Mass Spectrometry Technology

2.1 Time-of-Flight Mass Spectrometry

Time of Flight (ToF) mass spectrometry determines mass per charge by measuring the (non-relativistic) time delay between a 'Start' signal and a 'Stop' signal as ions of a known energy traverse a drift path of known length. A diagram of CODIF is depicted in Figure 2.1. From non-relativistic energy equations, the mass depends as $m = 2E/v^2 = 2E/\left(\frac{d}{\Delta t}\right)^2$ and therefore, additional hardware is required to measure or filter by energy per charge. Typical applications include a variant of an Electrostatic Analyzer (ESA) to sweep over a wide range of plasma energies. The ESA utilizes an applied electric field to steer incoming charged particles with electrostatic force. The combination of electric field and geometry pass charged particles within a specific energy range, while the applied force is always perpendicular to its velocity; as a consequence, the particle has no work imparted to it and the ESA conserves the initial kinetic energy of these ions.

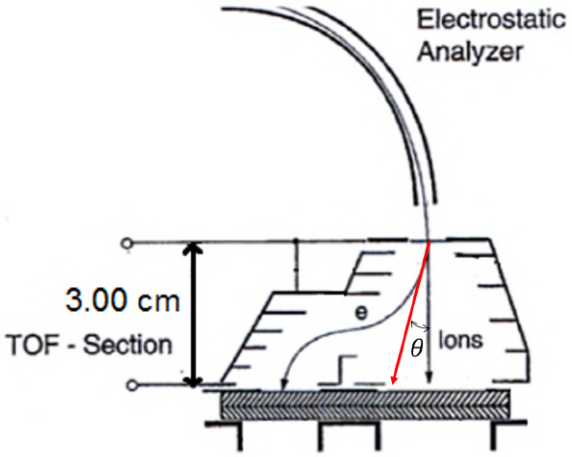

Figure 2.1: Illustrated above are scattered trajectories of impinging particles. In red is a heavily scattered particle from the entrance. The increased path length caused by this trajectory is increased to $3sec(\theta)$, and increases the ToF accordingly.

2.1.1 Electrostatic Analyzer Physics

Electrostatic analyzer benefits can be seen by solving the Poisson Equation. The basic functionality between the various geometrical designs remains the same: act as an energy filter before the particle can continue onwards. Most designs are accomplished by applying a known sweeping or constant voltage across two parallel plates over a known arc length or distance. Here, we can relate the median of the Gaussian-distributed energy E of the

transmitted plasma's energy to be proportional the applied voltage ΔV and a constant proportional to the electric field topology, called the Analyzer Constant C given by the equation $E = e\Delta V/C$. (Some literature uses the reciprocal, $K = \frac{1}{C}$.) This analyzer constant C is related to the geometric factor, denoted G_F. The geometric factor relates the detected electron cascade flux to the incident particle flux, thereby deriving the latter as well as its distribution function[24].

With all the derivations by Farnell et al. (2013), the optimal spherical ESA setting will deflect particles with incoming energy E_o along the trajectory $r_o = \frac{r_1+r_2}{2}$ without deviating. We assume that the electrodes are biased such that the particle trajectory along r_o experiences no potential, or $V(r_o) = 0$. Table 2.1 lists a few commonly used detectors and their constituent Analyzer Constants[24].

Detector	Analyzer Constant C	Median Energy E_C
Parallel Plate[a]	$C = \frac{8d\sin\phi\cos^3\phi}{L}$	$E_C = \frac{e\Delta V}{\left(\frac{8d\sin\phi\cos^3\phi}{L}\right)}$
Cylindrical[b]	$C = 2ln\left(r_2/r_1\right)$	$E_C = \frac{e\Delta V}{2ln(r_2/r_1)}$
Spherical[c]	$C = \left(\frac{r_2}{r_1} - \frac{r_1}{r_2}\right)$	$E_C = \frac{e\Delta V}{\left(\frac{r_2}{r_1} - \frac{r_1}{r_2}\right)}$

[a] With the length L between entrance and exit apertures, separation of parallel plates d, and particles arriving at azimuthal angle ϕ.
[b] With the outer radius of curvature r_2 and inner radius of curvature r_1.
[c] With the outer radius of curvature r_2 and inner radius of curvature r_1.

Table 2.1: Listed are some Analyzer Constants for common ESA configurations.

Given the relationship with the applied voltage and geometry, this allows for the ESA to selectively transmit particles of a known energy per charge E/q ratio. Ions without the corresponding energy per charge crash into the walls of the ESA and are prevented from entering the remainder of the detector. However, there is a spread in energy per charge of the particles transmitted, related to the energy passband of the ESA. Ultimately, this affects the resolution of the instrument by changing the geometric factor, which discussed in more detail in Section 2.1.3.

Arguably the most important aspect of the ESA is the energy passband ΔE, which is the

FWHM in energy of transmitted particles leaving the ESA. From this passband, a design can be constructed to fix the remaining parameters, such as necessary voltage per center plasma energy, the radii of curvature for spherical, cylindrical, or parallel plate distances, and aperture widths. We refer to the works of Farnell et al. (2013) for detailed discussion on formulation of the Analyzer Constant, the geometric factor (discussed later), and how this energy passband is related to the angular deviation of the plasma[24].

CODIF, the focus of this work, utilizes a top-hat style ESA. A top-hat style ESA is a modified spherical ESA, where particles enter at the midpoint of the hemispheres with a third "top-hat" electrode overlooking the entrance aperture, and traverse an arc of $\pi/2$ radians to the exit. Depending on the application of the ESA, this would typically lead to the ToF entrance. A typical design of this top-hat is illustrated in Figure 2.2.

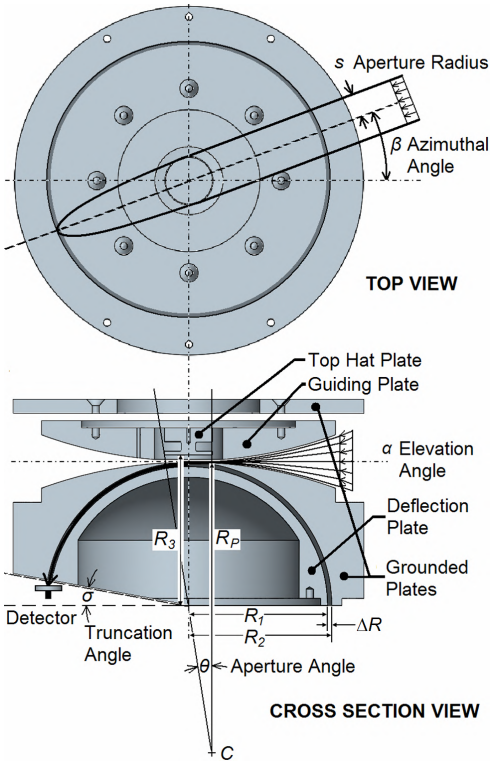

Figure 2.2: Cross-sectional view of a typical Top-Hat ESA. Adapted from Victor et al. (2006)[90].

2.1.2 Physics of Time-of-Flight Drift Chambers

The ToF chamber itself is fairly straightforward: ions that successfully traverse the entrance foil encounter a drift chamber of a known, fixed length. Since the length of the drift path is fixed, we can infer the velocity of an incident ion by the time difference between a signal generated at each end of the drift chamber. To facilitate ions passing through the entrance, the chamber body is held at a constant Post Acceleration voltage (PAC). Ions impacting the carbon foil generate secondary electrons caused by collisions within the foil, with the knockoff electrons averaging around 3-10 eV. Some additional pulling electrodes, applied

PAC, and geometry of the drift chamber are designed to minimally affect the trajectories of ions, while steering the low energy electrons towards the electron multipliers designated for the "Start" signals. Ions will continue over the full drift chamber length, eventually encountering an electron multiplier for the ions. Each ion that collides with the active detection area will generate an electron cascade, which will be detected as a "Stop" signal.

Provided that both the Start and the Stop signals deposit enough charge to trigger the external electronics constant-fraction discriminators (CFD), the time delay between the Start and the Stop will be collected, yielding a time difference Δt. With that and the non relativistic energy equation (and assuming no energetic losses in the carbon foil), we obtain the velocity, and we can derive the mass-per-charge in terms of the energy-per-charge[73, 72]:

$$\frac{m}{q} = 2\left[\frac{E_o/q + V_{PAC}}{\left(\frac{d}{\Delta t}\right)^2}\right] \tag{2.1}$$

When paired with the energy-per-charge information from the ESA settings, we can subsequently determine the mass-per-charge. Note that the ToF chamber determines only velocity; an ESA is required for more detailed information. Since the drift is velocity dependent, it has some useful properties for spectrometry purposes.

First, any charged molecule that fragments on impact with the entrance foil will cause the fragments to each retain the mother particle's velocity by conservation of momentum. This holds for particles that undergo charge exchange on impact as well[73]. The equipotential used is designed to significantly steer only the low energy electrons and leave ions negligibly affected, continuing straight towards the back end of the chamber. As neutrals will not be steered regardless, they will follow a similar trajectory as the ions and produce a ToF spectra very closely matched. Therefore, the ToF spectra produced for all of the fragments will be identical to that of the mother particle. Additionally, this property allows for the detector to be very unaffected by internal charge exchange.

Secondly, any included ESA will allow the same energy-per-charge ratio to pass through,

which includes multiple charge states, e.g. He^{++}. However, the drift chamber measures velocity. Therefore, the combination of the ESA with the drift chamber yield a mass per charge ratio. By varying the potential of the ESA, different energy per charge particles are transmitted to the drift chamber portion. Consequently, ions of different masses and charge states can be identified using this velocity dependent approach in ToF systems.

2.1.3 Geometric Factor

Previous sections describe the internal dynamics of the ESA, as well as the ToF physics for particles that successfully traverse the ESA and ToF drift chamber. However, not all particles from the ambient plasma environment incident on the detector are detected. In order to relate detected events with that of the local plasma environment, a method is required to work backwards and derive the total incident flux from the detected flux, and to that end is the concept of geometric factor. The geometric factor is a sampling of the observed particles within a velocity space carved out by an angular and energy dependence.

Traditionally, the geometric factor is calculated by:

$$G_F(E) = A^{\Delta E}/_E \Delta\Theta\Delta\Phi \tag{2.2}$$

where A denotes the aperture area, $^{\Delta E}/_E$ is the error in energy, and $\Delta\Theta$, $\Delta\Phi$ denote the angular acceptances in azimuth and polar directions, respectively.

Victor et al. (2006) expanded the velocity space term for the symmetry of a quadrispheric analyzer[90] (a variant on an electrostatic analyzer) truncated at an angle σ seen in Figure 2.2.

$$< \frac{dv}{v} d\alpha >= \frac{1}{4}\left(\frac{r_2 - r_1}{r_1}\right)^2 \csc^3\left(\frac{90^o - \sigma}{2}\right)\left[\frac{7}{8} + \cos\left(\frac{90^o - \sigma}{2}\right)\right] \tag{2.3}$$

This expansion can be transformed into a more useful quantity by converting to energy space, which is directly related to velocity space. First, is the proportionality of the energy

and velocity distributions, of the following

$$\frac{\Delta E}{E} \approx \frac{C_k}{K} \approx < 2 \cdot \frac{dv}{v} d\alpha > \tag{2.4}$$

If we utilize spherical symmetry, and truncate at $\sigma = 0^o$ (identical to CODIF) then we can simplify further, to

$$G_F(E) \approx \frac{18.74 \cdot r_o^2}{K^{7/2}} \left[cm^2 \cdot sr \cdot eV/eV \right] \tag{2.5}$$

provided $r_o$is in cm. This generalized form is, again, for full polar field of view, extrapolated to a full sphere $(4\pi\, sr)$[90].

Comparing with the ESA of CODIF, the analytical version is pretty accurate. Reme et al. (1997, 2001) measured the geometric factor of the ESA of CODIF utilizing Formula 2.2. Including transmission probabilities, each of CODIF high sensitivity region pixels measure $2.16 \cdot 10^{-3}\, cm^2 \cdot sr \cdot {}^{eV}/_{eV}$ while the low sensitivity region pixels measure $2.3 \cdot 10^{-5}\, cm^2 \cdot sr \cdot {}^{eV}/_{eV}$ by Reme et al.[72, 73]. With the above formalisms, we can include the transmission probabilities of the ESA (95% for high side, 1% for low side[73, 72]) in Equation 2.5 and scale by the solid angle of each pixel. Doing so yields $2.26 \cdot 10^{-3}\, cm^2 \cdot sr \cdot {}^{eV}/_{eV}$ for the high side and $2.37 \cdot 10^{-5}\, cm^2 \cdot sr \cdot {}^{eV}/_{eV}$ for the low side, marking a margin of error of 4.6% and 3.0%, respectively.

This end result again relates the current of those particles, and therefore the number, that exit the ESA with that of the ambient plasma incident upon the ESA entrance. For large K, this is a small fraction of the ambient plasma. Exiting ions then interact with the ToF portion of the detector, which has its own geometric factor to compensate for.

The ToF chamber is subject to similar constraints in its geometric factor, but it behaves differently. First, particles incident on any electron multiplier medium (traditionally thin carbon foils) have an associated stopping power. Stopping power applies complicated braking forces on the incident ion, dependent on the incident particle's energy, trajectory, mass, and

on the density of the target. It is no surprise that a significant fraction of these incoming ions do not pass through the foil, and are "lost". In addition, stopping power causes the particles to scatter, and lose energy "straggling" in the foil.

We can subsequently convolute these two geometric factors (ESA and ToF) together and achieve a net geometric constant for the whole system, G_{FT}, to relate total flux input to total flux detected.

2.1.4 CODIF Instrument

Section 2.1.4 encompasses the ToF theory of operation particular to the CODIF instrument. Section 2.1.4 briefly details the contributions made by CODIF, while Section 2.1.5 discusses the disadvantages inherent due to the configuration and design of CODIF.

The Cluster Ion Spectrometry (CIS) experiment is the scientific suite launched on July and August 2000 to study the magnetosphere surrounding the Earth, including sites of magnetic reconnection. Four identical spacecraft were launched in a tetrahedral spatial orientation, a controlled variable distance apart from one another. Distance between the craft has varied between $\sim 100 - 10000\,km$ over the course of the mission. The spacecraft flew in highly elliptical, polar orbits. These orbits obtain a minimum perigee near $\sim 4R_E$ (Earth radii), a maximum apogee of approx. $\sim 20R_E$ and approx. 57 hour period. CIS experiment's orbit is such that over about one year, it has precessed over all local times.

Figure 2.3: Photo of the CODIF sensor on the lab bench. Particles enter the ESA through the cylindrical openings on the left, and travel down to the inner drift chamber.

CIS experimental suite included a Hot Ion Analyzer (HIA) and a time-of-flight Ion Composition and Distribution Function analyzer (CODIF). CODIF consists of a top-hat style

Electrostatic Analyzer (ESA) entrance system along with a drift chamber. Together, it determines the distributions of the constituent major ion species[73], and is pictured in Figure 2.3. The ESA selects incoming particles by their energy per charge via electrostatic deflection, and then CODIF's drift chamber determines mass per charge by the time it takes the ions to drift $3.00\,cm$ to a set of Microchannel Plates (MCPs) to act as a charge amplifier. The HIA effectively extends the dynamic range of the suite to include large ion fluxes, but does not measure ion mass.

Introduction to Sampling Plasma Distributions The premise behind mass spectrometry is ultimately to determine the mass of some particle, electrically charged or neutral. There are various means to accomplish this goal, and each has its advantages and disadvantages. Many more instrument types exist, but the three most relevant are quadrupole ion traps, magnetic sector, and time-of-flight instruments.

Any instrument that has to sample large ensembles of particle fluxes are subject to the effects of statistical variations caused by the collection of events. From the classical perspective, an ensemble of measurements of individual ions of a known, constant rate invoke a statistical Poisson distribution and subsequent error in these measurements. For a Poisson distribution, n events are observed with the total expected number $N = Rt$ depending on the constant rate of the source R and the collection time t. The probability P_n of observing n events with expected N events is thusly:

$$P_n(N) = \frac{N^n}{n!} e^{-N} \tag{2.6}$$

The statistical error in count rates σ from Poisson statistics behaves as $\sigma = \sqrt{N}$ with the total number of expected events N. Note this is statistical error from measuring n total, separate ions - it refers to the observed error from repeated measurements of a constant ion source. Therefore, as the sample size increases, the relative error $\sigma/N = 1/\sqrt{N}$of the measured mean decreases. The above is for counting statistical treatment of plasma ions. These

ions are normally distributed in energy, and that follows similar treatment of a Gaussian distribution.

For the Gaussian distributed energy of the plasma, we can relate its FWHM to the observed standard deviation of the events σ_N.

$$FWHM = 2\sigma_N\sqrt{2ln\,(2)} \tag{2.7}$$

However, since we measure a finite sample of ions, that implies the mean of the continuous Gaussian distribution can vary with the sample size. This is referred to in the literature as the standard deviation of the mean $\sigma_{\bar{x}}$ and is related to the standard deviation of the distribution σ_N and total events N by:

$$\sigma_{\bar{x}} = \frac{\sigma_N}{\sqrt{N-1}} \tag{2.8}$$

Subsequently, the larger the sample size becomes causes a reduction in the error of the mean of the distribution from statistical observations.

ToF Spectrometry by CODIF Mass spectrometry, and ToF based spectrometry in particular, involve a multitude of physical mechanisms just to register one ion. This section aims to break down all the interactions an ion can undergo within the CODIF sensor. This section will start with the basics - what mechanisms incoming charged particles experience in the order the particles receive them. Afterwards follows a more detailed inspection of key points involving CODIF. Then, current magnetospheric contributions from the CODIF sensor are expanded upon, and current shortcomings with the instrument.

First Interaction - the Electrostatic Analyzer Under normal operation, an incoming charged particle first interacts with CODIF's top-hat Electrostatic Analyzer (ESA), which filters these particles by their energy per charge. Top-hat style ESAs such as this one utilize a spherical deflector (the top-hat), which rests above the midpoint of two hemispherical electrodes. The advantage of this is a full 360^o view, and the three electrodes steer ions

in a toroidal symmetry, which can be well described without loss of generality as spherical symmetry.

The ESA for CODIF has an intrinsic energy resolution of $^{\Delta E}/_{E} \approx 0.16$ and as a result a passband of ions are allowed to continue through to the ToF drift chamber, with the remainder crashing into the walls of the ESA and ending their journey[73].

Second Interaction - the Drift Chamber Entrance After sifting by the ESA, this ion is accelerated by a Post Acceleration Voltage (PAC) towards a thin $\sim 3.0\ \mu g/cm^2$ carbon foil array, typical for heritage missions. For the low energy ions to continue through the drift chamber, the PAC is significant. Incoming particles scatter off the carbon foil, emitting $\sim 10\, eV$ secondary electrons from the carbon foil and are steered away to an isolated MCP resting along the inner radius of CODIF for further multiplication into a macroscopic signal on the order of $10-100\, mV$ out of the anode. Particles that fragment after colliding with the entrance foil carry the mother particle's velocity each, so all fragments will have the same ToF[73]. Traditional ToF spectrometry involves generating a signal at both the entrance and exit of a drift chamber for a particle. However, scattering with the carbon foil has two major drawbacks:

1. The particle has to successfully navigate through the carbon foil and reach the exit side of the drift chamber to produce another signal; consequently the carbon foil must be kept very thin.

2. Scattering reduces the energy of the particle, and low energy particles need a large PAC to accelerate it to the point where it has a high probability to exit the foil into the drift chamber.

Third Interaction - Exit Drift Chamber Provided the ion has significant energy to pierce the carbon foil and continue, it encounters a 3.00-cm drift path down to a deck of MCPs pictured in Figure 2.1. Ions continue straight due to their much higher mass than the

electrons, and cause an electron cascade at these Stop MCPs. This MCP deck is a Chevron stack of two individual MCPs, which drastically increase the probability of detection, and amplify the single event. The time difference between these signals infers the mass per charge of the incident ion. However, carbon foils invoke a large energy loss as the particle must 'punch through' and continue to the MCPs for a usable signal to be generated. The time difference between these signals is recorded using a prototype constant-fraction-discriminator utilizing a time-to-amplitude converter. Typical spectra observed from a carbon foil at 22 keV total energy for various ion species can be seen in Figure 2.4. The accompanying spectra quantities of interest are included in Table 2.2. Flux ratios are included where these ratios convey the fraction of detected flux per observed Start for the Start efficiency, and per observed Stop for the Stop efficiency. Ions observing both a Start and a Stop is called a Valid: Start efficiency is defined as $\eta_{Start} = {}^{Valids}/_{Stops}$, and similarly the Stop efficiency is defined as $\eta_{Stop} = {}^{Valids}/_{Starts}$.

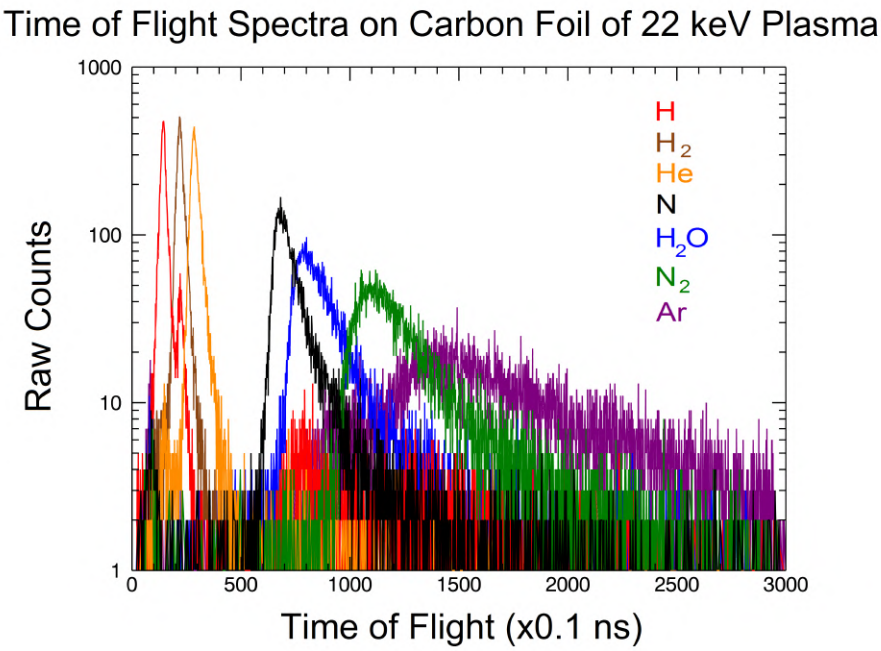

Figure 2.4: Overlay of various ion time-of-flight spectra through a carbon foil. These plasma spectra were observed on a 10 keV initial energy with 12 kV PAC, for a total energy of 22 keV.

Ion	Total Events	Stop Efficiency	Start Efficiency	Peak ToF [ns]	FWHM [ns]
H^+	16267	0.4094	0.1457	14.5	2.3
H_2^+	16328	0.5330	0.1622	21.8	2.4
He^+	16370	0.7059	0.2093	28.6	3.0
N^+	16177	0.4156	0.1822	68.2	6.9
H_2O^+	16112	0.4283	0.1954	80.1	18.2
N_2^+	16025	0.3760	0.1998	105.2	30.8
Ar^+	15495	0.2615	0.1555	149.2	79.2

Table 2.2: Table of various plasma spectra data, observed on a 10 keV initial energy with 12 kV PAC, for a total energy of 22 keV to accompany Figure 2.4.

The length of the drift chamber is known to high precision, and the velocity distribution of incoming particles can be inferred from this as well as the distribution in time it takes the particles to traverse the gap. At launch, CODIF demonstrated the capability to accurately determine timing differences down to 0.2 ns when supplied with 100 mV signals. Changes in

signal intensity affect the timing comparators in the circuitry, so smaller (or faster) signals will change this statistic.

CODIF Contributions Heavy singly charged ions are predominantly of ionospheric origins, and have inherently different production means. While nitrogen and oxygen ions only differ by a 12% mass difference, the ionization energies are very different, 15.581 eV for nitrogen and 12.069 eV for oxygen. This property directly affects the scale heights at which photoionization occurs, and subsequent ions flowing out of the ionosphere[37]. However, the majority of studies have neglected the significance of nitrogen to the dynamics of the ionosphere and magnetosphere owing to the inability and difficulty involved to distinguish between these ions very close in mass.

2.1.5 Challenges of ToF Spectrometry by Carbon Foil

Scattering Losses Prior sections treated ToF mass spectra generally, inclusive of any suitable medium that allows the ion to be transmitted through while knocking off a few electrons to initiate a cascade. Traditional ToF spectrometry involves generating a signal at both the entrance and exit of a drift chamber of known length for a particle, using a carbon foil at the start to generate a handful of secondary electrons which are further amplified later into an electron cascade. An illustration of the ToF drift chamber of CODIF is shown in Figure 2.1. This section specifically explores the drawbacks of carbon foils in ToF detector applications.

Resulting velocity distributions of transmitted particles can be inferred from the distribution in time it takes these particles to traverse the drift gap. Incoming particles scatter off the carbon foil, however this scattering has two major drawbacks:

1. The particle has to successfully navigate through the carbon foil and reach the exit side of the drift chamber to produce another signal; consequently the carbon foil must be kept very thin.

2. Scattering reduces the energy of the particle, and low energy particles need a large PAC to accelerate it to the point where it has a high probability to exit the foil into the drift chamber.

The loss of energy in a carbon foil is energy and mass dependent, with energy loss becoming significant at high masses and low energies. Stopping Power of carbon is well researched and is nonlinear with respect to the thickness of the foil, as well as energy of the impinging particle[6, 105, 104]. Scattering also causes the angular distribution out of the carbon foil to broaden. As the angles are now diverging from orthogonal to the drift chamber, the transit time increases due to the change in trajectory. These straggling particles produce a profound "tail" to the ToF spectra, reducing resolution, and reducing instrument sensitivity to heavier particles. Substantial drawbacks discussed are all scattering dependent; these can be mitigated by reducing the overall scattering observed, like via grazing incidence of the ions onto surfaces.

CODIF Shortcomings While ToF spectrometry instruments are fairly robust, there are certain aspects particularly prone to error. There are a few different ways the measurements can be disrupted, to varying degrees of efficacy.

- Generate falsely coincident signals
- Attribute detected ion to incorrect mass per charge
- Electronic deadtime

First, falsely coincident signals occur from a few different sources, but the end result is the same; the electronics pick out a seemingly random Start and Stop signal pair that are not correlated. One situation includes illumination of the electron amplifiers (in CODIF's case, the MCPs) with a high energy penetrating radiation such as relativistic electrons. These electrons are very likely to penetrate the instrument's casing and directly interact with the MCPs, producing unrelated cascades of electrons. Overwhelming the signals with

uncorrelated spectra swamps the system, and cripples the production of spectra for as long as the particles bypass the entrance of the ESA. In addition, high background rates can cause a Start signal to be matched to a random, uncorrelated Stop, producing another false ToF. These situations can occur if the MCP gain is large.

Second, ions detected could be misinterpreted by the logic, and categorized as a different mass per charge. Typically, this manifests for the higher energies and lighter mass ions due to the comparable ToF each have. For example, He^{++} has the exact same time of flight as diatomic H_2^+, and at the highest energies the Gaussian peaks pertaining to H^+, H_2^+, He^+, *and* He^{++} start to overlap. Therefore, a chance exists that some ions of one peak are logged by the electronics as one of the others. This effect varies with energy and mass, affecting the lighter and more energetic ions more significantly.

Finally, electronic deadtime is a major constituent, dependent on impinging flux rate. At launch, the onboard CODIF electronics utilized a timing-to-amplitude converter (TAC) to produce a voltage proportional to the time delay between a Start and a Stop signal. This was sampled by a fast analog-to-digital converter (ADC) which could fully digitize the signal in a conversion time under $6\,\mu s$, which means any signal more frequent than approx. $166\,kHz$ would be masked as the electronics struggle to keep pace with the signals.

The following sections look at each issue in more depth. Accompanying each are some observed performance problems other studies have experienced. Afterwards, the limitations are discussed, as well as possible remedies to the issues.

False Coincidences A previous study by Mouikis et al. found that while CODIF was in orbit, significantly high fluxes of relativistic electrons cause falsely coincident ToF data [61]. This significant intensity of energetic penetrating radiation belt electrons bypass the ESA, and pass through the instrument. During the transit, these electrons can interact with the MCPs used for the Start and/or Stop signal, producing a signal. When this is picked up by the electronics, there is a high probability of a randomly selected Start and Stop being

falsely labeled coincident and subsequently logged as a physical ion.

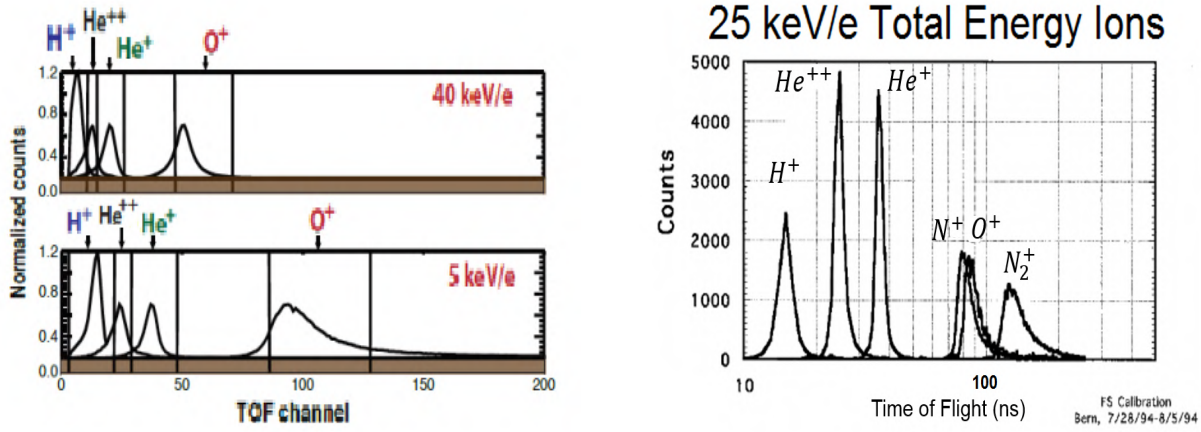

(a) CODIF spectra of "spillover" effect during its mission. Included is a 40 keV/e and 5 keV/e beam. Adapted from Mouikis et al. 2014.

(b) CODIF spectra of "spillover" effect during its mission. Included is a 25 keV/e beam collected from calibration data at the University of Bern. Notice the significant overlap of nitrogen and oxygen. Adapted from H. Reme et al. 1997.

Figure 2.5: CODIF spectra of "spillover" effect during its mission. Included is a 40 keV/e and 5 keV/e beam during flight, and a 25 keV/e calibration beam. Adapted from Mouikis et al. 2014 and H. Reme et al. 1997.

Spillover Effects In addition, for certain energies and masses of ion there is a region of "spillover", where the skewed Gaussian peaks of the spectra are so close together in time channels that they overlap. In other words, certain ranges in energy and mass exist where the lower energy portion of protons, for example, overlap with a portion of the He^{++} peak, which Figure 2.5 illustrates. Furthermore, the 25 keV/e calibration data in this figure also points to a significant overlap of nitrogen with oxygen. As a result, all studies with CODIF that include oxygen data can potentially be contaminated with nitrogen ions.

Additionally, Liao et al. performed a statistical study on oxygen outflow from the ionosphere using CODIF data. To further complicate matters, a velocity filter effect described by Horwitz (1986)[34] was found to characteristically inhibit low energy $\sim 10 - 40\,eV\,O^+$ from reaching the instrument [50]. As a result, the lack of low energy oxygen generates an underestimation of outflow from the lower ionosphere. Methods to increase the detection

efficiency of low energy heavy ions would strive to alleviate, at least partially, the lack of detected ions in this range.

Lack of resolution in the CODIF instrument also limits magnetic reconnection studies as well. A study on magnetic reconnection rates by S. Wang et al. (2015) elucidated the importance of ion moments on reconnection. However, the study was constrained to O^+ ions above 5 keV for calculating the moments of these ions, due to significant contamination of protons in low energy oxygen within the magnetotail [93][92].

Electronic Deadtime Finally, the available computing time of the electronics complimenting CODIF constitute the final shortcoming of the unit. While the electronics are in the middle of a computation, the electronics prohibit any new signals from initiating a new calculation. Consequently, any new events while one is being processed will be ignored (masked). At launch, the CODIF instrument's limitation was in its analog to digital converter (ADC); this had an upper limit on conversion time of $< 6\mu s$ which corresponds to a maximum average rate (without prominent masking effects) of $\sim 167\,kHz$[73]. As a result, if the average flux rate of any signal (Start or Stop) exceeds this rate, then a significant chunk of events are simply missed as the electronics struggle to keep up with the calculations.

2.2 Advances in Time of Flight Detectors

2.2.1 Mass Resolution Motivations for Improvements

Three main properties are always of significant importance within ToF spectrometry: energy lost in the scattering processes, energy dispersion within the scattering medium, and angular dispersion caused by the scattering. Heritage of these styles of mass spectrometers include the Ion Composition and Distribution Function analyzer (CODIF), and the Charge, Element, and Isotope Analysis System/Mass Time-of-Flight (CELIAS/MToF) on Solar and Heliospheric Observatory (SOHO) among others.

This thesis investigates the following inquiries related to the science behind the mechanisms of ion detection:

1. How do the effects of grazing incidence affect the residual energy, dispersion, and detection efficiency of the commonly sought ion distributions compared to that of a heritage carbon foil?

2. What role does surface geometry/topology have under grazing incidence collisions and detection?

3. Can the addition of surface layers significantly alter the observed residual energy, dispersion, and detection efficiency? If so, what mechanisms contribute?

MCPs with straight channels have been chosen based on their geometry to facilitate grazing incidence scattering within CODIF. In a grazing incidence model, impinging particles will only specularly reflect once, which minimizes the energy lost and the corresponding dispersion of energy, in addition to constraining the angular distribution due to the internal MCP geometry.

2.2.2 Time of Flight Resolution

Efficacy of ToF mass spectrometry hinges on making the mass resolution as precise as possible. From Equation 2.13, the mass is derived from the measured transit time of the ion. As a result, the mass resolution $\Delta m/m$can be shown to expand to the form:

$$\Delta m/m = \Delta\left(\frac{m}{q}\right)/\left(\frac{m}{q}\right) = \sqrt{\left(\left(\frac{\Delta E}{q}\right)/\left(\frac{E}{q}\right)\right)^2 + \left(\frac{2\Delta t}{t}\right)^2 + \left(\frac{2\Delta d}{d}\right)^2} \tag{2.9}$$

where ΔE is the error in energy of the impinging ions due to the ESA as well as energy dispersion from scattering within the colliding medium, Δt is the error in observed ToF predominantly from signal electronics, and Δd the error in path length of the ToF drift from manufacture[20, 73].

Primary influence of the grazing incidence method is to vastly improve the quantity ΔE caused by scattering. Inside a carbon foil, massive and low velocity ions receive a significant loss of energy, which dominates the mass resolution in Equation 2.9.

2.2.3 Grazing Incidence Demonstration

Microchannel Plates (MCPs) are relatively well known for their high interaction surface areas, and subsequent electron gain from a single ionizing input event. Any impinging particle or photon can liberate an electron within the plate, depending on the energy transfer. Previously, we discussed how the energy transfer follows an angular dependence. In a grazing incidence setup, the object is to have incoming particles "graze" the walls of the MCP channels at shallow angles. A small portion of the incident ion's kinetic energy will be deposited into the local lattice atoms of the plate, with most of that going into the valance electrons. MCPs are discussed in greater detail in Section 3.

Angular effects on the production of secondary electrons has been studied in the past. Bouchard et al. (1979) simulated a simplistic model of secondary electron yield as a function of incident energy of a primary impinging electron and incident angle, with the results compared against existing grazing incidence data seen in Figure 2.6. As for the numerical simulation, we defer to the detailed calculations within the work[7, 88]. What can clearly be seen is the trend of larger angles of incidence (more parallel to the surface) to liberate more electrons and increase the secondary electron yield. The author attributes this increase to a material absorption property; as the angle of incidence becomes

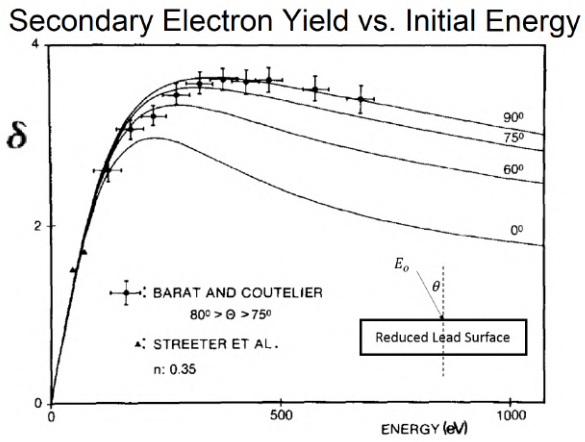

Figure 2.6: Experimental secondary electron yield δ as a function of primary incident particle energy, for impinging electrons on a reduced lead glass. Adapted from Bouchard et al. (1979).

more parallel to the surface, any secondary electrons are produced very close to the surface and are very likely to be ejected from the material due to the lack of material along the path to reabsorb them[7]. As the angle goes towards surface normal, there is now a higher probability of being scattered inward, into the material and getting absorbed that way, reducing the secondary electron yield.

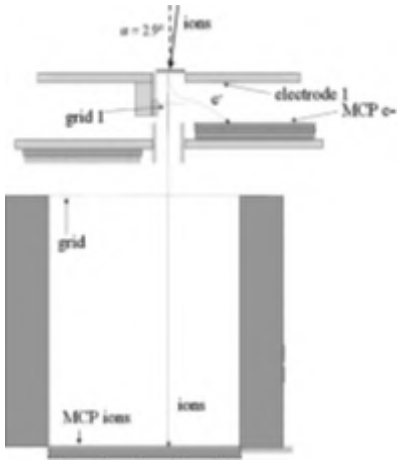

Figure 2.7: Setup and used in the studies from Cadu et al. (2012) and Devoto et al. (2008)[11, 20]. Adapted from Cadu et al. (2012) and Devoto et al. (2008).

This observed angular dependent enhancement in secondary electron production inspired the use of MCPs as an electron emitter for solar wind energy particles. MCP characteristics have been studied in applications for mass spectrometry. Cadu et. al. (2012) simulated and prototyped a ToF mass spectrometer based off a similar design of CODIF, using MCPs instead of carbon foils along a 5.00 cm ToF section. Figure 2.7 illustrates the setup used, with the resulting spectra depicted in Figure 2.8. As can be seen in the diagram, the incident ions follow a trajectory biased to the same angle as the bias of the MCP, so the vast majority of the plasma distribution runs parallel to the pores of the MCP. This leaves the fringes of the plasma's (Gaussian) angular distribution with trajectories capable of interacting with the MCP channel walls at very shallow angles, called "grazing incidence". They demonstrated high mass resolution without a Post Acceleration Voltage (PAC) based off the concept of "grazing incidence" of the incoming ions. For very shallow angles of incidence with this setup, N_2^+ can be distinguished from O_2^+[11, 20]. This proof of concept sparked further inquiry into the use of MCPs as the entrance electron amplification medium for solar wind energy particles. We improve upon this work by investigating how geometry and coatings of the MCP factor into the spectra.

Consequently, the combined effects of energy transfer, depth of secondary electron emission, and angular dependence of the secondary electron yield are the most important aspects for mass spectrometry under grazing incidence. In addition, the combination of secondary electron yield and energy transfer govern the energy lost by the impinging particle. Ultimately, the shallower angles will increase resolution this way.

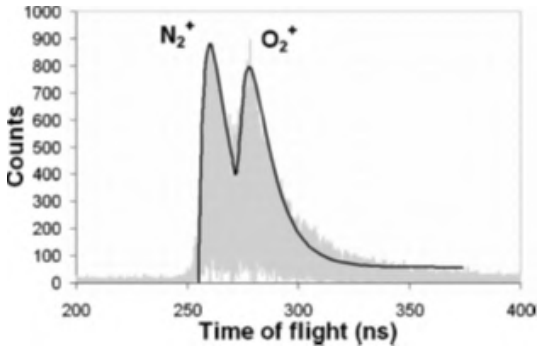

Figure 2.8: Spectra produced for molecular oxygen and nitrogen, showing a clear separation of ions only 4 amu apart by mass, without the use of a Post Acceleration Voltage[11, 20]. Adapted from Cadu et al. (2012) and Devoto et al. (2008).

2.2.4 Geometrical Dependence

Grazing incidence models are one method of evaluating the performance of MCPs, but there are other options available to consider. One such mechanism that will affect scattering is the dependence of the MCP gain on the L/D ratio. MCP gain is the total output charge pulse originating from a single incident particle. In other words, this is the (mean) number of output electrons per individual incident particle, and can be expressed as a (dimensionless) ratio of the total number of output electrons per singular incident particle.

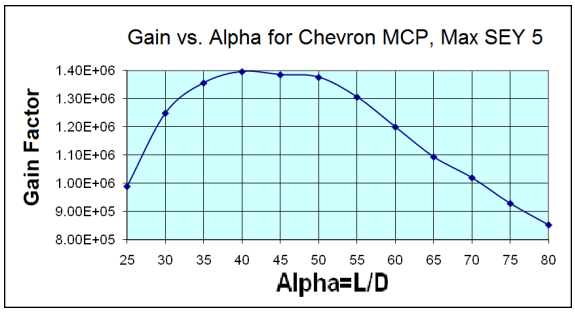

Figure 2.9: Using computations done by Guest (1979), the gain as a function of L/D ratio was computed by Ivanov et al. (2009). Adapted from Ivanov (2009).

Sternglass et al. (1957) investigated this SEY, which was found to be expressed as $\gamma(\theta) = \gamma_0 sec(\theta)$, and is a function of incident angle[83]. This can also be seen in the works of Lennard et al. (1986) in their angular dependence of argon's electronic stopping power[48]. Furthermore, MCPs exhibit a gain dependence on the L/D ratio[88, 39].

Ivanov et al. (2009) investigated the gain response as a function of aspect ratio, results depicted in Figure 2.9. They used a secondary emission model developed by A. J. Guest (1971) and found a trend of gain on the aspect ratio[88]. As the ratio increases, the number of emitted secondary electrons decrease. The authors concluded the MCP parameters drastically depend on the secondary emitter. While the gain is affected by the aspect ratio, the emissive properties were more significant, and increasing the average yield δ from 4 to 5 shifts the distribution up a factor of 10 while maintaining the distribution profile[88].

This model is summarized by Equation 2.10 below.

$$\sigma\left(V,\theta\right) \quad = \quad \left[\frac{V}{V_{max}}\sqrt{cos\left(\theta\right)\sqrt{\frac{V_o}{V}}}\right]^{\beta} e^{\left[\alpha\left(1-cos(\theta)\sqrt{\frac{V_o}{V}}\right)+\beta\left(1-\frac{V}{V_{max}}\sqrt{cos(\theta)\sqrt{\frac{V_o}{V}}}\right)\right]} \quad (2.10)$$

Here, β, V_{max} are material properties determined by numerical fits, V is the incident energy, $\alpha = {}^{L}/_{D}$ and θ is the incident angle for the total gain σ, developed by Guest[29, 88].

Subsequently, increasing the aspect ratio is expected to influence the mechanisms involved in grazing incidence scattering. Provided the incident angle is kept constant, the larger aspect ratios should reduce the signal amplitude of the output signal, and reduce the flux of detected particles accordingly. However, increasing the MCP aspect ratio also imposes a maximum angle of incidence; beyond this maximum angle, the incident particles will undergo multiple channel collisions and degrade the resolution accordingly.

2.2.5 Emissive Properties of Coatings

Number of electrons liberated per event depends directly on the energy deposited into the electron cloud of the colliding atoms inside the plate. This in turn is influenced by the electronic properties of the material. Most notable properties affecting scattering and electron emission include the density of the material, the work function, band gap, and first ionization energies. Some properties of commonly used compounds are outlined in Table 2.3. The dynamic range of MCP operation is directly proportional to the current running through

the channel walls[86]. Coating materials can alter these properties, allowing for increased or reduced gain as desired by varying resistivity and secondary electron yield (SEY), which ultimately affects the frequency of feedback events and electric potential required to begin ion feedback effects.

Compound	Density $[g/cm^3]$	Work Function ϕ [eV]	Band Gap E_G [eV]	First Ionization Potential E_I [eV]
$PbSiO_3$[a]	$3.1-4.0$	6.3	3.76	7.9
Al_2O_3[b]	3.987	$5.1-7.1$	7	8.9
MgO	3.58	$2.8-4.4$	7.8	8.76
W	19.3	4.5	-	7.98

[a] including amorphous
[b] amorphous

Table 2.3: Electrochemical properties of commonly used compounds for electronic gain.

Addition of emissive layers on substrates to improve material properties has been studied in detail. The majority of metal oxides behave as dielectric, electrically insulating materials, and have been investigated for their high secondary electron yield (SEY) values[91]. The major drawback to dielectric materials are the effects of surface charging. If these films are too thick, or the replenishment electron current is too small, or primary particle energy is too high, then the surface will begin to accumulate charge. In turn, this severely inhibits secondary electrons escaping to vacuum, and diminish the SEY[91]. Additionally, the gain observes a dependence on the total charge extracted per area from the MCP, with gain suffering from degradation as more charge is extracted.

Part of the improvement arises from the volumetric effect: the volume of the surface layer determines the SEY more significantly than the surface state of the solid[91, 8]. Using electrons as the primary particle inducing secondary emissions, Wang et al. (2018) found that the introduction of a composite film of $MgO-Al_2O_3$ significantly increases the total SEY, the maximum SEY, and the energy of the primary electron required to achieve the maximum SEY when compared to just a layer of MgO. They posit this change is likely caused by uniformly distributed metallic aluminum impurities inside the layer, allowing for

good charge transfer to the surface and inhibiting surface charging effects[91].

While the majority of effects of the coating are related to secondary electron emission, coatings can still confer a measure of improvements other than that caused by increase in SEY and gain. First, the much higher SEY will cause more events to be detected by the electronics due to the significantly increased electron cascade per ion. Additionally, the material properties of the coating are dependent on the primary ion energy, which in turn determines the volume of interaction available as well as the energy required to liberate an electron. For aluminum and magnesium oxide films, the electronic stopping power is much smaller (and the corresponding SEY is much larger) compared to the bare lead silicate MCP. As a result, the energy transfer from the ion primary is reduced.

2.2.6 Energy Loss

Foils in general invoke a large energy loss as the particle will scatter within the foil. The formalism in Section 2.1.2 is again only for particles without energy loss. Considering losses in the medium depends upon the total stopping power of the medium. Ions with lower energy will take longer to traverse the drift path, proportional to the inverse square root of the energy, seen in the equation below, derived from the energy equation[73, 42].

$$t = d\sqrt{\frac{m/q}{2\left(E_o/q + V_{PAC}\right)}} \tag{2.11}$$

Energetic losses within a carbon foil can be included as a scalar constant of proportionality $\alpha\left(E_o, m\right) > 1$ per incident ion mass, and incident ion energy. Using this, we obtain a "smeared" spectra of

$$\frac{m}{q} = 2\alpha\left[\frac{E_o/q + V_{PAC}}{\left(\frac{d}{t}\right)^2}\right] \tag{2.12}$$

For measured time-of-flight t, and

$$t = d\sqrt{\frac{m/q}{2\alpha\left(E_o/q + V_{PAC}\right)}} \tag{2.13}$$

For measured mass-per-charge m/q and a correction factor α.

Particles traveling through any medium are subject to a large variety of different forces simultaneously, making the process complex. The macroscopic effect that manifests over many interactions is bremmstrahlung radiation, as kinetic energy is transferred from the incident charged particle to the orbital electrons in the medium bulk. In general, the most important scattering processes include electronic stopping power, which are the inelastic screened Coulomb collisions between the ion and target's orbital electrons; nuclear stopping power, encompassing both elastic and inelastic Coulomb collisions of nuclei. Electronic stopping power describes the energy lost from the ion, and transferred to the numerous valence electrons of the bulk of the medium. Depending on the energy available to each electron, they can either be liberated from their atomic orbit, or they can spontaneously jump to a higher quantum state (and subsequently re-emit radiation as it jumps back down later)[26, 2, 96]. Meanwhile, nuclear stopping power describes the momentum transfer between collisions of the atomic nuclei, and subsequent slow down of the incident ion. Alongside energy broadening, the multiple scatterings also cause angular dispersion.

2.2.7 Energy Resolution

MCPs can be coated in numerous resistive compounds, with magnesium oxide (MgO) and aluminum oxide (Al_2O_3) as the primary focus of this part of the study. The purpose behind these compounds is to dope the MCP silicate material, altering its inherent work function, increasing or decreasing it to suit different needs. To begin a cascade, an incident ion needs to satisfy $E_{e^-} = E_{ion} - \phi > 0\ eV$ where $E_{e^-}$is the knockoff electron's kinetic energy, E_{ion} is the incident ion's energy deposited into the MCP, and ϕ is the work function of the doped material[26, 2, 96]. Since the work function affects the energy required to emit secondary electrons during a collision, the coatings should then effect the detector's sensitivity of detecting ions. A decreased net ϕ allows for less energy deposition needed to begin a cascade. Due to the decreased energy deposition needed, incident ions can then produce a cascade at

smaller angles of incidence.

MgO and Al_2O_3 as compounds both have a low work function, and would strive to lower the effective work function as a coating dopant. This lowers the energy threshold for secondary electron generation, which should increase the yield, and gain as a consequence[3, 81, 12, 84]. However, since it is operating at grazing incidence, the energy deposited is concentrated within the doped layer and not the lead silicate MCP base. The difference in lattice structure of the energy deposition layer affects the scattering trajectories of the ions, which impacts particle straggling and energy resolution.

What this infers is that the vast majority of the incident particle's kinetic energy is retained and a significantly reduced amount is transferred to the MCPs in the collision due to the grazing incidence condition. Coatings will further reduce the energy needed to begin a cascade, thus allowing the ion to retain more of its initial energy. We expect that all types of MCPs will outperform the carbon foils in terms of energy dispersion, and added coatings to have even less dispersion.

2.2.8 Angular Dispersion

Carbon foils introduce multiple scattering processes to the impinging particles. In addition to the energy dispersion caused by scattering, the final trajectory after exiting the foil can severely deviate from the impinging trajectory. Scattering through foils have been well researched, and it follows a Gaussian distribution in exiting angle. This elongates the transit time in (planar) ToF drift chambers, causing a longer tail in the spectra and increasing the FWHM of the spectra, thereby reducing resolution. A depiction is in Figure 2.1, showing the effects of this. The particle takes longer to travel the exit side of the drift chamber, but these detectors are designed with a uniform distance between the entrance and exit. Subsequently, any angular deviations appear as a broadening of the spectra and accompanying loss in resolution.

2.3 Plasma-Surface Collisions

In this chapter, the basics of plasma detection, and subsequent material surface-plasma physical interactions are discussed. First, Section 2.3.1 investigates the scattering basics such as charge exchange, scattering cross sections, and Stopping Power. Following that is Section 3, devoted to the properties of microchannel plates (MCPs). Finally, previous research on grazing incidence and use of MCPs in mass spectrometry are covered in Section 2.2. Many simulation packages take into account the physical mechanisms described in this section.

2.3.1 Physics of Plasma Detection

For all types of mass spectrometry instruments, detection of a particle hinges upon generating an appreciable cascade of electrons that can then be detected by external electronics. In general this is accomplished by scattering the charged particle off some medium, liberating one or two electrons in the process, diffusion of the electrons to the surface of the material, and finally be ejected into vacuum. Typically, this is not enough for signal detection; additional electron amplification of the signal is required. Approximately a few milliVolts in amplitude lasting a duration of at least a few nanoseconds measured at full base width is enough for current electronics.

Charge Exchange Each time a particle (electrically charged or neutral) interacts with a bulk medium, charge exchange will occur. A neutral may gain or lose electrons in the collision, becoming ionized and altering its electrodynamic kinematics in a potential ionization process. Similarly, an ion may become neutralized in a process known as potential emission. We refer to the work of Allegrini et al. (2014) on the specifics of charge exchange of scattered particles.

Scattering Basics - Two Body Scattering

Center of Mass Frame The Center of Mass (CoM) frame pictured in Figure 2.10 is a convenient frame for treatment of elastic and inelastic collisions. Provided there are no transverse forces acting on a two-body system, this frame allows for the relative motion to be simplified to an equivalent system utilizing a single particle moving in a potential, centered at the origin. Given an ion with mass M_1 moving initially with a speed V_0 towards a target atom of mass M_2 at rest and collides, the result is the ion moving at speed V_1 after the collision, and similarly the atom recoiling at speed V_2. The frame itself moves at a common lateral velocity V_C relative to an outside observer to impose that the net momentum within the system is zero. In other words:

$$M_1 V_0 = (M_1 + M_2)\, V_C \tag{2.14}$$

In this frame, the equivalent conservation of energy, momentum, and angular momentum equations become:

$$\frac{M_2}{M_1} = \frac{V_0 - V_C}{V_C} \tag{2.15}$$

given an impact parameter b, reduced mass $\mu \equiv {}^{M_1 M_2}/_{(M_1+M_2)}$ as well as the definitions $J_C \equiv \mu V_0 b$ and $E_C \equiv {}^1/_2 \mu V_0^2$ for the particle[104].

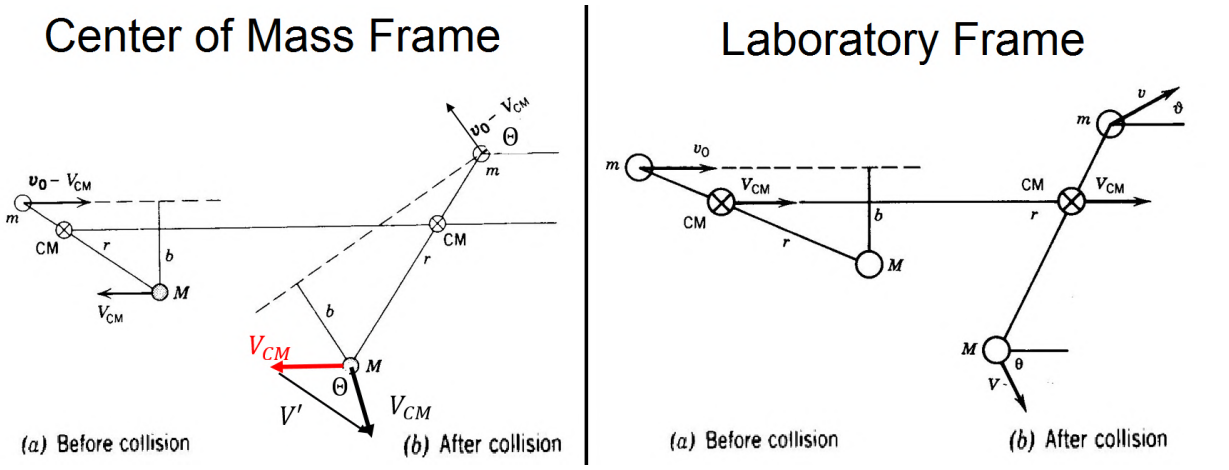

Figure 2.10: Conversion between Center of Mass and lab frames, utilizing vector math with the constant relative velocity of the CoM frame (not to scale). Adapted from University of Virginia, Raúl A. Baragiola (2003).

With this information, the initial and final parameters can be simply related to the final scattering angles. Due to the CoM frame moving at (lateral) velocity V_C, the total momentum of that frame is zero and is related to the lab frame. Figure 2.10 depicts this relationship. Due to this relative lateral motion of the CoM frame, the CoM recoil angle Φ is related to the lab frame recoil angle ϕ by $\Phi = 2\phi$ and similarly we can relate this to the projectile's CoM frame angle Θ via the relationship $\Phi = \pi - \Theta$. With this, the reduced mass μ, and applying vector math to the CoM frame, Ziegler et al. (2008) derives[104]: $V_2 = 2V_o{}^{\mu}/_{M_2} cos\,(\phi)$

This equation is for the lab frame's recoil atom velocity, dependent on the initial velocity and lab frame angle. However this is related to the CoM scattered angle, and can be simplified as such. Plugging into the kinetic energy equation to calculate the energy received during the collision yields:

$$T = \frac{M_2}{2}\left(\frac{2V_o\,\mu\,cos\,(\phi)}{M_2}\right)^2 = 4E_o\mu\,sin^2\,(\phi) \tag{2.16}$$

Therefore, the final CoM frame's angle of either the projectile or recoil atom (since both are identical in this frame) determines the total energy available to be transferred from the projectile to the recoil atom. As a direct consequence, the more shallow the angle, the less energy is transferred[104]. Depending on the specific transfer of energy and momentum, the

particle can scatter either elastically, inelastically, or quasi-elastically.

Stopping Power

Electronic Stopping Power Historically, the stopping range for ions begins with the consideration of the Coulomb interaction between the projectile ion, and the target's atomic structure. For the majority of ions, the presence of inner electrons provide a measure of screening and decrease the electric field available in the collision between the ion and the target. The electrodynamics involved in this interaction work against the projectile ion, reducing its velocity and imparting this energy to various electrons, causing excitations within the target material. This independent process is termed the electronic stopping power of the ion onto the target material. Electronic stopping power is inherently an inelastic process.

From the works of [6, 26], a semi-empirical model for the electronic stopping power S_e was found to be the following:

$$S_e = \left[\frac{dE}{dx}\right]_e = \left[\frac{8\pi^2 a_o}{u_o}\right]\left[\frac{N_o}{4\pi\epsilon_o}\left(\frac{Z_i Z_t}{\left(Z_i^{2/3}+Z_t^{2/3}\right)^{3/2}}\right)\right]\xi\cdot v\left(x\right) = C\cdot v\left(x\right) \tag{2.17}$$

This is valid for the energy transfer between an ion of mass M_i, atomic number Z_i, at speed v, onto a target with mass M_t, atomic number Z_t, and number density N_o. Here, a_o is the Bohr radius and u_o is the Bohr velocity ($u_o = 2.18 \times 10^8\, {}^{cm}/_{s}$).

Nuclear Stopping Power The above only deals with purely electromagnetic treatment of the ion-target interaction, which is valid for distances larger than the screening distance of the inner electrons. When the ion is much closer, both elastic and inelastic nuclear collisions need to be included. This treatment is best left to multiple-body central force scattering within the center-of-mass frame of reference. Recall the center-of-mass frame

pictured in Figure 2.10 as well as the standard laboratory frame.

Lindhart et al. (1961)[52] derived the nuclear stopping power for general applications. Using the Bohr assumption, which is at low velocities, the nuclear component of the stopping power is nearly constant. Due to this, it can be treated similar to the Thomas-Fermi expression. The maximum energy transfer between an ion of mass M_i, atomic number Z_i, onto a target with mass M_t, atomic number Z_t, at speed v is $T_{max} = {}^{2M_i^2 M_t v^2}/_{(M_i+M_t)^2}$, which can be integrated over the scattering cross section $d\sigma_n = \left({}^{S_n}/_{2\sqrt{T_{max}}}\right)\left({}^{dT}/_{T^{3/2}}\right)$ to yield a scaled function for the nuclear stopping power S_n:

$$S_n = \left(\frac{\pi^2 e^2}{2.17890}\right)\left[\frac{M_i}{M_i + M_t}\right]\left[\left(\frac{N_o a_o}{4\pi\epsilon_o}\right)\frac{Z_i Z_t}{\left(Z_i^{2/3} + Z_t^{2/3}\right)^{1/2}}\right] \cdot s\left(E^{'}\right) \tag{2.18}$$

Here, ξ_n is a dimensionless coefficient dependent on the Coulomb potential experienced by the nucleus. For Bohr-type nuclei, the experienced potential behaves as r^{-2} and the coefficient then approaches $\xi_n \to {}^{2}/_{(2.71839 \cdot 0.8853)}$ in the case where the nucleus is screened by the electron cloud.

This formula relies on a screened Bohr radius, given by $a \approx 0.8853 a_o \left(Z_i^{2/3} + Z_t^{2/3}\right)^{-1/2}$ with a_o being the classical Bohr radius[76, 53, 52, 33]. Notice, however, this equation is modified to incorporate inelastic nuclear collisions as well as elastic. A dimensionless scaling factor $s\left(E^{'}\right)$ is introduced to modify the purely elastic scenario to incorporate inelastic collision components, which are dependent on the reduced energy $E^{'}$. This factor is an empirical, piece-wise function of the reduced energy, where:

$$E^{'} = \frac{a \cdot M_i}{Z_i Z_t e^2 \left(M_i + M_t\right)} E = C_E E \tag{2.19}$$

Here, the nuclear stopping power is dependent on the (reduced) energy, and independent of velocity, as opposed to electronic stopping power discussed in the previous section which is velocity dependent.

All of these previously described physical mechanisms comprise and govern collisions

between plasma and surfaces. Detection of particles relies on the ability to efficiently emit electrons from the surface upon collision, and each of these secondaries becoming further amplified into an electron avalanche. As can be seen in this section, that requires a good collision cross section, and reduced thresholds for electron emission to occur. To this end, microchannel plates (MCPs) are commonly used for these purposes as they are able to obtain a great collision cross section, ease of liberating secondary electrons, and finally they have the added benefit of a huge interaction surface area.

3 Science of Microchannel Plates

3.1 Microchannel Plate Introduction

Microchannel plates, or MCPs, are thin plates typically made out of a semiconducting glass with numerous pores etched through the thickness of the plate, seen in Figure 3.1. Individual channels each have a diameter on the order of $\sim 10 - 100\,\mu m$ and are arranged in a closely packed structure[97]. This structure of the MCP results in a very large surface area from the numerous constituent channel surfaces.

Across the top and bottom sides of the MCP is a conductive electrode coating, typically a nichrome $NiCr$ which does not penetrate too far into the channels. The lead glass material composing MCPs is semiconducting, so electron multiplication is governed by the strip current replenishing the channel. Each individual channel in this manner is on the order of $10^9\,\Omega$ which act like a high density bundle of resistors in parallel, reducing the total observed resistance as a function of channel density. Typically, the total resistance approaches the order of $10^6 - 10^8\,\Omega$ per plate and this governs the strip current[97, 49].

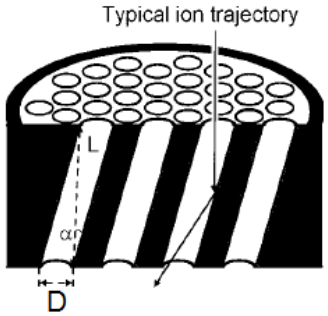

Figure 3.1: Cross sectional view of a bias tilt angle MCP, with channel diameter W and length of channel L, adapted from [11].

Secondary electrons can be produced upon particle collision if the energy transfer from the projectile is enough to liberate the target electron from its occupied orbital. MCPs are comprised of semiconductor materials, and thus the energy requirement to emit electrons is related to the band gap. The number of electrons emitted per collision is known as the secondary electron yield (SEY). Secondary electrons are then accelerated down the pore and collide again, liberating more electrons and forming a cascade. In effect, this behaves like an array of compact dynode amplifiers[97, 49], and the net sum of the SEY over the whole microchannel constitutes the gain. Both of these properties see MCPs commonly used as

electron multipliers.

MCPs can be characterized a few different ways, and all are equally important. First and foremost is the aspect, or $^{L}/_{D}$, ratio. This is the ratio of the length of the pores L to the diameter of the pores D, which can be seen in Figure 3.1. Aspect ratio governs some key geometrical properties, such as angle α in the diagram. Next, the pore density as well as diameter govern the Open Area Ratio (OAR), which expresses the open area (caused by pores) of the MCP face as a fraction to the total MCP face area. Finally, all the channels are etched at a certain bias angle. Another useful MCP characteristic is its intrinsic gain, where the MCPs have a maximum amplification they can support. This is limited by the strip current, and during normal operation this is approximately $10^3 - 10^4$ gain per MCP.

When used as electron multipliers, typical arrangements involve two plates in what is known as a Chevron stack. This arrangement is when the bias angles of each plate run against each other, and can achieve $\sim 10^6 - 10^7$ gain. Utilizing this method drastically improves the detection by increasing the chances of a collision while simultaneously limiting ion feedback effects (briefly discussed later).

3.1.1 Microchannel Plate Basics

MCPs are limited in their maximum amplification (or gain) mechanisms by two forms of saturation: space charge and current saturation. First is a space charge saturation, where the space charge density of the output electron cloud becomes large enough to electrostatically inhibit further output electrons from escaping. This space charge density is dependent on both the applied voltage on the MCP as well as the available space in the pores, which depends on the pore diameter[29, 97]. Larger diameters allow for more accumulation of space charge, and as such experience higher gains. Similarly, MCP current saturation is an imposed limit in the gain of the MCP based on the rate of replenishment of electrons in the channel walls. Replacing emitted secondary electrons is required to maintain the amplification process. Replenishing electrons are provided from the induced current running

along the channel walls caused by the applied voltage, and is subsequently dependent on the electrical resistance of the MCP. Larger resistances reduce the current flow available to the MCP to replace the emitted electrons, producing an upper limit to the total amplification possible.

Output electrons from a MCP have been profiled in energy by many groups, and notably by Koshida et al. (1985) in both saturation and unsaturated modes[43]. When a MCP was stimulated with a beam of electrons, the output electrons were found to follow an exponential distribution in energy, peaking around a few eV. The energy distribution has a long tail upwards of $> 100\,eV$ which was found to be highly dependent on the distribution of the MCP potential [43]. Distribution of the potential, and by extension the electric field uniformity, was found to be caused by the depth that the electrode faces of the MCP penetrate into the pores. This effect can be mitigated by controlling the depth of penetration; more penetration narrows the energy distribution, but gain suffers as a consequence.

Additionally, emitted electrons are dependent on the saturation of the MCP, with more saturation inducing more energetic tail electrons. Unsaturated modes of operation were met with smaller spread in energy of the output electrons (FWHM of the energy spectrum) than when in saturation [43].

The voltage drop across the semiconducting plate induces an internal electric field between the faces of the plate, which is parallel to the pores in a straight-channel MCP, and which has both tangential and normal components for an MCP with a tilted channel axis. This field accelerates the electrons generated towards the exit face of the MCP, and the ions towards the entrance face, but this effect is negligible for incident ions. Particles which have lost almost all of their kinetic energy or been implanted and subsequently re-ionized are significantly accelerated towards the MCP entrance face, and can obtain enough energy to initiate another secondary cascade in an effect called ion feedback detailed below.

3.2 Characteristics of Microchannel Plates

3.2.1 Kinetic Ionization

Kinetic ionization refers to the direct transfer of kinetic energy from an incident ion to the valence electrons in the MCP material, studied extensively by H. Winter (2007) across many different types of surfaces [96]. This study first investigated the effect of the bandgap of insulators to that of metals. Also studied were the effects of energy - using ions very close to the threshold energy and below this energy to cause kinetic emission, the secondary electron outputs were observed.

Kinetic ionization mechanisms are extensive and beyond the scope of this work; here we briefly outline the most significant mechanisms of electron promotion, surface morphology dependence and angular response, diffraction of electrons by plasmons, as well as surface excitons.

The investigation by Winter et al. (2007) probed protons for their remaining post-collision energy, as well as number of secondary electrons emitted per event. Observed trends show peaked structures in energy spectra, with a defined energy shift dependent on the number of electrons emitted; more electrons emitted cause the residual energy to decrease a small but significant amount for the proton which removed the electron(s)[96].

In addition to these experiments, Fraser et al. (2001) developed a semi-empirical formula describing the electron yield of ions which undergo kinetic emission. They derived a closed form expression for the total electron yield γ_k for any planar sample. Net result was a clear dependence on the velocity of the ion, and at sufficiently low velocities the dependence of the yield was linear with velocity [26].

Basic Velocity Dependence Kinetic emission first and foremost depends on the energy transferred ($dE\,(x)$) from the ion into the electron cloud (electronic stopping power), as well as from nuclear interactions (nuclear stopping power). As a direct consequence, the electronic stopping power S_e and nuclear stopping power S_n play a critical role.

Following the derivation of Fraser et al. (2002)[26], the number of free electrons created at depths x to x + dx depend on the electronic stopping power S_e. Now this is the total number of free electrons created at this depth; each has a classical semi-empirical probability $P(x)$ of escaping to vacuum. Therefore, the total secondary electron yield caused by only kinetic emission, γ_k, is the integral $\gamma_k = \int_0^T N(x) P(x) dx$ where T is the total thickness of the area of interaction. In the case of a microchannel, this is the maximum depth at which the ion-electron interactions occur. Fraser et al. (2002) calculated the resulting integral, and found:

$$\gamma_k = \frac{B \cdot P(0) \, csc(\alpha)}{\epsilon} \int_0^T S_e(x) \, e^{\left(\frac{-x}{L_s}\right)} dx \tag{3.1}$$

with $P(0)$ defining the probability of a surface electron escaping to vacuum, L_s denoting the escape path length of the secondary electron, and ϵ representing the average energy required to liberate an electron upon collision at a grazing angle of α, with B a semi-empirical constant $0 < B < 1$. Recall that from Beuhler et al. (1977) and Fraser et al. (2002)[6, 26], a semi-empirical model for the electronic stopping power S_e was given in Equation 2.17.

Unfortunately, this makes the integral in Equation 3.1 only solvable numerically or by approximation techniques. An exact solution exists, but requires piece-wise evaluation of the stopping power at velocity $v(x)$ over incremental distances dl, then calculate the new velocity after experiencing the retarding force, and repeat. However, as can be seen, this equation implies a linear relationship of stopping power in velocity.

Recent studies on kinetic emission reveal an interesting property: it is observed that electrons within insulating bulk materials (binding energies of valance electrons approx. 10 eV) are more efficiently liberated into vacuum than are conduction band electrons in a metal (work function approx. 4-5 eV)[96]. Kinetic emission relies on the transfer of energy from the impinging particle to the surface electron cloud of the target structure; a direct consequence of this means that more efficient energy transfers, like that of large angle scattering, more

easily liberate electrons from the target surface. Defects, pits, and impurities in the surface as well as other factors that make the surface "rough" alter the angle of incidence for the particles, which manifest as enhancements in electron emission[96]. The work of Winter et al. and the precursory studies by Roncin et al. demonstrate some energy from collisions manifest as wave phenomena, including surface excitons, plasmons, and diffraction of electrons[96, 75]. These mechanisms are beyond the scope of this work, but do contribute to a small extent overall towards modifying the angular and energy distribution of these secondary electrons.

3.2.2 Potential Ionization

Particles are not required to collide with the MCP to initiate emission of secondary electrons. The presence of a charged particle with a first ionization potential large enough causes it to rob an electron from the MCP material[26]. The excess potential energy released by this process can initiate an electron cascade.

Potential emission is en energy independent process of the ion. Subsequently, low velocity collisions will minimize the kinetic emission portion, and potential emissive properties will dominate. In addition, this process is heavily dependent on the charge state[26].

Potential emission was studied extensively by Aumayr et al. (2007), focusing on the effects of slow ions and inelastic processes [2]. Electrons can be ejected from the surface material's valence band if the available energy of ionization for the vacant state, W_i, exceeds twice the work function ϕ in a process called Auger Neutralization. They examined in detail a multitude of different Auger and resonant mechanisms where potential emission would occur. We refer the reader to their work for more in-depth treatments involving these resonant, Auger, and radiative processes.

3.2.3 Ion Feedback

Ion feedback is an undesired behavior of MCPs where positive ions are produced within the MCP initiate an electron cascade. Residual gas and adsorbed atoms on the MCP near

the output end of the channel can become re-ionized by the electron cascade during normal operation[86, 49]. Once ionized, it will experience the Lorentz force and accelerate due to the voltage applied to the MCP faces, heading back towards the input end. End result of these processes is a continuous, repetitive series of electron avalanches, saturating the channel and distorting the electric field as the channels begin to charge[86]. These methods both have enough energy to start an electron cascade, propagating down what essentially behaves as a multiplier tube and creating a false signal, seen as an increase in low-amplitude pulses in the distribution[86].

Minimizing the path length a positive ion can travel works just as well to inhibit ion feedback. More recently, MCPs are being fabricated that incorporate a curved microchannel to prevent the feedback ion from gaining enough energy to initiate an electron avalanche[49, 86]. The broad topic of ion feedback stretches beyond the scope of this work, and we refer to the works of Timothy et al. (1977), Leskovar et al. (1977), Wiza et al. (1979) for a more detailed investigation.

3.2.4 Dynodization

Secondary electrons generated in the MCP observe a uniform electric field induced by the applied voltage, and are accelerated accordingly. Eventually, they impact another section of the MCP pore, having traveled a distance z down the pore, and corresponding initial energies V_{or} in the orthogonal (into the MCP wall) direction and V_{oz} in the direction parallel to the channel axis. This distance is determined by the initial conditions of the emitted electron, which include the energy available to this electron perpendicular to the channel wall surface and the angle

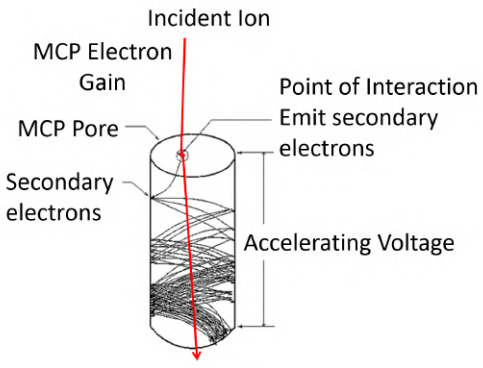

Figure 3.2: 3D sketch of trajectories of emitted electrons and ions internal to the MCP channel, and the dynode-like structures formed during transit.

it was emitted at. Eberhardt et al. (1979) studied this motion, and found deviations in z to be self correcting; Δz changes the energy available at the next collision and that available energy compensates by an equal but opposite displacement $-\Delta z$ when averaged over the whole ensemble of electrons [22]. Subsequently, a classical dynode structure is formed, and one is depicted in Figure 3.2.

4 Experiment Implementation

This work is an in-depth investigation into methods of improving upon the standard ToF instrument via novel methods of collision detection. By using microchannel plates in a setup where ions specularly reflect or "graze" off the internal plate channels, we demonstrate a significantly improved mass resolution than traditional ToF instruments, at the cost of instrument efficiency.

This chapter is divided into three major sections: thesis research objectives are contained in Section 4.1, followed by the advantages and drawbacks conferred by MCPs in Section 4.3, and finally the experimental setup is detailed in Section 4.2.

4.1 Thesis Research Objectives: Detail and Implementation

Utilizing the engineering model of the CODIF instrument, we will illuminate it with a broad range of ion species over various energies to determine the following:

1. Direct comparison of mass spectrometry Time of Flight (ToF) spectra, energy/timing resolution, and efficiency between a carbon foil, $PbSiO_3$ MCPs, and coated MCPs.

2. Impacts of MCP characteristics and other parameters, such as Length per Diameter ($^L/_D$) ratio, Open Area Ratio (OAR), depth and composition of coating, and ion angles of incidence.

3. Simulations of the above using SRIM/TRIM 2008 for carbon foils and various coated MCPs.

4.1.1 Objective 1

In line with ionospheric and magnetospheric missions like MMS, Objective 1 covers a series of commonly sought ions:

$$H^+,\ H_2^+,\ He^+,\ N^+,\ H_2O^+,\ N_2^+,\ Ar^+$$

(with Ar for reference). Each ion's data, sampled from a constant flux, monoenergetic beam, will be compared against changes in PAC, applied MCP voltage, applied ESA voltage, and total energy on both the canonical carbon foil pixel and MCP pixel. The majority of these ions are common plasma constituents of interest for the Earth's (and other planet's) magnetospheres, ionospheres, as well as the heliosphere, hence why these ions are chosen as targets.

4.1.2 Objective 2

Objective 2 touches on some of the other geometrical properties of MCPs, in an attempt to characterize MCP behavior. Utilizing similar methods to Objective 1, MCPs with different properties in addition to coatings will be tested. These intrinsic properties govern the response of the MCP to incoming stimuli, the results of which contribute to macroscopic effects and influence characteristic behavior. Some key factors to focus on are the energy required to emit an electron from the MCP material during a collision, the MCP gain defined as the total number of electrons liberated per incident particle, and how the MCP geometry itself plays a role.

4.1.3 Objective 3

In addition, typical plasma parameters for CODIF under nominal operation will be simulated for the lighter atomic ions. Utilizing SRIM/TRIM 2008, the complex, stochastic plasma-surface physical interaction will be simulated, taking into account a wide range of surface effects. SRIM outputs can then be applied to our detector geometry to generate a ToF spectrum we would expect to observe at those parameters. The experimental results of the foils and MCPs will then be compared against each other and against the simulation of the ion.

SRIM/TRIM was chosen for this application due to the program's robust approximation methods and semi-Empirical data package. The software employs a wide range of physical

effects of collisions that are significant at our detection range, including energy dissipation to phonons and nuclear recoils. SRIM excels in the low energy $\lesssim 1\ MeV/amu$ and fits existing stopping power measurements well. Given the range CODIF operates is $1\ eV - 40\ keV$ and the focus on surface interactions, SRIM/TRIM was chosen.

4.2 Experimental Design and Methods

However, there are a large number of possible geometries and coatings available for MCPs to be used for the carbon foil replacement. As of the publication of this thesis, the most readily available MCPs include geometries ranging from $^{L}/_{D}$ 20, 40, 60, and 80. Additionally, the most readily available MCP thin coatings are magnesium oxide and aluminum oxide, via Atomic Layer Deposition (ALD) methods. Due to this vapor deposition method, larger diameter (smaller $^{L}/_{D}$ ratios) are preferred for uniform layer formation. As will be discussed in Section 5, the simulated response to ions depicts aluminum oxide as superior to magnesium oxide in regards to spectra width (resolution), and reduction in energy transferred on collision. Additionally, aluminum oxide is much less reactive than magnesium oxide, which readily reacts with water for example. Consequently, the MCPs chosen include an uncoated $^{L}/_{D}$ 20, an uncoated $^{L}/_{D}$ 40, a 60 Å aluminum oxide coated $^{L}/_{D}$ 20, and a 60 Å aluminum oxide coated $^{L}/_{D}$ 40.

4.2.1 CODIF Reconfiguration and Methodology

To accommodate the MCP in the existing, heritage structure of CODIF, some electrical and mechanical alterations had to be made. Visible in Figure 4.2 are the physical changes made to house a circular MCP. A spare circular carbon foil array was fabricated, as one pixel needed to be cut back to allow for the circular holder. The two neighboring pixels needed to be cut as well to affix the holder to the array. Electrical changes were required as well. The carbon foil faces closest to the ESA are all held at the PAC potential, so we wanted to keep that consistent as well. Each MCP tested had its top face (closest to the

MCP	R_{MCP} $[M\Omega]$	R_{BAL} $[M\Omega]$	V_{MCP} $[V]$		
			$10\,kV\ PAC$	$12\,kV\ PAC$	$14\,kV\ PAC$
Uncoated $^{L}/_{D}$ 20	40	49	267	320	373
Uncoated $^{L}/_{D}$ 40	56	62	267	320	373
Al_2O_3 Coated $^{L}/_{D}$ 20	43	250	88	105	123
Al_2O_3 Coated $^{L}/_{D}$ 40	75	250	138	166	194

Table 4.1: Listed values of applied MCP voltage based on PAC and voltage dividing resistor setup.

ESA) tied to the PAC so the steering of the interior particles is the same as for the carbon foil. Spatial limitations then limited us for the return path for the bottom face of the MCP, so it was tied via resistive balance to the path associated with the top face of the heritage Chevron MCP stack. The final associated voltage drop across this MCP thusly follows the following relationship: $V_{MCP} = 0.06V_{PAC} \cdot \frac{R_{MCP}}{R_{MCP}+R_{BAL}}$ where R_{MCP} and R_{BAL} denote the MCP and balance resistor values, respectively. The values were chosen such that each MCP tested operated in an unsaturated mode; in other words, the applied voltages were kept far below levels needed for saturation to occur. Typical values used for the modified CODIF instrument are included in Table 4.1.

First tested was an uncoated MCP with $L/D = 20$ ratio. This MCP has a $25\mu m$ pore diameter spaced such that the total Open Area Ratio (OAR) is 63%. An MCP with $L/D = 20$ and coated with $60\,\mathring{A}$ of Al_2O_3 replaced the previous MCP, and underwent the same tests. The MCPs used are shown in Figure 4.1, taken with a SEM.

After the spectra with the MCP displayed an efficiency dependence on the ESA voltage, we tried a ratio $L/D = 40$ uncoated MCP. This ratio constrains the pore sizes to smaller sizes, increasing the OAR to 66% for the ions to travel through, as well as lower the maximum allowed angle for a particle to not interact with the MCP channel wall. With this, we expect

the efficiencies to be higher than with lower L/D ratios, due to more probability of interaction with the wall of the MCP channel.

To illuminate the detector with ion beams over a wide range of species, we used a $1-40\,keV$ duoplasmatron located in Morse Hall at the University of New Hampshire. With the engineering copy of CODIF, a pair of pixels of CODIF will be selectively illuminated with these different ions via duoplasmatron for an efficiency range over different MCP and PAC voltages, along with a nominal time of flight spectrum. The entrance system will be replaced in one pixel, exchanging the carbon foil for an MCP, seen in a diagram depicted in Figure 4.2. These tests will be run for these changes over various MCP coatings.

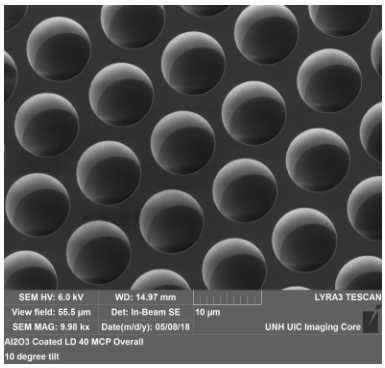

(a) SEM image of the $60\,\dot{A}\,Al_2O_3$ coated $^{L}/_{D}$ 40 microchannel plate used in CODIF.

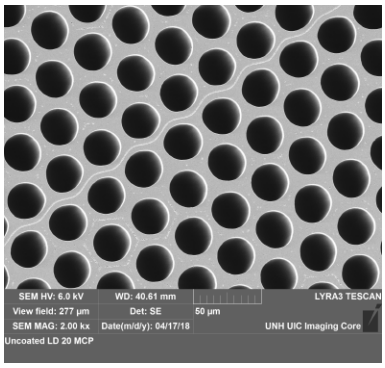

(b) SEM image of the uncoated $^{L}/_{D}$ 20 microchannel plate used in CODIF.

Figure 4.1: SEM image of the different microchannel plates used in CODIF. Note that these SEM images will not show the detail of the microchannel wall coatings, due to limitations for the SEM beam in geometry and energy ranges.

CODIF is mounted inside the vacuum chamber on a rotary table, which provides full rotation over the range of active quadrants. The duoplasmatron produces and aims a stable, monoenergetic beam of plasma directed at the ESA of CODIF, illuminating one pixel at a time governed by this rotary table. Combinations of internal gain, surface scattering, and external electronics yield ToF spectra dependent on the presence of the carbon foil or the MCP as a scattering surface.

A faster, more sensitive ToF electronics will provide us with more details of the temporal relationship of the ion distribution function, which is the result of many kinetic processes

in space. The prototype fast electronics being tested show a preliminary response time of a ToF output occurring 200 ns after a valid pair of events are received, which implies a data processing rate approximately 5-10 times faster than the heritage CODIF instrument at launch.

Ions tested for instrument efficiency include the particles listed in 4.1.1. These ion species were collected at two different initial energies, 5 keV and 10 keV except for hydrogen, which is over the range 15 keV and 10 keV due to limitations with the duoplasmatron source producing these low energy, light ions. Protons undergoing impact ionization at 5 keV have a significantly reduced scattering cross section as seen in Section 2.3.1, inhibiting the creation of a plasma beam at this energy. For all ions, the PAC of CODIF ranged from 10, 12, and 14 keV, with some measurements with the MCPs at lower PACs for proof of concept.

Results are compared between two canonical segmented sections, or pixels, of the CODIF instrument. A photo and schematic depicting each 22.5° pixel is illustrated in Figure 4.2. It was designed with a 3 cm ToF drift chamber, $\sim 3.0\ \mu g/cm^2$carbon foils at the entrance. Resulting spectra observed from the plasma beam illuminating a MCP is collected from the modified Pixel 7, and compared against the carbon foil canonical counterpart from Pixel 5 utilizing the same ion beam. This process was repeated over a selection of different MCPs, including: an uncoated $^{L}/_{D}\,20$, an uncoated $^{L}/_{D}\,40$, a 60 Å aluminum oxide coated $^{L}/_{D}\,20$, and a 60 Å aluminum oxide coated $^{L}/_{D}\,40$.

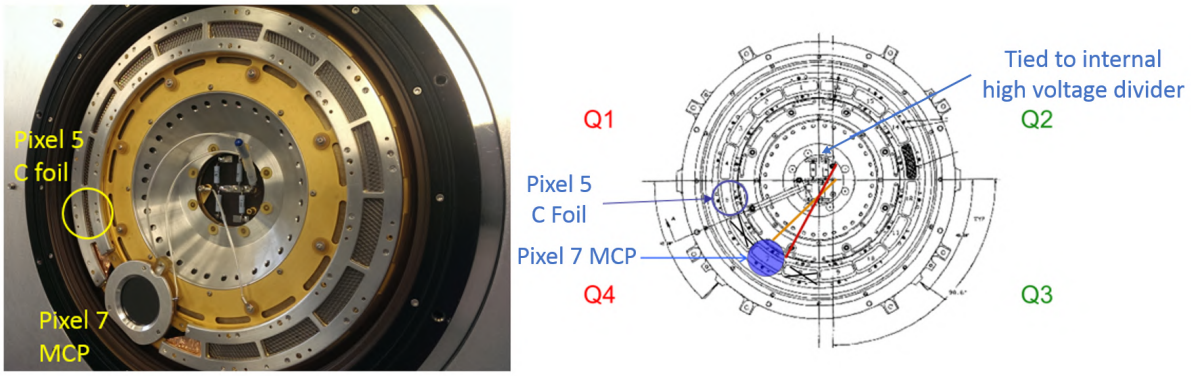

Figure 4.2: Internal entrance system to the ToF drift chamber of the active canonical pixels used in this experiment. Particles must first navigate the ESA before they interact with either the carbon foil in Pixel 5, or the MCP in Pixel 7, both located in Quadrant 4 of the detector.

4.2.2 Duoplasmatron Plasma Source

For fine plasma control, a duoplasmatron under high vacuum ($\sim 2-7\ \mu Torr$) is used, depicted in Figure 4.3. It implements a Wein filter to screen for ion species far before the plasma beam illuminates CODIF. As this operates by impact ionization of argon, argon spectra is taken in addition to the commonly seen ions. The plasma extraction voltage source allows for production of ions with kinetic energies per charge between 1 keV/e and 40 keV/e. The duoplasmatron is also outfitted with an ESA of its own, as well as an Einzel lens to focus the beam of plasma to allow for fine plasma control.

First, the cathode of the duoplasmatron is a hot filament thermionic emitter in ambient air under high vacuum. A platinum gauze coated with a proprietary blend of carbonate compounds is subjected to AC electric heating, which converts the blend of carbonates into oxides. These oxides aid in the thermionic emission process, and many electrons are liberated from the filament. These electrons are confined via electromagnets, and then elastically collide with any gases present, ionizing the gas proportional to the collisional cross-sections for each particle. However, notably argon is much easier to ionize due to its large cross-section, and its cross-section of ionizing other neutral gas particles is very large. As such, the system uses an argon leak gas primarily, with the option to leak in trace amounts of

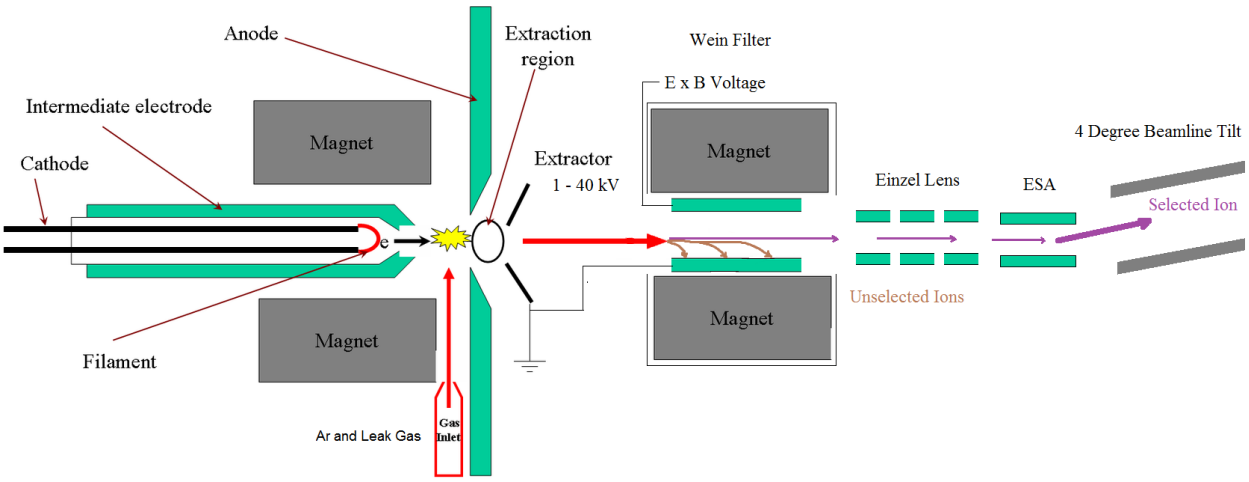

Figure 4.3: Simplified diagram of argon impact ionization and electromagnetic optics inside the duoplasmatron located in Morse Hall at UNH.

gases not normally present, like hydrogen and helium. For reference, argon is the only gas required to produce plasma beams of particles found in ambient air. Next, all the ions are accelerated to the desired energy by an electrostatic extraction voltage, where they pass through a Wein filter. This filter applies a constant magnetic field B with an adjustable voltage (which induces an electric field E), with ions left unperturbed if they satisfy the velocity relationship $v = E/B$ and steers all other ions out of the beam path. Since the velocity of the ions is mass dependent up to this point, we effectively select for ions with appropriate mass. Here the ions are optically steered to a proper beam diameter by the Einzel Lens. After this, the remaining selected-for ion specie encounters an Electrostatic Analyzer (ESA) that deflects the plasma beam based on its energy per charge down the center of the beamline. This part selects for the proper energy input, steering all other energies out of the beam path. Therefore, the plasma beam seen by CODIF is a monoenergetic plasma of one particular ion specie, dependent on the Wein Filter, ESA, and energy settings.

4.2.3 Parameters Under Investigation

For a ToF detector, some parameters are more significant for mass resolution than others. Under nominal operation, these parameters are critical to the successful operation of a ToF mass spectrometer:

- Total detected ion fluxes
- Residual energy of the primary ion
- FWHM of spectra

Requiring two consecutive detected events to measure a ToF hinges on detecting both events. Therefore, an adequate flux rate for Starts, Stops, and Valids (Start with an associated Stop) needs to be present. Production of a Start signal is dependent on initiating an electron avalanche from the primary ion. As a result, the emissive properties of the material and energy transfer are important. This energy transfer also directly affects the energy of the plasma distribution after collision, and more scattering that occurs this way affects the FWHM.

These parameters above are investigated using the ion source with the various MCP surfaces illuminated in tandem with the carbon foil. We also expect there to be a difference between the MCPs due to:

- L/D ratio, affecting the geometry
- Coating, affecting electron emissive properties

Expect the L/D ratio to govern maximum angle of impact, which implies altering the total interaction surface area and imposing a flux cutoff beyond a critical angle. In addition, we expect less energy lost to the more emissive coating as it is easier to excite an electron to vacuum. Simulations of these effects should offer more insight into the details of our measured data.

4.3 Significance of Detector Modification

4.3.1 Known Advantages and Disadvantages

MCPs are more durable than thin carbon foils. Operating under grazing incidence, the plasma's initial energy remains mostly unperturbed. Different coatings allow for subtle variances in detection efficiencies for various ions, which can be utilized in future detector designs. No dependence on a PAC directly lowers power requirements, which allows for a power supply with smaller mass onboard satellites and lowers flight risk. In addition to the detector modifications, a prototype fast timing electronic board will be tested. This prototype is designed to decrease "deadtime" between events registered and logic output.

Current NASA rocketry and propulsion technology to launch a typical scientific satellite into orbit is estimated at about $22,500 per kg of payload. Available power, volume and mass are subsequently prime real estate onboard a satellite. High voltage power supplies occupy a large volume, and its components typically result in a significant amount of mass in order to obtain the high voltages required of all the instruments. Reduction in the required voltage for the PAC would substantially reduce the accompanying power supply specifications. With less strict criterion for the power supply, mass and power consumption are both reduced. Devoto et. Al., 2008 demonstrated separation of N_2^+/O_2^+ without the need for a PAC[20]. Reduced power requirement correspondingly reduces the necessary supply payload mass.

MCPs operating under grazing incidence are heavily reliant on geometrical factors, including incident angle and energy. This heavily impacts the energy available to the valence electrons in the MCP pore wall, which in turn affects the secondary electron production and subsequently, the gain of the MCP. This results in a net efficiency for the MCP being much lower than for carbon foils. In addition, this dependence on available energy now implies that the applied ESA voltage influences the efficiency of the system, where with carbon foils the efficiency was uniform with ESA. This is because the ESA influences the trajectory of the exiting ion, while keeping the energy per charge the same. For a carbon foil, this makes

little difference, but the MCP is more sensitive.

4.3.2 Supporting Simulations

As the MCP has a plethora of different governing properties concerning both particle scattering as well as production of electrons, we simulated ToF spectra for all the ions used by the source. This includes utilizing SIMION software package to simulate the ion trajectories impinging on the MCP, followed by the scattering simulation using the software package SRIM/TRIM 2008. Both of these tools are described in Section 5.

First, MCPs are comprised of mostly open area, as the channels are thin, and at shallow angles. This makes MCPs very sensitive to angle of impact, whereas for the carbon foil, the minute changes in angular trajectory from the ESA are insignificant with respect to the scattering produced and subsequently are considered negligible. Scattering itself is modeled in SRIM/TRIM, which also depends on the structure and composition of the MCP, including any coatings if present. Therefore, we use the simulations to predict the responses from the various arrangements of MCPs, which in turn guide the choice of which MCP coatings and geometry to use.

5 Supporting Sensor Simulations

As mentioned previously, applied ESA voltages affect the exit angle of plasma ions. For the MCP, we studied the SIMION simulation of CODIF's ESA to extrapolate for MCP optimal angle tests, with SIMION introduced in Section 5.1 and the results discussed in Section 5.2. The exiting trajectories were fed as input to SRIM/TRIM to simulate experimental spectra, introduced in Section 5.3 and results discussed in Section 5.4.

5.1 SIMION Introduction

SIMION is a software package focusing on simulating charged particle optics. To this end, the software interpolates either 2D or 3D electrostatic and magnetic fields imposed by magnetic sources and applied voltages. First, the software solves the necessary partial and ordinary differential equations by the Runge-Kutta method. SIMION extrapolates the kinematics through straightforward finite difference methods from these numerical solutions to the Laplace Equation.

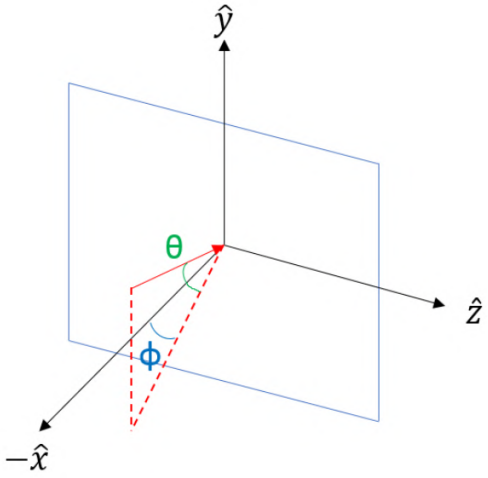

Figure 5.1: Coordinate system used in SRIM simulations, with a typical trajectory of an ion depicted.

Using this information, SIMION then tracks the particle trajectories as they traverse these fields[18]. The coordinate system used within SIMION is shown in Figure 5.1.

5.1.1 SIMION Basics

SIMION starts from the electrodynamic basics. Using the Lorentz Force in Equation 5.1, the acceleration of charged particles can be calculated from the fields themselves.

$$\vec{F} = q\left(\vec{E} + \vec{v} \times \vec{B}\right) \tag{5.1}$$

However, the fields need to be derived. The fields are extrapolated by numerically solving the Poisson equation in Equation 5.2 for a scalar electric potential field ψ, electric permittivity ϵ, and total charge density ρ:

$$\nabla^2\psi = -\frac{\rho}{\epsilon} \tag{5.2}$$

5.1.2 SIMION Setup and Assumptions

A SIMION simulation of the ESA and CODIF was developed during design of the instrument. Using these base files, the output distribution of ions from the ESA were examined for nominal CODIF operation at typical values. Simulated duoplasmatron source plasma beam is Gaussian distributed in energy and in angle. Simulations used source with a standard deviation $\sigma_E = \pm 100\, eV$ for energy and for $\sigma_A = 5^o$ half-angle. The simulation closely mimicked present beamline operating conditions, and assumptions chosen accordingly:

1. 5 keV beamline center energy, ± 100 eV normally distributed
2. 5°normally distributed in half-angle cone of plasma, originating far from the instrument
3. ESA is only dependent on effective energy per charge $^E/_q$ so all charged ions of the same energy per charge follow nearly-identical trajectories

5.2 SIMION ESA Electrostatic Simulation Results

This thesis aims to observe the improvements in resolution offered by utilizing MCPs under grazing incidence as a replacement for carbon foils in the CODIF instrument. Grazing incidence operation is subsequently extremely dependent on the angle of the impinging particles, as it affects the scattering experienced and the energy exchanged into producing electron showers from the MCP. Consequently, the exit trajectories of ions out of the ESA were sim-

ulated using SIMION. While the carbon foil is relatively unaffected by minor changes in angle, the MCPs exhibit a much different response.

5.2.1 ESA Trajectories of Exiting Particles

ESA simulations using SIMION investigated the exit trajectories dependence on the effects of applied ESA voltage, and incident plasma beam energy. Since the ESA functions on effective energy per charge, the exit trajectories do not vary significantly due to the ion's mass [24][73].

The simulation closely mimicked present beamline operating conditions:

1. 5 keV beamline center energy, ± 100 eV normally distributed

2. 5°normally distributed cone of plasma, originating far from the instrument

Charged particles have their trajectories tracked by the program as the applied potentials and initial beam energies are varied. Figure 5.2 depicts the trajectories of 100 N_2^+ ions, Gaussian distributed around $5250 \pm 200\, eV$ in energy and around 10^o conic half-angle. These trajectories were then tabulated over the different potentials and initial beam energies to put together a picture of the distribution of ions that exit the ESA.

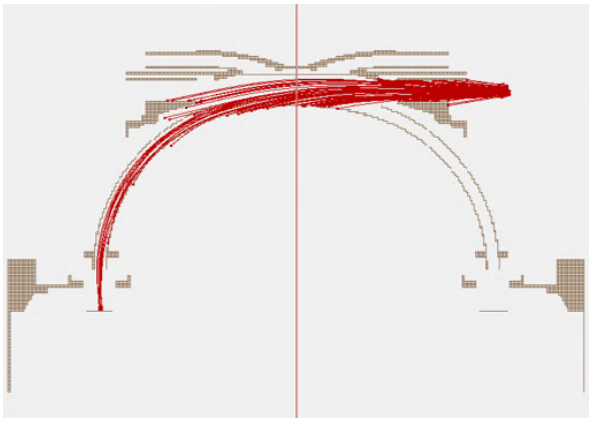

Figure 5.2: Trajectories of 100 N_2^+ ions through the ESA are illustrated above, simulating nominal operation. Ions are Gaussian distributed around $5250 \pm 200\, eV$ in energy and fill a 10^o conic half-angle.

Given the N_2^+ trajectory scheme, the simulation was repeated for a larger sample size of protons. Recall that the steering effect is dependent on effective E/q ratio, so protons will exhibit the same deflection as singly ionized N_2^+. A sample of 100000 protons with the distribution $5000 \pm 100\, eV$ normally distributed in energy, and normally distributed 10^o conic half-angle was simulated as the ap-

plied ESA voltage was varied from $-620\,V \geq V_{ESA} \geq -680\,V$ in $10\,V$ steps, with the PAC held at $10\,kV$. The angular distribution out of the ESA was tabulated over each voltage setting of the ESA, and the results plotted in Figure 5.3.

Figure 5.3 elucidates three important trends. First of which, the profile of the exiting particles is a Gaussian distribution, with a median peak that shifts as the ESA voltage is changed. Using the specifications for the ESA in the instrument, the median voltage for it is 650 V, and here the simulated ions have nearly parallel (0^o elevation) trajectories, as expected. Second, the number of ions that successfully exit the ESA diminishes as the voltage applied extends further out from that corresponding to beam center energy. Finally, The design of the ESA imposes a bounding limit of $\pm 5^o$ and any angle beyond that is lost as the ion collides with one of the ESA surfaces.

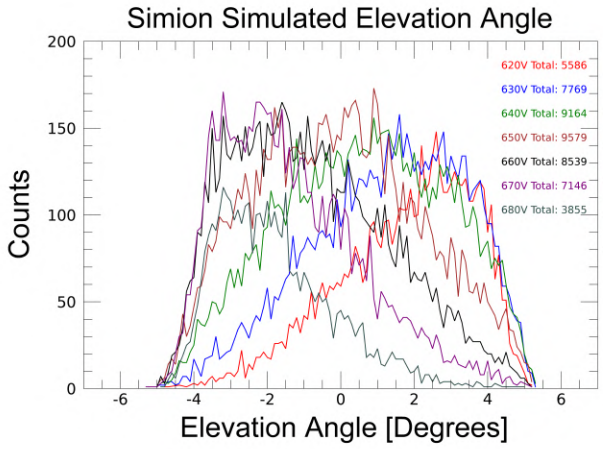

Figure 5.3: Distributions in exit elevation angle of 100000 protons of $5\,keV \pm 0.1\,keV$ energy originating in a 10^o cone outside the ESA entrance. Of the 100000 protons simulated, note only a small fraction successfully traverse the ESA.

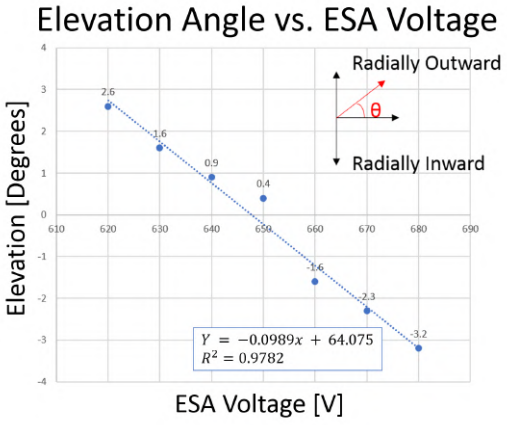

Figure 5.4: Linear fit of the peak of the angular distribution as a function of ESA voltage applied.

While the traditional carbon foil is insignificantly affected by angle of incidence, grazing incidence operation of MCPs is highly sensitive to this impinging angle. This directly corresponds to energy deposited into the MCP on collision, depth of penetration of the ion, and changes the scattering cross section. Due to polar symmetry of the instrument, the radial (or elevation)

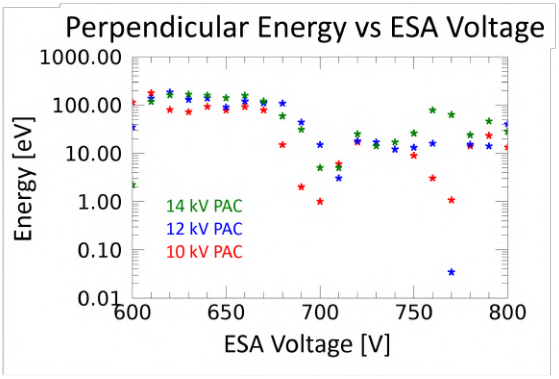

(a) Perpendicular energy [eV] of the simulated particles vs ESA voltage for a Gaussian distributed plasma beam of 5450 eV for the beam center, with PAC changes.

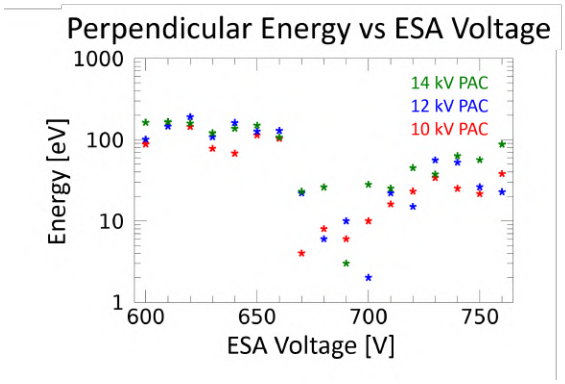

(b) Perpendicular energy [eV] of the simulated particles vs ESA voltage for a Gaussian distributed plasma beam of 5250 eV for the beam center, with PAC changes.

Figure 5.5: Perpendicular energy [eV] of simulated particles vs ESA for two differing beam energies.

angle is the most significant component. Peak elevation angle does observe a linear trend, which is plotted out in Figure 5.4. Using this information, the perpendicular component of the energy, or the amount of energy available to be deposited into the subsequent microchannels (perpendicular to the x axis in Figure 5.2), can be calculated and are depicted in Figures 5.5a and 5.5b.

Resulting components become the initial conditions for SRIM/TRIM, as the next stage in detection is the response of the entrance system. The simulation will track the ions through both a thin carbon foil as well as a coated and uncoated MCP. For the carbon foil, the ion's exit trajectory and remaining energy are logged by the simulation, as well as significant electronic data for production of secondary electrons.

Figures 5.5a and 5.5b depict the simulated trends of incident ions in the perpendicular direction; in this case it would be directly into the channel walls of a MCP. This also represents the maximum component of the energy that is available to the MCP as the ion scatters. In Figure 5.5a is the simulated trend in the perpendicular energy component of the impinging ion for a center beam energy of 5450 eV. For the ESA, recall the geometry was constrained such that $eV_o = 0.13E_o$ which implies the center beam energy would nearly

perfectly follow the curvature of the ESA at 708.5V. Notice how for all PAC energies there is a minimum in perpendicular energy, implying the bulk of the plasma beam exits the ESA very close to normal to the detection medium below, in our setup this is a MCP face. Also, for all but the highest PAC there is another drop-off in perpendicular energy near 770V, which due to the design of the ESA would imply a plasma beam energy around 5925 eV in the regime near this drop-off in perpendicular energy.

However, the PAC influences this energy too; notice the minimum of perpendicular energy begins to shift higher a few Volts in the ESA as the PAC is increased. The larger PAC is causing greater acceleration towards the detection areas, inevitably causing the otherwise uniformly deflected beam to deviate with the PAC. Figure 5.5b shows the simulated response to a slightly lower energy of plasma beam. The beam center would be perfectly deflected at 682.5V but the PAC again causes it to vary slightly.

5.2.2 SIMION Simulation Summary

As the simulations depict, the ESA voltage applied governs the exit trajectory of the plasma distribution illuminating it. Increasing the voltage applied against a monoenergetic beam of plasma causes the ions to be deflected inwards a few degrees, and the inverse is also true. For the traditional carbon foil, this is insignificant. The energetic losses and deviation in trajectory from scattering processes inside the foil dominate and vastly outweigh those caused by a shift of a few degrees of the impinging particle.

However, this is not the case for MCPs. Angular changes of this magnitude drastically change the properties of the specular scattering. Mentioned previously, the angle of incidence governs the available energy that can transfer from the ion into the MCP. In addition, the volume of material the primary ion can interact with changes with angle as well. A more shallower angle means that the depth of penetration is diminished, but the interaction length parallel to the pore is increased accordingly. Subsequently, the angle of incidence plays a critical role in the transfer of energy and production of secondary electrons. As a result,

the variance caused by the exiting ESA distribution will significantly affect the ToF spectra acquired from MCPs.

5.3 SRIM/TRIM Introduction

SRIM/TRIM was used for the simulations of particles on the MCP at solar wind energies. Within this $1\ eV \leq E \leq 40\ keV$ energy range, surface scattering becomes the dominant effect. SIMION results fed into SRIM/TRIM for stochastic consideration of MCP surface interactions. Resulting energy and angular data were applied in the non-relativistic energy range over the CODIF drift chamber, generating a simulated ToF spectra.

5.3.1 SRIM/TRIM Basics

The program package works by approximating all the contributing physical mechanisms in Section 2.3.1 to obtain high computer efficiency while still maintaining accuracy[104].

First, TRIM tracks a large number of individual ions through a target material. Energy, position, and direction among other intrinsic data are stored for each ion. These properties change as the particle undergoes an ensemble of binary nuclear collisions during the simulation. Between collisions, the ion is assumed to move in a straight line to the next collision, dictated by the mean free flight path[104]. Energy is reduced by the simulated effects of nuclear and electronic stopping power, and when it sinks below a per-determined cut-off value, the program stops tracking the particle. This method is accurate up to a few $^{MeV}/_{amu}$ but ultimately falls off in accuracy as relativistic effects take over[104]. In addition, the program treats the losses from the different mechanisms differently, and are treated independently. Nuclear stopping power are discretized, and occur at each collision whereas electronic stopping power effects are continuously interacting.

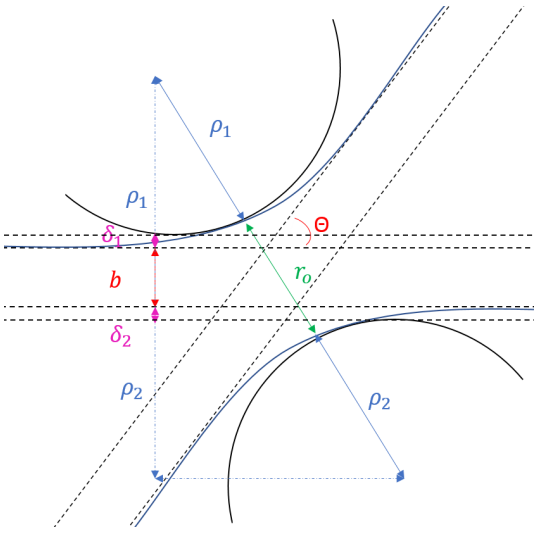

Figure 5.6: Scattering in the classical COM frame, showing the hyperbolic trajectories from the interaction potential, and superimposed with the "scattering triangle" with impact parameter b, distance of closest approach r_o, radii of curvature at closest approach ρ_1, ρ_2, respectively, and two small correction terms δ_1, δ_2.

SRIM Scattering Formula Earlier in Section 2.3.1 we discussed the basics of the Center of Mass (COM) reference frame. Scattering in the COM frame is constructed such that a trigonometry tool can be superimposed over the trajectories. The authors call this the "scattering triangle" and is comprised of the impact parameter b, distance of closest approach r_o, radii of curvature of the particles at closest approach ρ_1, ρ_2, respectively, and two small correction terms δ_1, δ_2. Illustrated in Figure 5.6, the scattering triangle allows for determination of the COM deflection angle Θ.

From the triangle, we obtain

$$cos\left(\frac{\Theta}{2}\right) = \frac{\rho + b + \delta}{\rho + r_o}$$

$$with\, \rho \equiv \rho_1 + \rho_2\, and\, \delta \equiv \delta_1 + \delta_2 \tag{5.3}$$

This illustration portrays two hyperbolic particle trajectories taken under classical mechanics, given by the blue curves. Approximating the trajectories at closet approach with circular paths allows for an analytic and significantly faster calculation without significant loss in precision. The small correction terms compensate for the circular assumption. In the CoM frame, the classical distance of closest approach equation becomes:

$$1 - \frac{V(r_o)}{E_C} - \left(\frac{p}{r_o}\right)^2 = 0\, and\, E_C \equiv \frac{E}{1 + {}^{M_1}/_{M_2}} \tag{5.4}$$

where $V(r_o)$ is the interaction potential between the two particles and E_C is the energy available in this COM system. TRIM solves this numerically via Newton's Method with two to three iterations to error margins less than 0.1%. With this formalism, the radius of curvature ρ can be rewritten using the centrifugal force f_C present within this frame[104],

$$\rho = \rho_1 + \rho_2 = {}^{\left(M_1 V_1^2 + M_2 V_2^2\right)}/_{f_C} = \frac{2\left(E_C - V\left(r_o\right)\right)}{-{}^{dV(r_o)}/_{dr}} \tag{5.5}$$

The authors of the program apply some convenient scaling factors to facilitate computations, such as the reduced energy ϵ and the screening length a. From earlier in this section, recall that these are given by:

$$\epsilon = \frac{aE_C}{Z_1 Z_2 e^2} \tag{5.6}$$

where e is the electronic charge, and Z_1, Z_2 are the atomic numbers of the incident and target particles, respectively. The screening length a is in reference to the Bohr radius a_o and is given by:

$$a = \frac{0.8853 a_o}{\left(Z_1^{2/3} + Z_2^{2/3}\right)} \tag{5.7}$$

All of these can be combined one more time to $B \equiv {}^{p}/_{a}$, $R_o \equiv {}^{r_o}/_{a}$, $R_C \equiv {}^{\rho}/_{a}$, $\Delta \equiv {}^{\delta}/_{a}$ to yield the formula:

$$cos\left(\frac{\Theta}{2}\right) = \frac{B + R_C + \Delta}{R_o + R_C} \tag{5.8}$$

This equation is significant because it allowed for the first time an analytic solution that could be done quickly to high accuracy[104]. All the simulation needs from this point is an expression for the error Δ. Here, Ziegler et al. found the best description followed

$$\Delta = A\frac{R_o - B}{1 + G}, \;\; A \equiv 2\alpha\epsilon B^{\beta}, \;\; G \equiv \gamma\left[\left(1 + A^2\right)^{1/2} - A\right]^{-1} \tag{5.9}$$

where

$$\alpha \equiv 1 + C_1 \epsilon^{-1/2}, \;\; \beta \equiv \frac{C_2 + \epsilon^{1/2}}{C_3 + \epsilon^{1/2}}, \;\; \gamma \equiv \frac{C_4 + \epsilon}{C_5 + \epsilon} \tag{5.10}$$

with fitting parameters $C_1 - C_5$ varying, depending on the potential to fit[104]. These formalisms make the backbone of the SRIM/TRIM simulation package, and facilitate the computations for every particle collision. However, this alone is not enough to allow reasonable computational times if the program has to calculate the scattering for each and every target atom along the path of the ion. An additional concept is needed, which the authors call the free flight path between collisions.

Free Flight Path The concept of the free flight path emphasizes reducing computational rigor by omitting certain calculations where the collisions transfer a negligible amount of energy and also have negligible angular deviations. This is accomplished using the free flight path, which calculates the maximum distance the particle can travel until there is one significant collision. Free flight path is dependent on many variables, and is treated statistically. First, there is a probability $W_1(b)\,\delta b$ for finding a target atom between radial impact distance b and $b + \delta b$ of[104]:

$$W_1(b)\,\delta b = 2\pi N L b \delta b \tag{5.11}$$

where L is the free flight path length, and N is the atomic density of the target. This probability is subsequently weighted by the probability $W_2(b)$ of not finding a closer target atom than at impact parameter b given by:

$$W_2(b) = e^{-\pi N L b^2} \tag{5.12}$$

These two probabilities can be convoluted together to find the closest atom between

radial impact distance b and $b + \delta b$ of

$$W(b)\,\delta b = W_1(b)\,W_2(b)\,\delta b = 2\pi b N L e^{-\pi N L b^2}\delta b \tag{5.13}$$

which can be parameterized in terms of energy. Aiding the calculation is the assumption that at high energies, the mean angular deflection per free flight path length is roughly constant[104], or:

$$\frac{M_2}{M_1}\frac{\Delta E_n}{E} = \frac{M_2}{M_1}\frac{L S_n(E)}{E} = constant \tag{5.14}$$

with ΔE_n being the energy transfer from nuclear collisions, and S_n the nuclear stopping power. TRIM then checks a balance condition, to see if the ion's energy change exceeds approx. 5% of its total energy, and if so, L is reduced to compensate. At low energies, this free flight path can become less than the target's interatomic distance. In this case, L is replaced by the mean atomic separation of the target $N^{-1/3}$ and 5.13 is replaced with:

$$W(b)\,\delta b = \begin{cases} 2\pi N^{2/3} b \delta b & for\, b < \pi^{-1/2} N^{-1/3} \\ 0 & for\, b > \pi^{-1/2} N^{-1/3} \end{cases} \tag{5.15}$$

Typically, TRIM calculates L by the impulse approximation, which is valid for any energy transfer T such that $T << E$ [104]. The impulse approximation posits that for Coulomb collisions, $sin^2\left(\frac{\Theta}{2}\right)$ can be reduced to an algebraic relationship with the reduced impact parameter $b' \equiv b/a$ and a to-be-determined function of the potential, $f\left(b'\right)$[104].

$$sin^2\left(\frac{\Theta}{2}\right) = \left(\frac{f\left(b'\right)}{2b'\epsilon}\right) \tag{5.16}$$

Which is subsequently reduced to

$$sin\left(\frac{\Theta}{2}\right) = \frac{f\left(b'_{max}\right)}{2\epsilon b'_{max}} \tag{5.17}$$

From earlier in Section 2.3.1, recall that the transferred energy is:

$$T = \gamma E sin^2\left(\frac{\Theta}{2}\right) = \gamma E\left(\frac{f\left(b'\right)}{2b'\epsilon}\right) \Rightarrow \left(\frac{\epsilon_{min}}{\gamma\epsilon}\right)^{1/2} = \frac{f\left(b'_{max}\right)}{2\epsilon b'_{max}} \tag{5.18}$$

With these expansions, the simulation can accurately track the transfer of energy at each collision relatively simply, saving computation time. Electronic energy loss is then the result of $\Delta E_e = LNS_e\left(E\right)$ with the electronic stopping power $S_e\left(E\right)$ described in Section2.3.1.

5.3.2 SRIM/TRIM Setup and Assumptions

Resolution of mass spectrometers in energy, time, and space all have one constituent in common; scattering of the ions to be detected leads to less accurate data and a reduction in resolution capabilities of the instrument. For these simulations, only the scattering effects have been considered. Electron emission from the base lead silicate material, as well as coatings such as magnesium oxide, tungsten, and aluminum oxide have been described in great deal by the previous works, such as those of [64, 39, 6, 22].

Ions impinging on the wall of a MCP pore can be approximated as planar at this energy and geometric scale. Depicted in Figure 5.7 is the coordinate system used in these simulations with a coated MCP. The simulations were run with the following ions: H^+, He^+, N^+, O^+, Ar^+ over the same energy ranges as the CODIF experiments, including 15, 17, 19, 20, 22, and 24 keV for all ions except protons, with protons ranging from 20, 22, 24, 25, 27, and 29 keV due to the relative difficulty in producing and ion optics of low energy protons with the duoplas-

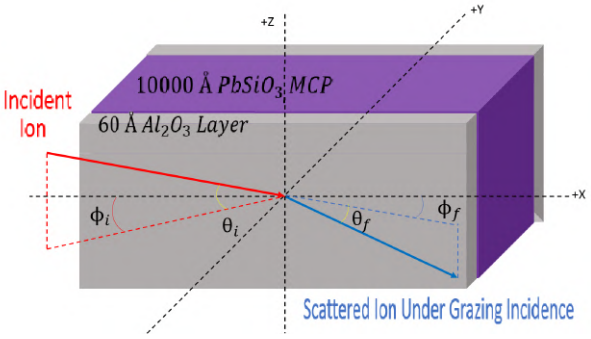

Figure 5.7: Coordinate system used in SRIM simulations of ion interactions with the coated MCP. A planar symmetry was used to approximate the microchannels at the atomic scale. The layer of aluminum oxide is 60 Å thick on top of the lead silicate MCP, which has an inter-pore spacing of 1 micron (10000 Å).

matron. For these simulations, the impinging ion was kept at a constant energy, and the incident angles ϕ_i, θ_i were iterated through. 50000 ions per species were launched at each angular step from $\phi_i \in \{0.1^o - 4.85^o\}$ in 0.25^o steps, and θ_i held constant at zero degrees.

The assumptions guiding these angular ranges are twofold: first, the $^L/_D$ ratio governs a maximum angle per channel which is typically less that 3 degrees, and second, particles exiting the ESA are Gaussian distributed near parallel to the x axis, and then enter a microchannel which has cylindrical symmetry - therefore the z displacement component will be negligible, and a suitable rotated reference frame can be chosen to extrapolate the influence of the z component.

However, SRIM only takes into account the actual collisions. There is a purely geometrical component that arises from tilting straight-channel micropores. As seen in Figure 5.8, the two openings of the same diameter are shifted with respect to the length L of the channels and the angular displacement θ. Therefore as the angle is varied, the fluxes of ions will change accordingly. By approximating these openings as circular (they become "compressed" in the axis of the tilt, and are more closely modeled by ellipses), we can arrive at an analytical result. First, recall the classical overlapping-circles geometry problem has a solution of:

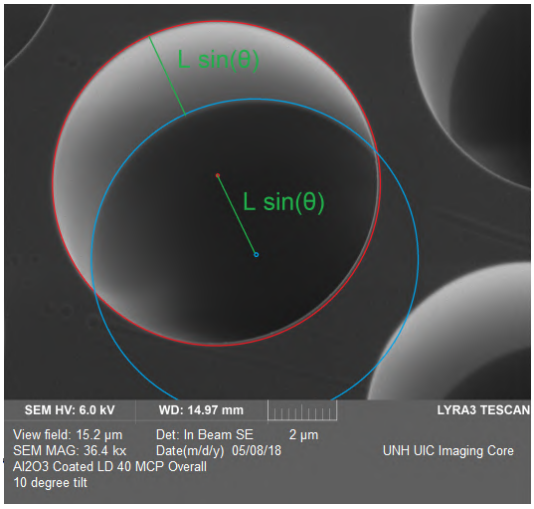

Figure 5.8: Geometrical effect of tilting a microchannel array. It creates a shifted 2-circle overlapping problem.

$$A_{Overlap} = r_1^2 cos^{-1}\left(\frac{d^2 + r_1^2 - r_2^2}{2dr_1}\right) + r_2^2 cos^{-1}\left(\frac{d^2 - r_1^2 + r_2^2}{2dr_2}\right) - \sqrt{(-d + r_1 + r_2)(d - r_1 + r_2)(d + r_1 - r_2)(d + r_1 + r_2)} \quad (5.19)$$

Now in our general case, the entrance and exit of the pores are identical, or $r = r_1 = r_2 =$

$^1/_2D$ (with D being the diameter of the pore) but are shifted by the tilt. As can be seen in Figure 5.8 as well, is the shift is easily described by $Lsin\,(\theta)$, which is both the distance the centers of these circles are shifted, and the projected width of the microchannel's interaction area. Consequently, $d = Lsin\,(\theta)$ as well. Plugging this back into Equation 5.19 we then arrive at a simplified expression

$$A_{Overlap} = \frac{D^2}{2} cos^{-1}\left(^L/_D sin\,(\theta)\right) \tag{5.20}$$

From the result above, it is easy to get the remaining area of the interaction region A_I by subtracting this from the area of the entrance circle A_E

$$A_I = A_E - A_{Overlap} = \frac{\pi D^2}{4} - \frac{D^2}{2} cos^{-1}\left(^L/_D sin\,(\theta)\right) \tag{5.21}$$

Incoming flux of particles have a proportional chance to interact, or pass right through without interacting dependent on the ratio of the area of the interaction region A_I, and the total opening's area A_E. In other words, we define a fraction of flux that passes through the microchannel without interacting as $\eta = {}^{A_{Overlap}}/_{A_E}$ and subsequently the ratio that do interact is $\zeta = 1 - \eta = {}^{A_I}/_{A_E}$. Therefore, we obtain

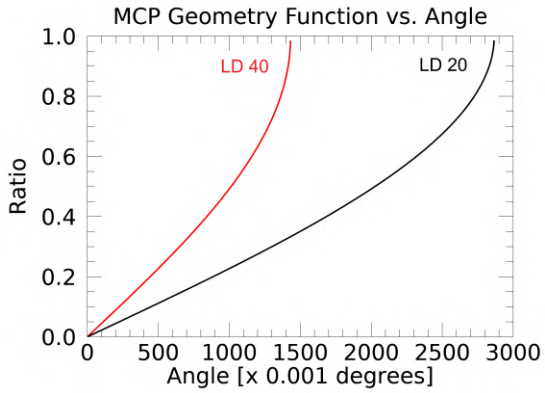

Figure 5.9: Plot of ζ as a function of angle for the two aspect ratios tested in CODIF, an $^L/_D$ 20 and an $^L/_D$ 40.

$$\zeta = 1 - \frac{2}{\pi} cos^{-1}\left(^L/_D sin\,(\theta)\right) \tag{5.22}$$

Note how Equation 5.22 depends on both the aspect ratio and the tilt angle of the MCP. This function is plotted in Figure 5.9. This ζ function has a cutoff, which is dependent on the aspect ratio of these MCPs. The cutoff occurs when the tilt of the MCP pore causes the

interaction region to completely eclipse the exit opening of the channel, where every particle is guaranteed to interact with the microchannel wall material. Eclipsing and the subsequent cutoff occur at the angle of

$$\theta_C = tan^{-1}\left(\frac{1}{L/D}\right) \tag{5.23}$$

Recall the assumption that the L/D ratio governs the angular range of accepted ions. Equation 5.23 gives the cutoff for which interaction with the MCP is guaranteed. This angle, which is L/D dependent, is used in the calculation of geometrical effects in the sections to follow.

5.4 SRIM/TRIM Scattering Calculation Results

Results of SRIM/TRIM calculations for a steady, monoenergetic beam of plasma are presented in the following sections. SRIM/TRIM simulation sets mimic CODIF experimental tests, and are comprised of the four ion species H^+, He^+, N^+, Ar^+ over the same total energy ranges used, which is $E_T = \{15, 17, 19, 20, 22, 24\}\ keV$ for ions other than protons, and $E_T = \{20, 22, 24, 25, 27, 29\}\ keV$ for protons. Plasma is then simulated to impinge onto the inner wall of a MCP pore, approximated as a plane for simplicity. Simulations were done for a bare lead silicate MCP $1000\,\mathring{A}$ thick, one with a $60\,\mathring{A}\ MgO$ layer coated on top of the base MCP, and one with a $60\,\mathring{A}\ Al_2O_3$ layer coated on top of the base MCP. Incident angle of the ion varied from $0.1^o - 4.85^o$ in 0.25^o steps, and each step collected data of 50000 separate ions.

5.4.1 Simulated SRIM Spectra

SRIM/TRIM calculated the scattering of each individual ion, and output the ion's final energy and trajectory after interacting, as well as flux data. Both these parameters are then subsequently used to generate a simulated ToF spectra within the CODIF instrument by enforcing a $3.00\,cm$ flight path in the direction parallel to the surface. By varying just

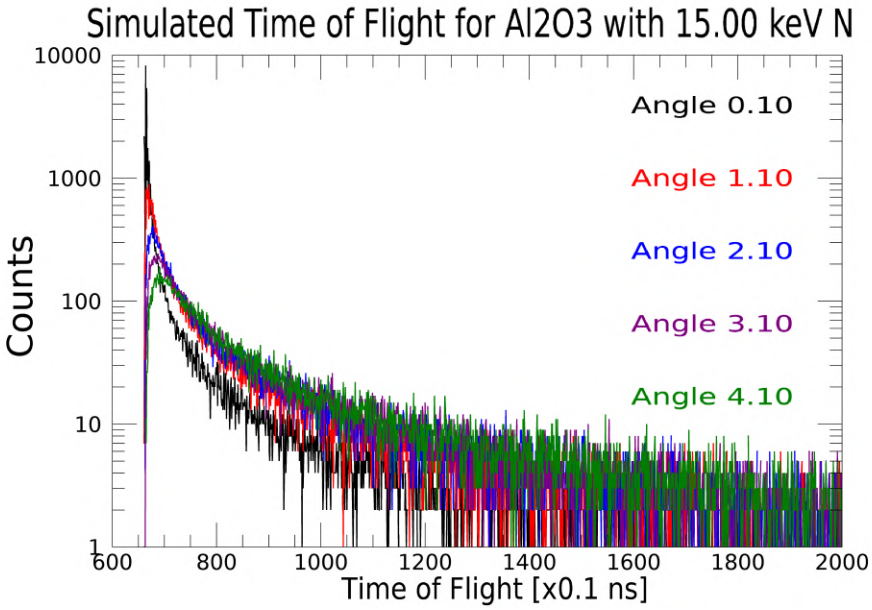

Figure 5.10: SRIM simulations of $15\,keV\,N^+$ over a range of incident angles onto a 60 Angstrom layer of aluminum oxide over a traditional lead silicate MCP.

the angle over the range of energies used in the experiments, the angular effects can be investigated. Raw SRIM calculations of a select few angles for a steady, monoenergetic beam of nitrogen is given in Figure 5.10. A monoenergetic 15 keV beam of N^+ impinges onto the inner wall of a MCP pore. This has a $60\,\mathring{A}\,Al_2O_3$ layer coated on top of the base MCP lead silicate material, which is $1000\,\mathring{A}$ thick. As mentioned previously, incident angle of the oxygen ion varied from $0.1^o - 4.85^o$ in 0.25^o steps, and each step collected data of 50000 separate ions. Section 5.3.2 talks about the assumptions as well as accounting for the effects of geometry. Flux results have been adjusted according to the geometrical effects and split into an $^L/_D$ 20 and $^L/_D$ 40 set, using Equation 5.22.

Plotted in Figure 5.10 are only a select few angular data sets for clarity. However, what can be seen are two major, important trends:

1. Centroid of the spectra increases as the angle of incidence increases

2. FWHM of the spectra increases as the angle of incidence increases

ToF centroid and FWHM changes with angle are indicative of changes in the amount of energy transferred and range of energy transfers, respectively, from the ion to the top layers

of the MCP plus coating, if present. First, the incoming angle highly constrains the scattering processes acting on the ion. More oblique angles cause more dispersion of the ions spatially, and cause the ions to lose more energy in the collisions which increase the transit time. The larger angle also causes the ensemble average exit angle to increase as well; this off-axis trajectory means the ions will take longer to reach the end of the 3 cm flight path and increase the transit time accordingly. The net result of both of these impose a larger FWHM and long decay tail of the spectra.

These following paragraphs and figures in Appendix B depict a wide array of salient details concerning the spectra for ions in SRIM/TRIM. These are investigated and separated by coating of MCP. Influence of the incident angle on the spectra parameters were investigated, iterating over all the energies that are used experimentally in this work. Spectra details include the resulting centroid of the time of flight spectra (residual energy retained by the ion), the FWHM imposed, and numerous important flux rates. Of these flux rates, particular attention was given to the successful grazing ions, the backscatter flux back the way it came and out of the MCP, and the rate of particles that are scattered beyond the CODIF detection limits of 300 ns ToF. From these we can also calculate the number of implanted ions.

Uncoated Standard MCP Figures B.1 - B.4 depict the net trends of the ions impinging on an uncoated lead silicate MCP, covering protons, helium, nitrogen, and argon, respectively. These trends include position of ToF centroid, spectra FWHM, throughput flux, backscattered flux, and the flux of particles scattered beyond recognition, or the straggling ions. These straggling ions are plasma that have been scattered to the point where the residual energy they retain causes the ToF to be longer 300 ns, which is the cutoff for the electronics of CODIF.

What can be seen are the following trends. First, for all ions simulated, total initial energy does not affect the total number of ions successfully grazing off the surface. All

energies are within 1% or less of each other in terms of specularly reflected ion flux. $^{L}/_{D}$ ratio as well as angle of incidence is much more significant. Second, backscatter and straggler flux rates observe a mass dependence. Heavier ions are more susceptible to straggling as well as backscattering back out the way the ions entered than light ions. Finally, the FWHM for all ions are relatively static, variances of about 10% are seen across different masses. Energy slightly changes these values as well, with an increase in energy typically reducing FWHM by a marginal amount. The major contributor is the angle of incidence. Finally, the centroid of the distribution has a slight angular dependence. Increasing obliqueness of the angle of impact shifts the centroids to longer ToF values. Energy is more significant for centroid energy due to the relationship of the ToF to the energy.

MgO **Coating** Figures B.5 - B.8 depict the trends of the magnesium oxide simulations for protons, helium, nitrogen, and argon, respectively. Similar to the above no-coating results, these ions closely mimic the observed trends of the uncoated MCP. Distinct angular dependence affects all ion's centroid values, FWHM, total grazing particles, backscatter, and straggling ions. For each ion, there is a noticeable split between the effects of geometry of the $^{L}/_{D}$ 20 and $^{L}/_{D}$ 40. The narrower MCP of $^{L}/_{D}$ 40 trends towards a larger change over all the parameters listed above over a smaller change of angle of incidence, making it more sensitive to angular changes.

Compared against the standard, uncoated MCP, the addition of magnesium oxide subtly changes the observed tendencies listed above. First, the centroids in time of ions scattering off the *MgO* coating are marginally slower than that of the uncoated MCP, for the majority of ion masses and energies. Only a few low energy, high mass ions are sporadically better performance than either the aluminum oxide or uncoated MCP. Additionally, the FWHM suffers as a result of the scattering. This response in energy, mass, and angle makes this coating perform the worst of the MCPs in general. Flux rates are relatively consistent between the coatings; there is no significant difference in rates of any particular ion and are

all within 1% of each other regardless of coating. This, again, lends support to a purely angular driving force behind the scattering effects.

Al_2O_3 **Coating** Figure B.9-B.12 shows the simulated ToF spectra of protons, helium, nitrogen, and argon, respectively, over the typical ranges used in CODIF. Simulations show the following trends in the ToF spectra.

These figures depict the trends of the spectra in time. SRIM offers the ability to look at the ensemble averaged energy deposition per depth. Energy transferred to the electron cloud and exchanged in a nuclear recoil collision both as a function of depth are obtained and plotted in the following figures (Figures B.9-B.12). These figures illustrate again just how similar all the MCP coatings behave. Addition of aluminum oxide influences the observed energy and FWHM tendencies, contrasting against the uncoated and magnesium oxide MCPs. Most importantly, the centroids in time of ions scattering off the alumina coating are marginally faster than that of any other MCP for all ion masses and energies, barring a select few outliers at high energies and low mass. Consequently, the particles scattered off the alumina coating retain marginally more energy after the collision. Additionally, the FWHM resulting from the scattering is on the order of a nanosecond in favor of the alumina coating compared to that of the magnesia coating. However, the uncoated MCP FWHM is superior to that of the aluminum oxide, making this coating fair as a middle-of-the-road choice for scattering effects. In general, in terms of energy, mass, and angle, this coating's scattering performance is the best of the MCPs. Flux rates are relatively consistent between the coatings; there is no significant difference in rates of any particular ion and are all within 1% of each other regardless of coating. Again, this evidence is indicative of a purely angular driving force behind the scattering.

5.4.2 SRIM/TRIM Summary

Directly comparing the spectra of magnesium oxide and aluminum oxide in generated SRIM/TRIM spectra depict the following important details. More scattering occurs in MgO than Al_2O_3 as evidenced by the increased FWHM of the spectra, and centroid in ToF occurring at longer times. With a larger gain, and less variation due to scattering effects, aluminum oxide layer was chosen over the magnesium oxide to compare against the carbon foil and uncoated MCPs.

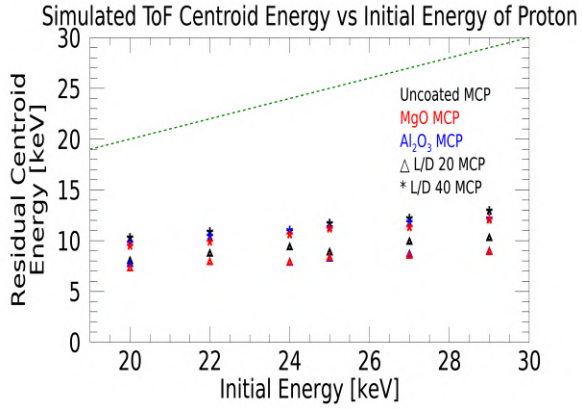

(a) SRIM/TRIM predicted residual energy of protons on all MCP surfaces, energies, and geometries.

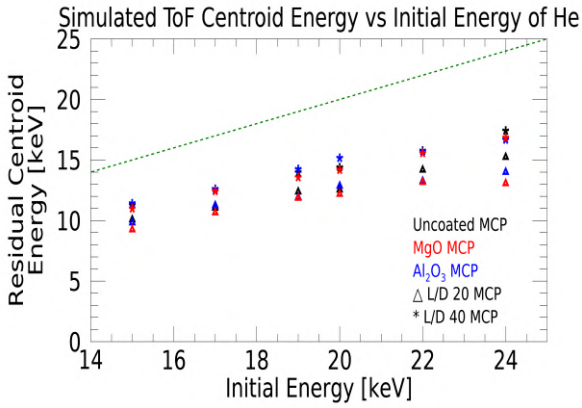

(b) SRIM/TRIM predicted residual energy of helium on all MCP surfaces, energies, and geometries.

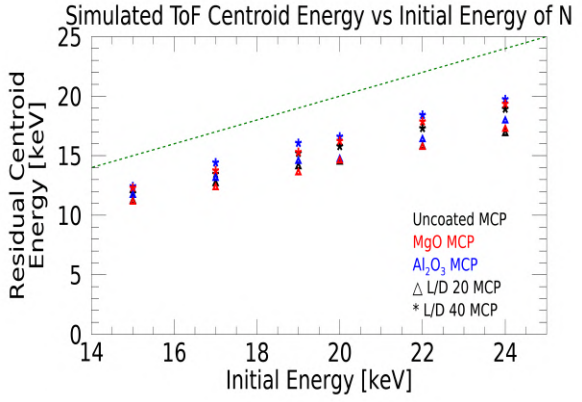

(c) SRIM/TRIM predicted residual energy of nitrogen on all MCP surfaces, energies, and geometries.

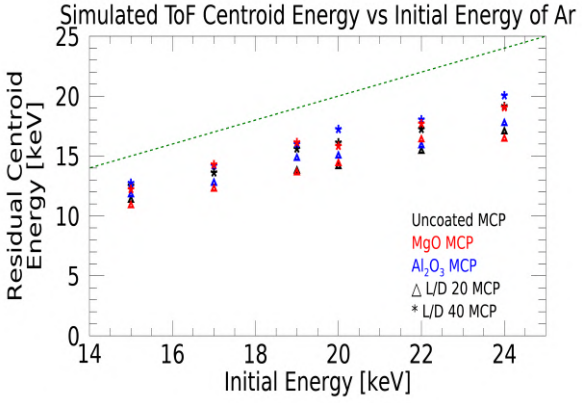

(d) SRIM/TRIM predicted residual energy of argon on all MCP surfaces, energies, and geometries.

Figure 5.11: Predicted energy retention of proton, helium, nitrogen, and argon plasma across lead silicate MCPs, aluminum oxide coated MCPs, and magnesium oxide coated MCPs. Geometry effects are accounted for.

Depicted in Figure 5.11 is the direct comparison of SRIM-calculated residual energy for each ion across each MCP under consideration, including geometrical effects. These are the energies that CODIF would register based on energy loss and trajectory after colliding with the MCPs. Three MCP materials are examined between the $^{L}/_{D}$ 20 and $^{L}/_{D}$ 40: one without a coating, one with a 60 $\mathring{A}$ layer of MgO, and one with a 60 $\mathring{A}$ layer of Al_2O_3. Recall the base MCP lead silicate material is assumed to be 1000 $\mathring{A}$ thick. Additionally, the $^{L}/_{D}$ ratio governs the maximum angle of grazing incidence that does not exhibit multiple scattering interactions with the MCP channel. For these MCP simulations, that means the $^{L}/_{D}$ 20 MCP experiences ions grazing at 2.85^{o} from normal to the surface, and the $^{L}/_{D}$ 40 MCP experiences ions grazing at 1.35^{o} from normal to the surface.

Two trends are immediately apparent. First, there is a schism between residual energy for all ions, between the $^{L}/_{D}$ 20 and $^{L}/_{D}$ 40. The $^{L}/_{D}$ 40 retains more of the initial energy than the $^{L}/_{D}$ 20, causing a separation, with the $^{L}/_{D}$ 40 being closer to the initial energy. Second, there is a mass dependence: as mass increases, the ion is observed to retain a larger fraction of its initial energy. Next, the Al_2O_3 coated MCP has slightly better energy retention than both MgO and no coatings, with outliers at high energies and low masses.

For the flux data, there is not much difference between the coatings. From the total spectra-producing flux observed, comparing individual ions in Figures B.1 - B.12. Looking specifically at B.1c, B.5c, and B.9c, for example, reveals protons have no significant differences among the constituent layers. Even the changes in energy only negligibly affected these rates. The driving force in this regard is purely angular. This is also seen in the backscatter and straggler plots, as well as for the remaining ions. The only major differences occur with mass, and that can be explained by the collision cross section. As the mass of the ion increases, the scattering cross sections for both electronic and nuclear interactions increase. This is partly due to increased atomic nucleus (and by extension electron cloud) size. As a result, more massive particles like argon are exponentially more likely to undergo scattering, which includes classical Rutherford backscatter back out the front of the MCP. Similarly,

the more massive ions also are more likely to be scattered to the point of straggling.

Additionally, MgO is much more reactive than Al_2O_3, particularly with water. In the lab, any and all modifications to the instrument have to be done on a workbench at atmosphere, which allows the water reactions to occur. Then upon reinstallation into a vacuum environment, the water will have to take a substantial amount of time to outgas. Furthermore, the now-present water layer becomes the first few layers of interaction with the MCP, and not the coating, effectively reducing the emissive properties of the MgO layer. As a result, we chose the aluminum oxide coating for the experiment.

6 Results and Discussion

Measured time of flight spectra basics and a baseline comparison with heritage data are discussed in Section 6.1. Following in Section 6.2 which compares the MCP responses to the carbon foils, and contrasts effects caused solely by the differing geometries as well as coatings. Next are the ion flux rate responses to the differing MCPs as well as carbon foil in Section 6.3. Due to the grazing incidence operation of MCPs, the angular dependence is significant, and discussed within Section 6.4. Finally, sources of error are addressed in Section 6.5.

Appendix A contains the time of flight spectra for all ions and energy ranges used in this thesis. Progression of the changes in time of flight spectra with energy are given in Appendix A.1 while the entrance system normalized comparisons are in Appendix A.2.

6.1 CODIF Spectra Baseline Results

The following Section 6.1.1 establishes a baseline of the instrument, by comparing current spectra taken with the carbon foil to that used to calibrate the flight model of CODIF in 1994. Afterwards, the basics of spectra dependence on initial energy are investigated in Section 6.1.2 in what is called a time of flight progression with energy. Section 6.1.3 goes over the basics of fitting all spectra, common among the carbon foil, uncoated MCPs, and coated MCPs. Finally, the energy losses from the time of flight spectra with initial energy are discussed in Section 6.1.4.

6.1.1 Comparison of Current Carbon Foil with Heritage Carbon Foil Spectra

To begin the comparison against the classical carbon foil, the current setup of CODIF carbon foils need to be verified. In other words, we investigate the differences, if any, of carbon foil spectra between the prototypes. Scattering on the same carbon foils used during calibration should be the same, with the only difference being the supporting electronics. First, we

show the current capabilities of modern CODIF with new timing electronics and compare with heritage ion data from at-launch CODIF. This is best accomplished by looking at the carbon foil data between the versions. Only difference between the current installment of CODIF and heritage are the electronics used to infer the ToF from the signals generated by the same thickness carbon foil. The latest version of the supporting electronics utilizes modern approaches to signal discrimination as well as generally faster components, allowing relative measurements accurate down to 100 picoseconds and allowing for a max flux rate of just about 3 MHz. At launch, the heritage version is accurate to approx. 0.2 ns at a maximum rate of 0.25 MHz.

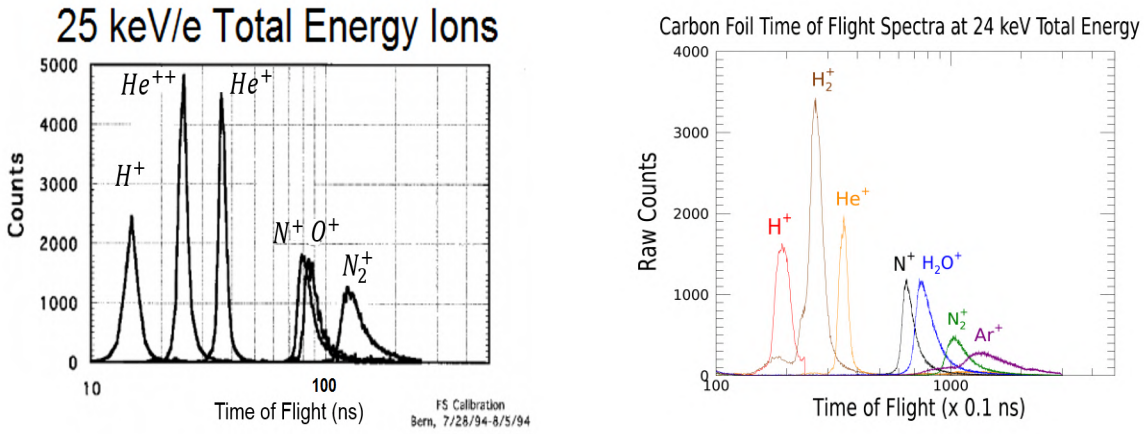

(a) University of Bern calibration of CODIF prior to launch.

(b) Current modification of CODIF with updated electronics.

Figure 6.1: Comparison between spectra taken by CODIF at calibration at University of Bern in 1994, and current version with updated timing electronics.

As can be seen in Figure 6.1, the spectra distributions are similar between the versions. The location of the mean, and general distribution shapes are nearly identical, with the only major difference being the total number of collected events. With the enhanced timing resolution, we pick up the same plasma profiles as does the previous instrumentation, as expected. The higher timing precision available allows for smaller margins of error in energy.

6.1.2 Time of Flight Progression with Energy

Next part is to observe the response to the same ion over different initial energies for all MCPs and the carbon foil. Time of Flight progression refers to the subsequent changes in the ToF spectra as the initial energy of the ion is varied. As the residual energy of an ion increases, the time it takes to traverse the drift chamber decreases, therefore higher energies shift the temporal spectra to smaller values of time. The changes to initial energy alter the collision cross section available to the ion; residual energy kept by the ion will subsequently change based off these changes to the scattering cross section. Resulting spectra responses per ion over all energies yield curves showing the progression of the spectra with respect to energy, which we call a ToF progression.

In Figure A.1 depicts the ToF progression on a carbon foil for all ions listed in Objective 1. The changes in total energies cause the peak of the spectra to shift to lower times. In addition, more of the plasma successfully emerges from the carbon foil, reducing angular and energy dispersion a small amount. This manifests as a narrower FWHM of the spectra.

6.1.3 Spectra Results and Fits

Figure A.5 depicts the resulting spectra from H_2^+ from the source, comparing MCP aspect ratios of $^L/_D$ 20 to $^L/_D$ 40 as well as the Al_2O_3 coated $^L/_D$ 20, with carbon foil for reference. Depicted are the resulting spectra from H_2^+ from the duoplasmatron source, comparing a coated $^L/_D$ 20 MCP to an uncoated version and a carbon foil for reference. Note that the coated $^L/_D$ 20 MCP spectra includes sputtering effects; the H_2^+ has been more easily broken apart by collisions along the beamline and result in a prominent proton peak at a faster ToF. In addition, heavier elements from the beamline are also sputtered and contribute to the ToF spectra. Sputter from a duoplasmatron source becomes more prominent with the lighter ion species due to the faster velocities the ions contain.

When multiple different ion species overlap like this, we deconvolute them using a double exponential fit. In the case of Gaussian distributed particle populations, Gumbel et al. (1954)

found that the total number of particles detected from the Gaussian sample population contribute to the shape of the exponential[30]. In particular, as the total number of events detected increases, he found that the exponential function approaches a limit, and that limit is the Gumbel function. Restating from earlier sections, the standard Gumbel distribution behaves as

$$F_G\left(x;\mu,\beta\right) = \frac{1}{\beta}e^{-\left(\frac{x-\mu}{\beta}+e^{-(x-\mu)/\beta}\right)} \tag{6.1}$$

To incorporate the sum of two separate Gumbel functions, the fit function took the form of the following:

$$F\left(T\right) = C_0 + A_1 e^{-\left((T-t_0)/t_1+e^{-(T-t_0)/t_2}\right)} + A_2 e^{-\left((T-t_0^{'})/t_1^{'}+e^{-(T-t_0^{'})/t_2^{'}}\right)} \tag{6.2}$$

where the amplitudes of each peak are $A_{1,}\, A_2$ respectively; each peak (global maxima) occurring at t_0, $t_0^{'}$ respectively; rising edges governed by t_1, $t_1^{'}$ respectively; and trailing edge governed by t_2, $t_2^{'}$ respectively; for any point in time T.

6.1.4 Spectra Energy Loss

Ions incur an energy loss on collision, so the residual energy contained by the ion is important for detection. Resulting spectra distributions are skewed Gaussians - therefore, the mean value follows the centroid of the distribution. In a system where the spectra are no longer skewed, the maximum peak would be equal to the centroid. As mentioned previously, the ion travels a 3 cm flight path after passing through the carbon foil or MCP at the entrance to CODIF; from the observed time of flight, the energy of the centroid can be derived using the non-relativistic energy equation, knowing the mass of the monoenergetic plasma beam. This yields the residual energy, or how much energy is retained by a scattered incident particle.

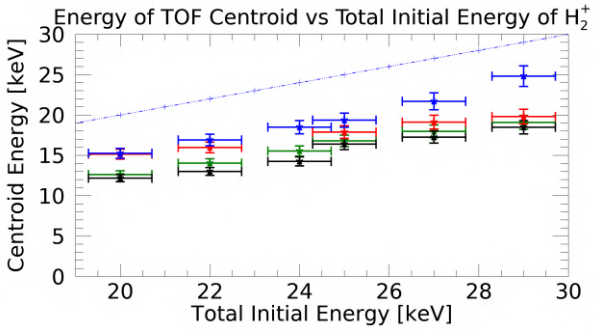

(a) Energy of the observed ToF peak for H_2^+ ions vs. the total ion energy before the collision.

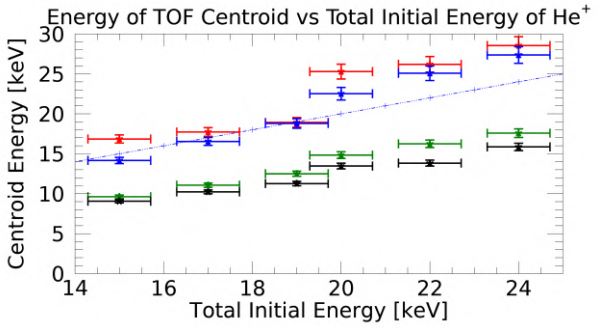

(b) Energy of the observed ToF peak for He^+ ions vs. the total ion energy before the collision.

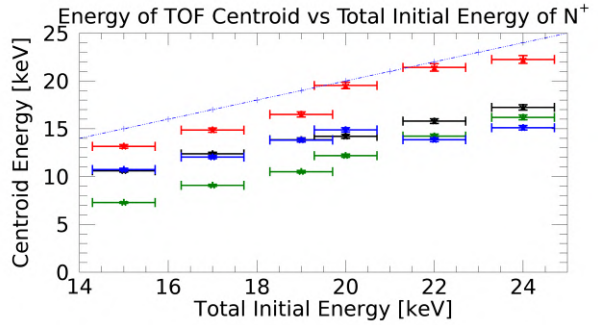

(c) Energy of the observed ToF peak for N^+ ions vs. the total ion energy before the collision.

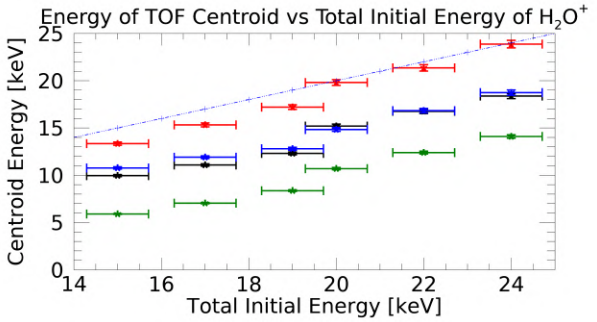

(d) Energy of the observed ToF peak for H_2O^+ ions vs. the total ion energy before the collision.

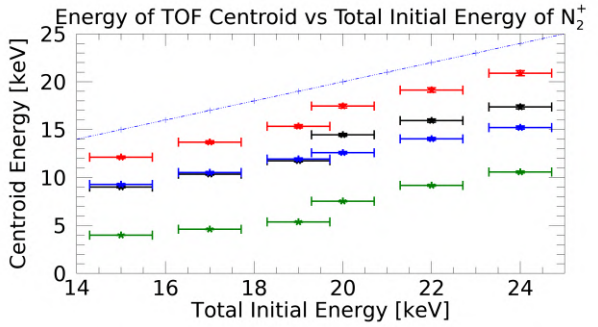

(e) Energy of the observed ToF peak for N_2^+ ions vs. the total ion energy before the collision.

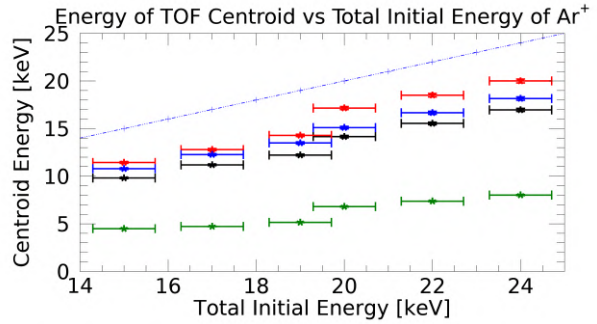

(f) Energy of the observed ToF peak for Ar^+ ions vs. the total ion energy before the collision.

Figure 6.2: Depicted here are the resulting energies of the centroid of the ToF distribution when compared to the carbon foil (green) for an L/D 20 uncoated MCP (black), aluminum oxide coated L/D 20 MCP (blue), and an L/D 40 uncoated MCP (red).

Figure 6.2 shows the observed energy calculated from the centroid of the distribution of each specie of ion. This distribution is a function of the initial total energy imparted from the source and the PAC. The blue dashed line indicates no energy loss into the carbon foil or

MCP. As can be seen, all MCPs retain more energy than the carbon foil except for helium and hydrogen. There is clear separation of each of the surfaces in terms of retained energy, with geometry effects being more pronounced as well as this mass dependent effect on the light ions.

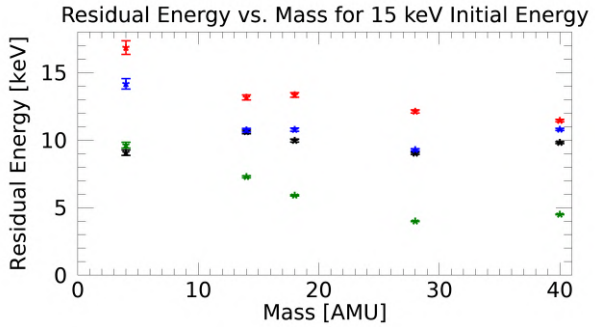

(a) Residual energy after the collision of the observed ToF peak for 15 keV ions vs. the ion mass.

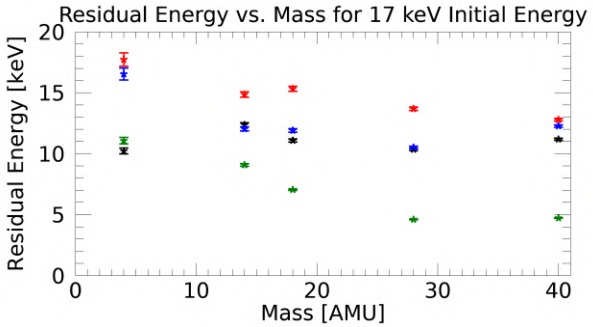

(b) Residual energy after the collision of the observed ToF peak for 17 keV ions vs. the ion mass.

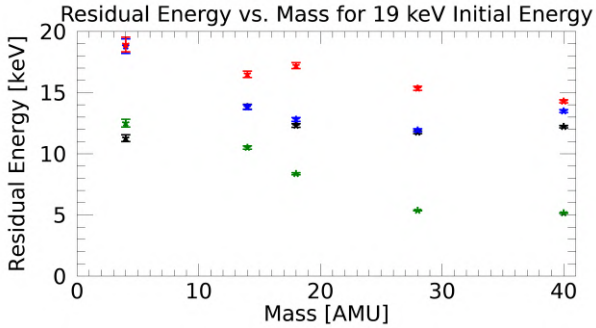

(c) Residual energy after the collision of the observed ToF peak for 19 keV ions vs. the ion mass.

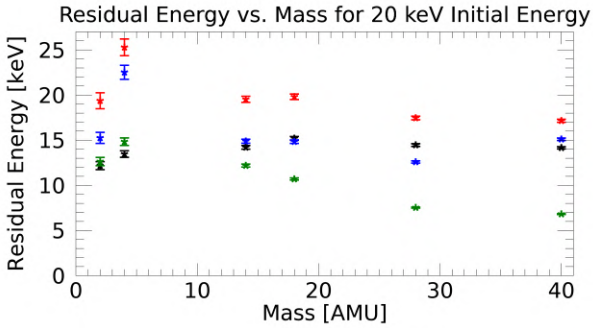

(d) Residual energy after the collision of the observed ToF peak for 20 keV ions vs. the ion mass.

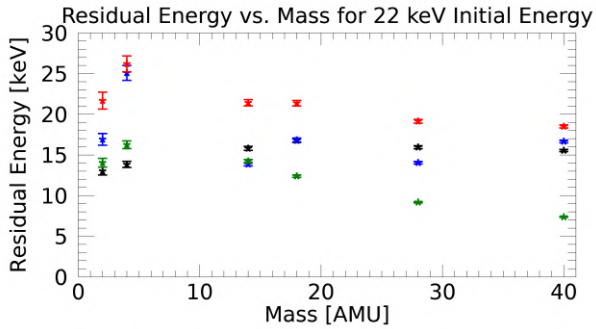

(e) Residual energy after the collision of the observed ToF peak for 22 keV ions vs. the ion mass.

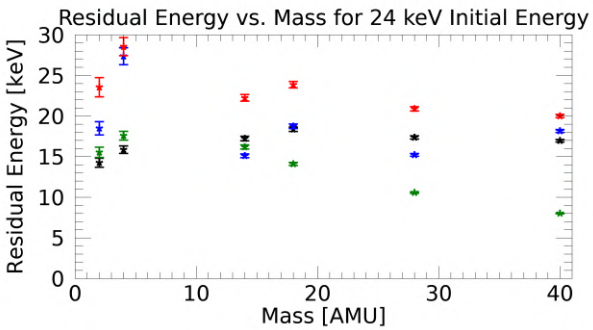

(f) Residual energy after the collision of the observed ToF peak for 24 keV ions vs. the ion mass.

Figure 6.3: Residual energy after collision with the MCPs and carbon foil are plotted as a function of mass above, at the same initial energy.

Therefore, Figure 6.3 compounds each individual ion of each energy range to depict the trends with particle mass. With this, we observe that the energy retention vs. the carbon foil for all MCPs improves as mass increases. In other words, the scattering and energy loss of heavy ions in the carbon foil is far more significant than with any MCP surface. Detailed discussion of the geometry induced trends and those of the coating are left to the respective subsections within Section 6.2.

Overall, for all ions heavier than helium, and at all energies, the FWHM of the plasma spectra is much more resolved. However, the use of the MCP at the entrance also acts as a collimator, limiting the total flux of particles that traverse through the plate, and further diminishing the flux of particles that interact at grazing incidences. The net result of this is the total event rate for a valid pair of signals through a MCP is significantly smaller than that of the carbon foil. In exchange, the timing data of the ions is much improved.

Figure 6.4 depict the trends in mass and in energy for a few selected ions and energies. Included is a linear fit projection on the FWHM vs Total Ion Energy plots. Across the board, the MCPs have a consistent and almost linear response, if not constant. For the FWHM vs. Total Energy, carbon foils improve (decrease) in FWHM linearly as energy increases. This is to be expected following the foil's Stopping Power due to itself being inversely proportional to the energy available.

Furthermore, the previous trends in FWHM are supported by the FWHM vs Mass in Figure 6.5. Carbon foil behaves exponentially with mass due to stopping power, while all MCPs remain relatively constant, or slightly linear. The subsections devoted to geometry and coatings elaborate on this in more detail.

In other words, as the energy available to the ion increases, the resulting FWHM and scattering effects due to the Stopping Power of the carbon foil decrease in a linear relationship. When we extrapolate to the case of FWHM vs. Mass, the relationship changes somewhat. MCPs still perform approx. linearly or a constant value, while the carbon foil steadily increases in an exponential fashion, as predicted in the non-relativistic regime.

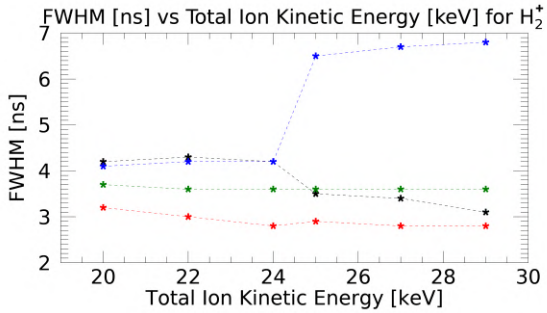

(a) FWHM vs. Total Ion Energy for H_2^+ across all energies.

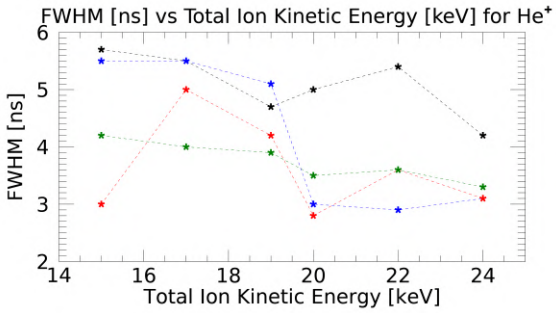

(b) FWHM vs. Total Ion Energy He^+ across all energies.

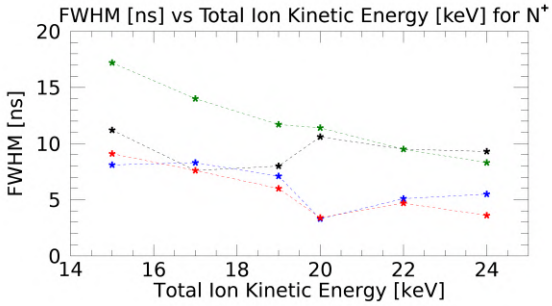

(c) FWHM vs. Total Ion Energy N^+ across all energies.

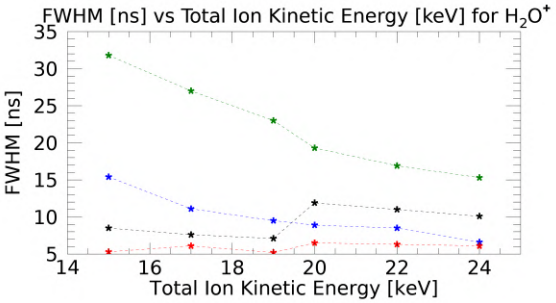

(d) FWHM vs. Total Ion Energy H_2O^+ across all energies.

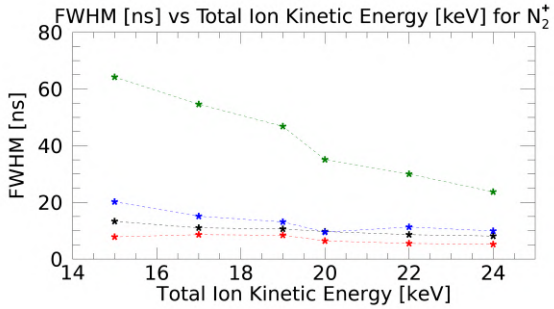

(e) FWHM vs. Total Ion Energy N_2^+ across all energies.

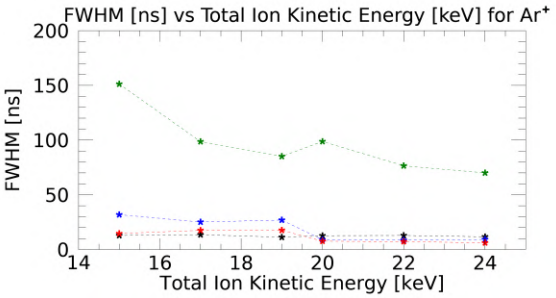

(f) FWHM vs. Total Ion Energy Ar^+ across all energies.

Figure 6.4: FWHM vs. Total Ion Energy for a range of parameters, comparing between an uncoated $^L/_D$ 20 MCP (black), aluminum oxide coated $^L/_D$ 20 MCP (blue), uncoated $^L/_D$ 40 MCP (red), and a traditional carbon foil (green).

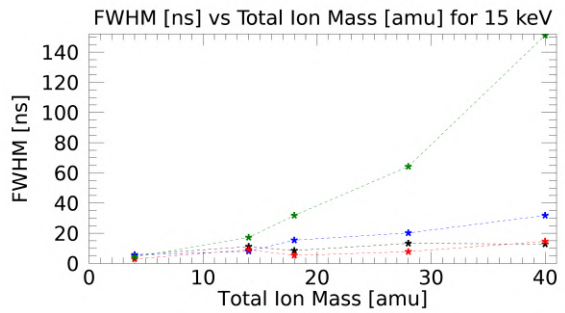

(a) FWHM vs. Mass at 15 keV between all entrance media.

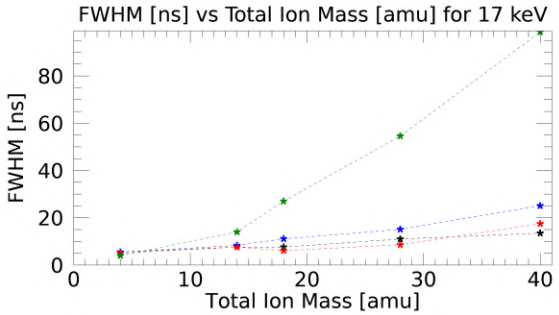

(b) FWHM vs. Mass at 17 keV between all entrance media.

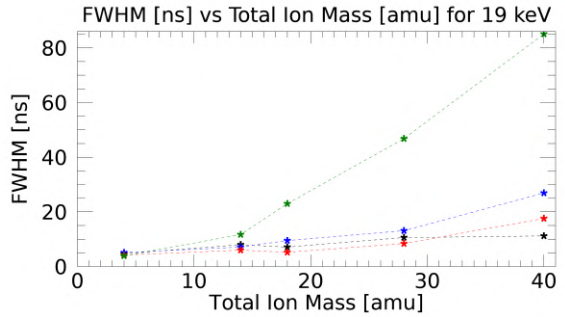

(c) FWHM vs. Mass at 19 keV between all entrance media.

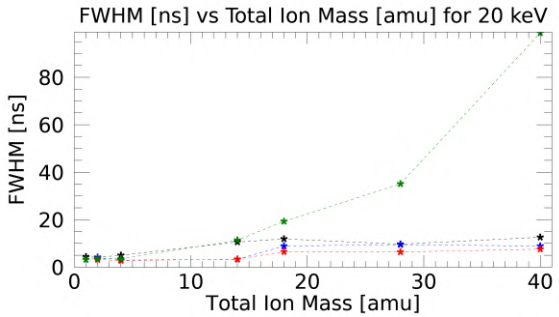

(d) FWHM vs. Mass at 20 keV between all entrance media.

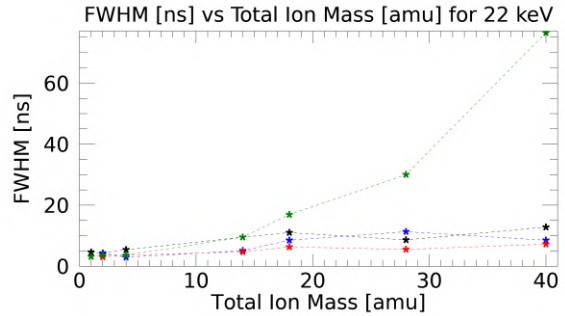

(e) FWHM vs. Mass at 22 keV between all entrance media.

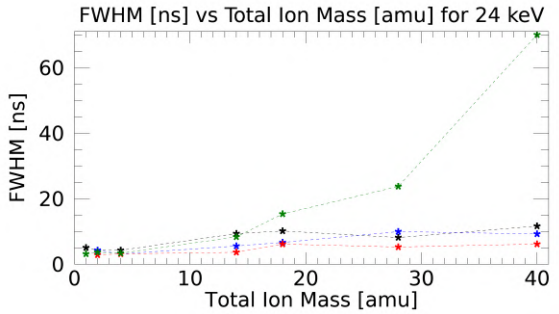

(f) FWHM vs. Mass at 24 keV between all entrance media.

Figure 6.5: FWHM vs. Mass for a range of parameters, comparing between an uncoated $^{L}/_{D}$ 20 MCP (black), aluminum oxide coated $^{L}/_{D}$ 20 MCP (blue), uncoated $^{L}/_{D}$ 40 MCP (red), and a traditional carbon foil (green).

Very Low PAC Range Experiment was done to determine the minimum PAC required for well-defined spectra. CODIF was designed for detection of ions using a carbon foil, and as such engineered for high PAC voltages in the 10 - 30 kV range. Consequently, the minimum turn-on voltage for the unit is about 4 kV, and cannot go lower. As can be seen, the figure shows a stark contrast in spectra for the N_2^+ ion at the same energies at this PAC far below nominal operational values. To compare, the carbon foil spectra for N_2^+ ions traversing is smeared to the point of non-recognition, indistinguishable from background and excluded from this plot. To complicate matters, the different species have different stopping power ranges when impacting a carbon foil, so for example under certain conditions N_2^+ might have a stronger (or weaker) stopping acceleration effect than a nitrogen ion.

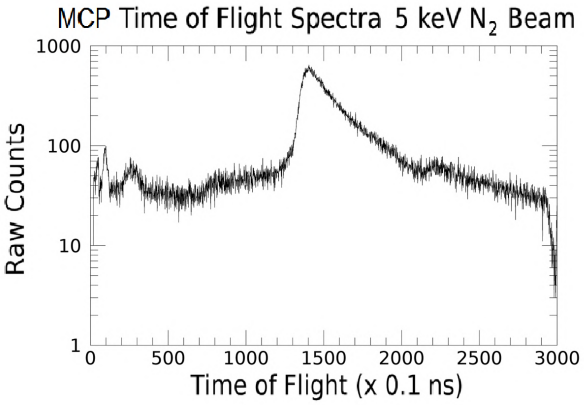

Figure 6.6: Comparison of ToF spectra for 5 keV N_2^+ ions, undergoing ~4 kV post acceleration onto a standard $L/D = 20$ MCP, having collected approx. 200000 separate events.

Potential applied to the MCP at the entrance is governed by a resistive divider chosen such that the voltage drop across the MCP is a known, small value. Interestingly, it was operable even with approx. 85 V drop across the plate, with the spectra observed depicted in Figure 6.6. Gain of the MCP at 85 V is small, and the Atomic Layer Deposition (ALD) predicts a Secondary Electron Yield (SEY) of approx. 1 at that voltage. In other words, each collision of a charged

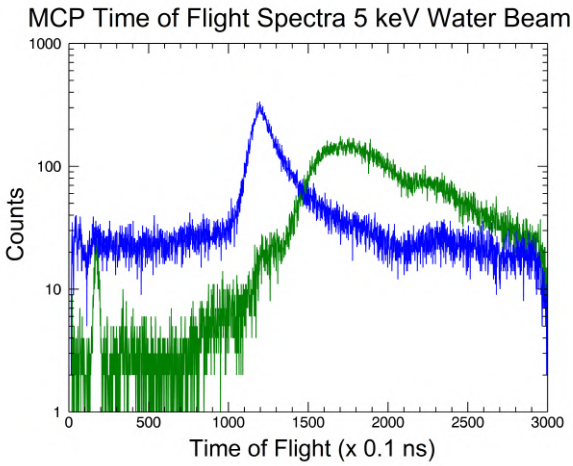

Figure 6.7: Comparison of spectra for 5 keV H_2O^+ ions undergoing ~4 kV post acceleration onto an aluminum oxide coated $L/D = 20$ MCP (blue) and carbon foil (green), approx. 200000 separate events each.

Ion and MCP	Spectra Peak ToF	Spectra FWHM	Start Rate	Stop Rate	Valid Rate	Start Efficiency	Stop Efficiency
5 keV N_2 Uncoated $^L/_D$ 20	140.5 ns	21.3 ns	7997	19408	212	0.01092	0.02651
5 keV N_2 Carbon Foil	N/A	N/A	N/A	N/A	N/A	N/A	N/A
5 keV H_2O Coated $^L/_D$ 20	119.6 ns	15.9 ns	24532	24947	805	0.03227	0.03281
5 keV H_2O Carbon Foil	170.2 ns	84.3 ns	4388	16276	579	0.03557	0.13195

Table 6.1: Plasma beam parameters for the 5 keV N_2^+ and H_2O^+ ions spectra on $^L/_D = 20$ MCP both with and without aluminum oxide coatings.

particle with the MCP will on average liberate 1 electron from the plate, creating a cascade. Additionally, Figure 6.7 contains the spectra of 5 keV water ions onto the aluminum oxide MCP at 4 kV PAC. Due to the coating, the SEY of 1 is achieved at only 35 V applied.

In addition, the MCP system all but eliminates the need for post acceleration, and will work with minimal applied voltage. As can be seen, the only requirement on the MCP is that is have a secondary electron yield of at least 1, to facilitate the knock-off electrons from a grazing incidence collision. Further support arises from testing an $^L/_D = 20$ MCP coated with a 60 Angstrom layer of aluminum oxide against a 5 keV beam of water at minimum PAC. The coating drastically improves the secondary electron yield at all voltages. In particular, the voltage required to achieve around 1 SEY is substantially lowered; in our case approx. 35 V potential is enough.

6.2 MCP Aspect Ratio and Coating Comparison

The upcoming sections detail the observed geometrical and coating induced trends of the spectra, energy, and ion flux against a thin carbon foil as reference. First, all spectra and derived quantities are compared against a carbon foil backdrop in Section 6.2.1. After establishing benchmarks against the carbon foil, Section 6.2.2 compares and contrasts purely geometrical effects by reconciling the uncoated $^{L}/_{D} = 40$ and $^{L}/_{D} = 20$ MCPs. Following that, the same process is repeated, but with the uncoated $^{L}/_{D} = 20$ and aluminum oxide coated $^{L}/_{D} = 20$ MCPs in Section 6.2.3. Finally, a brief summary ends this section.

6.2.1 Comparison to Carbon Foil

The question remains: how differently do particles scatter off the MCP surfaces as the geometry of the pores change? By the direct comparison of the $^{L}/_{D} = 40$ and $^{L}/_{D} = 20$ MCPs with the same coating, effects that are purely geometrical in nature can be measured and compared. In terms of a ToF based mass spectrometer, the most significant factors governing the resolution of the instrument are the following:

- Spectra FWHM
- Energy loss in collisions
- Detection efficiency and deadtime

First in the list is the FWHM of the spectra. Net sum of all scattering within the target influences the resulting spectra FWHM. Particles have a large probability of losing increasing amounts of energy as they undergo multiple scatterings. This spread in the residual energy manifests itself in the FWHM. Coincidentally, as particle velocity decreases, probability of multiple scattering increases.

Figure 6.4 illustrates how the ion response changes per surface as a function of energy. A few properties are immediately noticeable - especially for the heavy ions. Most prominent

is the FWHM gap from carbon foil spectra to all MCPs tested, and is most significant for water ions and heavier. Additionally, the lighter ions, predominantly helium and hydrogen, suggest a trend where eventually there is an energy range where the carbon foil outperforms the MCPs in terms of FWHM. This implies less variance of scattering within the carbon foil than the MCPs where this occurs.

Recall from Section 2.3.1 that the Electronic Stopping Power is proportional to the velocity, and Nuclear Stopping Power dominates at low velocities. However, these light ions travel faster than the threshold where nuclear collisions become significant[6, 70]. Therefore the primary interactions (for light ions) in these materials are energy transfers to the electron cloud of the conduction and valence bands of the target material, as opposed to the elastic and inelastic collisions with atomic nuclei. Similarly, this manifests in the MCP interactions by facilitating kinetic emission of elections as the dominant mechanism.

Furthermore, this increase in FWHM can be explained by the dependence of Electronic Stopping Power cross-section dependence on atomic number of the target. Recall from Section 2.3.1 that

$$S_e = \left[\frac{dE}{dx}\right]_e \sim \left[\frac{N_o}{4\pi\epsilon_o}\left(\frac{Z_i Z_t}{\left(Z_i^{2/3} + Z_t^{2/3}\right)^{3/2}}\right)\right] \cdot v\,(x) \tag{6.3}$$

which depends on both the target number density N_o as well as atomic number Z_t of this target. The lead silicate of the base MCP far surpasses the carbon foil in both quantities when compared. Consequently, the Electronic Stopping Power of the MCP is larger than that for the carbon foil, and ions lose more energy per penetration depth in the MCP than the carbon foil, even though the penetration depths differ. The MCP penetration depth is governed by the angular cross section, whereas the carbon foil penetrates the full thickness of the foil, plus any deviations caused by scattering. Moreover, the MCP is a crystalline compound lattice of many different atoms with different lattice spacing. This adds more variance as well due to the stochastic distribution of target atoms to collide with. Each

different atom in the lattice alters the above stopping power formula. Finally, the net sum of all these individual scattering interactions accumulates into a large variance for light ions onto MCPs, in part due to their high velocity dependence with the Electronic Stopping Power, and partly due to MCP composition and lattice effects.

By a similar notion, the heavier ions exhibit a profound gap in FWHM between MCP and carbon foil. As the Figure 6.4 illustrates, the carbon foil spectra for the heavy ions has much larger spread to it. Due to the increase in mass, the velocities are slower than the light ions and a larger contribution of Nuclear Stopping Power is present. Additionally, the nuclear cross section increases due to the size of the ion, further increasing the nuclear contribution. As the carbon foil particles must traverse a $3.0\,{}^{\mu g}/_{cm^2}$ foil to be detected in the spectra, that leaves a relatively large penetration depth where scattering can occur. The grazing incidence nature of the MCPs severely limit the penetration depth of the ion, so it has much fewer interactions in total for these ions. With much fewer interactions (respectively), the FWHM is kept small. In other words, the longer flight path of the ion through the carbon foil material is much more likely to facilitate multiple scatterings and exhibit Brownian motion of the ion "cannonball" as it collides.

FWHM as a function of energy by individual ion species discussed previously singles out velocity effects, and hints at scattering cross section effects. To look into that and compare the masses, Figure 6.5 compares the FWHM effects at constant energy over the mass range of ions used in this experiment. For all energies the carbon foil starts to deviate immensely from the MCPs around water and heavier. The MCPs all stay relatively similar in FWHM, and do not show a significant trend in mass or energy. That said, the high masses at low energies do deviate more in the MCPs as well. Consequently, the MCPs do not show as drastic a mass dependence as the carbon foil.

Reduction of the FWHM dependence on mass is indicative of diminished nuclear contributions. However, the nuclear size of these ions is no different between the two setups. Therefore, the drastic change originates from the angular scattering cross section difference.

This is a function of both the angle of incidence as well as the target MCP material properties. The combination of these results in much less probability of interaction in the MCP compared to the carbon foil, and manifests itself as a broadening of the FWHM of the carbon foil spectra. Within the carbon foil, the effects of both Electronic and Nuclear Stopping Power are significant, and cause exponential-like increase of FWHM with mass.

In addition to the spread of the spectra is the residual energy retained by the plasma after interacting. Whereas the spread of the spectra is related to the total breadth of cumulative scattering mechanisms, retained ion energy investigates the total transfer of energy from the ion in these conditions. Figure 6.2 shows how the MCPs and carbon foil respond. Notably, the ions heavier than nitrogen all retain more energy in all MCPs than the carbon foil for all energies. For the light ions, there are a few spots where the carbon foil spectra retains more energy than some MCP configurations. However, the percent increase and retention of energy is most significant at the lowest energies and the largest of masses.

Subsequently, the difference in initial energy and residual energy is deposited directly into the respective material. This transfer is a combination of inelastic collisions with the electron cloud of the material (Electronic Stopping Power) and nuclear recoil from collisions (Nuclear Stopping Power) as the atom bounces back from inter-atomic forces. Both these mechanisms contribute to the production of secondary electrons. However, the MCPs are more efficient at this than the carbon foil, with a few outliers outlined above. This is supported by Winter et al. (2007), where the differential cross section of argon ions into an electron cloud was analyzed. Under the kinetic emission regime, the lowest angles of incidence reported the largest differential cross section with minimal energy transfer to the electrons[96]. This means it is much more likely to interact with electrons at lower angles, while transferring minimal energy. Resulting energy redistribution is governed by a host of processes within the target, with more available mechanisms to possibly use with increased energy transfer. Excitons, plasmons, and nuclear recoil all redistribute the imparted energy, but are mediated by this available energy. Consequently, small angular impacts inhibit the loss of energy into

the target by any mechanism except by transfer and liberation of an electron.

6.2.2 Geometrical Effects Comparison

The preceding section dealt with the net differences of all MCPs to the carbon foil. An important question remains: how do purely geometrical changes of the MCP affect the resulting ToF spectra and by extension mass resolution? To this end, only the uncoated MCPs will be compared, with the only difference being the $^{L}/_{D}$ ratio, one $^{L}/_{D}$ 20 and one $^{L}/_{D}$ 40 compared against each other.

From Figure 6.4 we see the trend of each ion species with energy. Barring the outlier from helium ions, the $^{L}/_{D}$ 40 has the smallest FWHM of the MCPs tested, for each ion. There is a modest decrease of the FWHM with respect to energy, as well as a large variance with mass. The $^{L}/_{D}$ 40 ranges from 25% to 50% improvement over the $^{L}/_{D}$ 20, depending on mass.

This is indicative of a minor, if any, dependence of FWHM with energy as well as a clear angular relationship. The $^{L}/_{D}$ ratio restricts the angle of interaction and volume of interaction available, which in turn manifests in the FWHM of the spectra. Increasing the energy at constant mass implies the ions are traveling faster, but the increased velocity plays a marginal role in these interactions.

Similarly, Figure 6.5 depicts the trends with respect to mass for constant energies. Energy does not significantly affect these FWHM as seen by the locations of the MCP's FWHM as the energy increases, but there is a modest increase of FWHM with mass, and modest decrease of FWHM with energy.

The MCPs in general are all grouped together at much lower FWHM at the highest masses. Between the $^{L}/_{D}$ 40 and $^{L}/_{D}$ 20, there is a gap where the $^{L}/_{D}$ 40 has smaller FWHM, which starts after approx. nitrogen. Increasing mass starts to expand this roughly 10% difference up towards 20% for the largest difference. Therefore, these FWHM trends imply the plasma is more uniformly scattered in the $^{L}/_{D}$ 40 than the $^{L}/_{D}$ 20. FWHM is proportional

to the total variance of the sum of scattering processes. With a reduction in FWHM, the ensemble of particles undergoes roughly the same net scattering. Only difference being the geometry, and by extension the critical angle of the MCPs, the shallower critical angle is the cause.

Recall the critical angles for the MCPs are 2.9^o for $^L/_D$ 20 and 1.4^o for $^L/_D$ 40. The more oblique angles of the $^L/_D$ 20 allows for a wider variance due to its factor of two bigger critical angles. Additionally, multiple scattering probabilities are increased within this $^L/_D$ 20. With multiple scattering, the ion risks losing all energy and becoming trapped inside the channels, never making it out in the worst case scenario. Otherwise, multiple scattering causes major deviations in trajectory as well as energy transfer as the ion becomes more sporadic. As a result, the FWHM suffers from this.

From Figure 6.2 we see the trends of residual energy between the different uncoated MCPs. For all masses and energies of ions (except hydrogen) the $^L/_D$ 40 spectra retain more energy than the $^L/_D$ 20. This observes a mass dependence due to the mass dependence of the carbon foil, discussed in the previous section.

MCP induced grazing incidence greatly increases the probability of specular reflection occurring for colliding ions. Specular reflection imparts a marginal amount of energy into the MCP, proportional to $\sim sin^2\left(^\theta/_2\right)$ of the angle of impact from surface parallel (discussed in Section 2.3.1). Maintaining specular reflection for MCPs in grazing incidence configurations is key; the magnitude of the final velocity of the ion must be close (in this case about 90%) to its initial value and is imposed by the geometry. This implies that the velocity component perpendicular to the MCP channel is significant, and the parallel component does not contribute significantly. Due to the $^L/_D$ ratio governing the allowed angles, the perpendicular velocity component is reduced. From Section 2.3.1 we see the energy transfer equation in the center of mass frame. The geometrical changes reduces the available energy transfer by limiting the range of impact angles, which in turn affects the scattering. Therefore, the narrower channels of larger $^L/_D$ ratios diminishes the allowed energy transfer. Consequently

the ion retains a higher percentage of its initial energy, which is observed in the spectra.

6.2.3 Coating Effects Comparison

Sections 6.2.1 and 6.2.2 cover basic MCP comparison to carbon foil, and differences among geometry changes, respectively. Now, the question becomes how the coatings affect these outcomes?

First, this surface affects the scattering FWHM as a function of energy. Comparing the aluminum oxide $^{L}/_{D}$ 20 to the uncoated MCP from Figure 6.4 , there is some variance but trends start to emerge. Coated MCP's FWHM for the light ions (protons and helium) is within approx. 5% of that of the uncoated $^{L}/_{D}$ 20, at least at low energies. A schism forms at the higher energies. For protons, the coating makes it worse by about 60% and for helium is improved by about 40% For the heavier ions, the coated MCP is comparable (within ~10-15 %) but has variance as to performing better or worse. In summary, the uncoated $^{L}/_{D}$ 20 performs better on average in terms of FWHM than the coated one, but there are times when the coating is superior.

Similarly, Figure 6.5 depicts the trends with respect to mass for constant energies. Energy does not significantly affect these FWHM as seen by the locations of the MCP's FWHM as the energy increases, but there is a modest increase of FWHM with mass, and modest decrease of FWHM with energy. However, the schism between coatings of the MCPs becomes apparent. For ions heavier than nitrogen, the uncoated MCP actually fares better in terms of FWHM, by up to 50% at the highest energies.

Consequently, the coating imposes a situation where the ions are able to undergo a broader range of scattering when compared to the uncoated variant. This can be caused by the local microchannel morphology. One morphological constituent is the uniform surface smoothness of the coating. For the uncoated MCP, that would be the smoothness originating from manufacture, compounded with the plasma induced sputtering during operation creating a pitted structure. The coated MCP's surface smoothness relates to how uniform

the atomic layer deposition, such as creating small crystalline islands or outcrops within the pores. These morphological structures adjust the angle of impact to the local geometry, and can inhibit or aid the scattering processes, causing a large variance in observed energy. Next, the atomic layer deposition method of aluminum oxide used in the MCPs produces amorphous aluminum oxide layers. Amorphous alumina has a chaotic structure to it; amorphous alumina has a continuous distribution of bond configurations instead of discrete localizations in the band structure[81]. As a result, both the distribution of nuclei and the associated electron cloud lack organized structure as well. Therefore, scattering can occur at any atom or constituent electron cloud in the continuous distribution sporadically, which in turn increases the FWHM due to the increased amount of possible scattering targets.

In terms of energy lost by the ion, there is a stark difference. Figure 6.2 the measured energy of the centroid of the spectra depicts a marked improvement in retained energy with the additional alumina layer than without, for protons and helium ions. This improvement over the uncoated MCP is roughly 25% for protons and upwards of 50% for helium, and higher energies further separate the two. For the remainder of the ions and energies, the coating conferred a marginal benefit, less than 5% improvement except for argon and high energy nitrogen molecules, which increased to about 10% and decreased by about 10%, respectively.

First, this variance with mass and energy can be explained by a velocity dependence. Heavier ions at the same energy will have a reduced velocity than that of a light ion. From Section 2.3.1, recall the nuclear stopping power is energy dependent, and electronic stopping power scales with velocity. Subsequently, the more massive ions are more apt to undergo nuclear collisions (including elastic, inelastic, and quasi-elastic) than to scatter off the the electron cloud, compared to less heavy ions.

	Spectra Peak ToF	Spectra FWHM	Start Rate	Stop Rate	Valid Rate	Start Efficiency	Stop Efficiency
6 keV N_2 coated $^{L}/_{D}$ 40	100.7 ns	6.1 ns	7188	75232	246	0.003270	0.03422

Table 6.2: Plasma beam parameters for the 6 keV N_2^+ ions spectra onto a 60 Å Al_2O_3 coated $^{L}/_{D} = 20$ MCP.

Next, surface smoothness is another contributor. Atomic layer deposition methods provide a controlled growth environment for thin films of variable thicknesses as desired. Tamboli et al. (2011) studied the effects of atomic layer deposition using thin films of MgO. They found the vapor deposition method used produces very smooth and uniform surfaces using an atomic force microscope. Additionally, the smoother the surface, the higher SEY obtained[85]. With a smoother surface, the energy transfer from the ion to the surface is reduced, seen in Figure 6.2. It is significantly reduced for the light ions hydrogen and helium, which are the most susceptible to scattering due to their small mass.

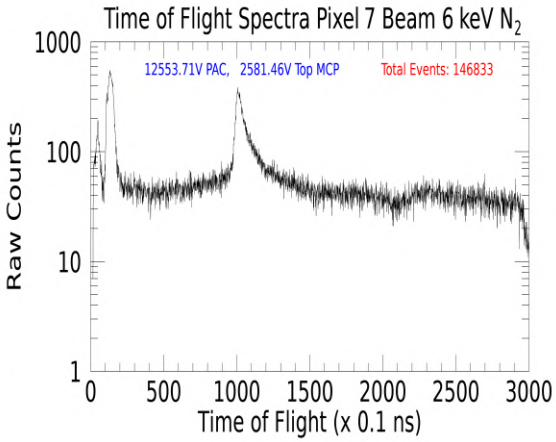

Figure 6.8: Raw ToF spectra of 6 keV N_2^+ onto a 60 Å Al_2O_3 coated $^{L}/_{D}$ 40 MCP.

Therefore, the combination of both an $^{L}/_{D}$ 40 and a coating of aluminum oxide would have an even larger SEY due to the interplay of both the geometry and coating effects. This is the case, however the SEY is so large it becomes a detriment. Seen in Figure 6.8 is the only spectra that could be obtained with this MCP. Huge flux of Starts and Stops with minimal Valid events leads to a very large noise floor that is very difficult to optimize for plasma detection.

6.2.4 Summary

Clearly, all types of MCPs vastly out-perform the traditional 3.0 $\frac{\mu g}{cm^2}$ carbon foil. Additionally, the aspect ratio $^L/_D = 40$ has a marginally reduced FWHM when compared to the $^L/_D = 20$. Reductions in FWHM are indicative of a plasma distribution that undergo relatively uniform scattering collisions, or in other terms, the distribution is more temporally coherent. Directly responsible for this difference are the distinct properties that differ between the MCP plates, namely the $^L/_D$ aspect ratio. Higher aspect ratios incorporate smaller pore diameters compared to the length of the pores, constraining the geometry as shown in 6.9.

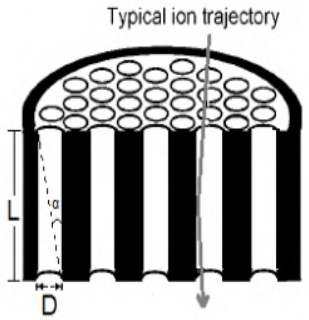

Figure 6.9: Basic MCP geometry. For a particle to not interact with the walls of the pores, its angular trajectory must be less than $\tan^{-1}\left(\frac{1}{2(^L/_D)}\right)$ from normal to the pore centers.

With straight channels (no bias angle) the angle given by the arctangent of the $^L/_D$ ratio $\alpha = \tan^{-1}\left(\frac{1}{^L/_D}\right)$ is the maximum angle of a particle to not interact with the MCP, with the particle on a trajectory from the edge of a pore to opposite edge, which is 1.4^o and 2.9^o for the $^L/_D = 40$ and $^L/_D = 20$ respectively. Since the particle distribution exiting the ESA and impinging upon the MCPs are similar, the scattering of ions (and subsequent FWHM spread) are confined to the direct changes in geometry between the different plates. This geometry confines the angles for particles to undergo specular or grazing incidence collisions, where the particle is assumed to have only one interaction with the MCP walls before continuing onward. As stated earlier, the $^L/_D$ ratios impose the angular limit, and the $^L/_D = 20$ accepts angles of incidence of approx. twice that of the $^L/_D = 40$.

Thin film coatings also reduce energy losses in the collisions by making the surfaces smooth via ALD. This is most evident by the light ions of hydrogen and helium. The SEM images from Figure 4.1 also shows the how smooth the surface of the coated MCP is. With a decent SEY from the coating itself, the combined effect with the smooth surface ensures

minimal energy transfer, especially for light ions. The heavier ions did not improve as much, but still beneficial over the uncoated. Consequently, this is due to the mass of the projectile ion, with lighter ions inherently more easily scattered in the collisions.

6.3 Ion Detection Efficiency Comparison

Observed flux rates of all signals varied with the media impinged upon. One particular metric to compare ToF performance are the signal efficiencies. Specifically, we are interested in the Start and Stop efficiencies of the MCP and carbon foil. With these, we define the Valid events as the total number of events that have a corresponding Start and a Stop within 300 ns of one another. These Valid events are compared against the total number of Stops and Starts for the Start efficiency and Stop efficiency, respectively.

By the definition of these ratios, some significant detection flux data can be obtained. With the Start efficiency (defined as $\eta_{Start} = {}^{Valids}/_{Stops}$) we compare those ions with both a Start and a Stop compared to all ions that at least produced a Start signal. By inference, we can get the number of ions lost, and cannot produce a Stop signal, and how they respond with energy. Similarly, the Stop efficiency (defined as $\eta_{Stop} = {}^{Valids}/_{Starts}$) we compare those ions with both a Start and a Stop compared to all ions that at least produced a Stop signal. Furthermore, the ions "missing" a Start can be inferred.

Experimentally determined Start and Stop efficiencies are plotted for all the ion species and energy ranges observed in Figures 6.11 and 6.12.

6.3.1 Carbon Foil

For all ions, the ratio of ${}^{Valids}/_{Starts}$increases with initial energy for the carbon foil. This has to do with the scattering cross section, as well as the respective stopping powers of the carbon foil. Recall in Equation 2.17 the electronic stopping power, which is the ensemble averaged energy transfer dE to the electron cloud via inelastic collisions per path length dx. It also observes a velocity dependence. Consequently, the energy increase will cause a

modest increase in the electronic stopping power. Additionally, the (scaled) nuclear stopping power component, in Equation 2.18 increases with mass, as well as a higher probability of small angular deflections from the cross section[53, 52]. As a result, the nuclear component of stopping power is insignificant for the fast, light ions and is more influential on massive, slow ions.

Net effects of both the stopping powers at higher projectile energies means the impinging particles will lose more energy on average, which shows up in the energy plots in Figure 6.2. If you take argon for example, at initial energy 15 keV, we measure just about 5 keV, for approx. 10 keV loss, but at 24 keV initial energy, we measure an energy of about 8 keV, for a much larger loss of 16 keV. However, the increased initial energy does increase the depth of penetration for these ions. By extension, increasing the energy increases the probability of the particles penetrating further into the carbon foil. Therefore, since the thickness of the foil is constant, the increased energy makes it much more likely for the ion to successfully navigate the full thickness of the foil and emerge out the other side. Consequently, the flux of ions that go on to produce a Stop signal are increased as well (which also makes for more frequent Valids). Seen in the figure is that the Valid frequency is increasing faster than that of the Start frequency culminating in a net result of increasing Start efficiency with energy for the carbon foil.

Similarly arguments can be made for the Stop efficiencies. However, there are a few important differences. Nitrogen actually decreases with energy, and water is relatively constant with energy, with the remainders slightly increasing with energy. For the carbon foil, this is almost identical to the Start efficiency. More energy allows more particles to produce a Stop by improving the chances to traverse the thickness of the foil, improving Valids as well. The difference arises in nitrogen most profoundly, where the Valid frequency is increasing slower than that of the Stop frequency culminating in a net result of decreasing Start efficiency with energy for the carbon foil. For water, the rates of increase are about proportional or slightly increasing. All the other ions follow the same trend as the Start efficiencies.

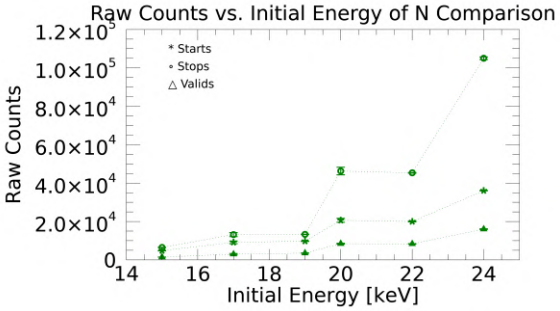

(a) Minute-average rates for Start, Stop, and Valid events of N^+ on carbon foil as a function of total initial energy.

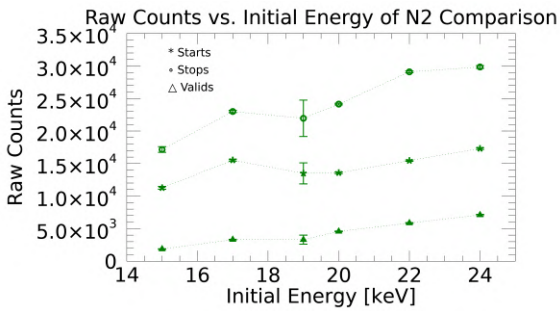

(b) Minute-average rates for Start, Stop, and Valid events of N_2^+ on carbon foil as a function of total initial energy.

Figure 6.10: Comparison of minute-average rates for an outlier N^+ and N_2^+ as representative of the generally observed trend of the other elements.

Therefore, the number of Stops being detected increases with energy faster than the Starts that also produce a Stop, for water and nitrogen. Illustrating the point is Figure 6.10. These differences are compounded from many different mechanisms and just as many sources. First, the carbon foils used are from the same set fabricated for the engineering model of CODIF; these carbon foils have been in-use since manufacture, and some of the foils show signs of wear. At this point in time, the foils exhibit some minor tears and holes. These allow for particles to travel through, creating a Stop signal without interacting with the foil. This will follow a probability distribution based on the foil, but with gaps present, increasing the energy will allow more particles to go through the foil and not change the number of particles already flowing through the gaps. However, the Starts will increase more slowly due to reduced area of the conversion surface. Therefore, the Start efficiency will droop, but this is heavily dependent on ion optics, or the spatial focusing of the plasma.

Knocking off electrons from the foil is dependent on the transfer of energy from the ion (or recoiling carbon foil atoms) to the electron cloud. Sufficient energy must be imparted to the electron to excite it to the point where it can break the surface potential barrier, and escape. For nitrogen and water to an extent, this means energy transfers from the ion to the electron cloud are less likely to liberate an electron. This is due to the size of the nucleus; more massive ions partition the energy among the nucleons, leading to a reduced energy per

nucleon. Reduced energy of the nucleons will impart less energy to the electrons of the target during collisions, leading to a large fraction of low energy secondary electrons[74]. Secondary electrons still need to cross the surface potential barrier of the carbon foil to be emitted, and picked up by the electron multiplier. Less secondaries are able to cross this barrier with decreased initial energy[74]. The increase in initial energy drastically improves the chances for heavy ions to traverse the foil and produce a Stop. Now, the heaviest ions of Ar^+ and N_2^+ have such a low probability of getting through the foil that the Stop efficiency still increases with energy. Nitrogen and water to an extent are just large enough to noticeably inhibit Start electron production, but still small enough that they are likely to emerge and continue to make a Stop. Consequently, these ions observe a near constant to downward trend with Stop efficiency with energy.

6.3.2 MCP Geometry

Both MCPs constrain throughput ions by their respective surface geometries. Seen in Figures 6.11 and 6.12, the Start efficiencies of the $^L/_D$ 20 and $^L/_D$ 40 uncoated both are very small, hovering around a few percent. The $^L/_D$ 20 is above the $^L/_D$ 40, with the exception of a handful of outliers. There is also a very minor upward trend with energy for all masses. Subsequently, the increased energy does not significantly affect the emission of electrons.

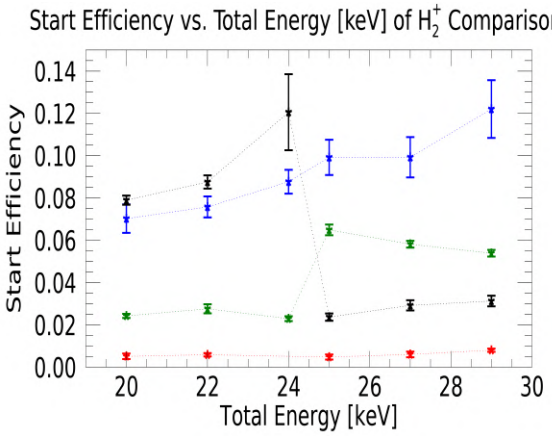

(a) Start efficiency of H_2^+ vs. total ion kinetic energy.

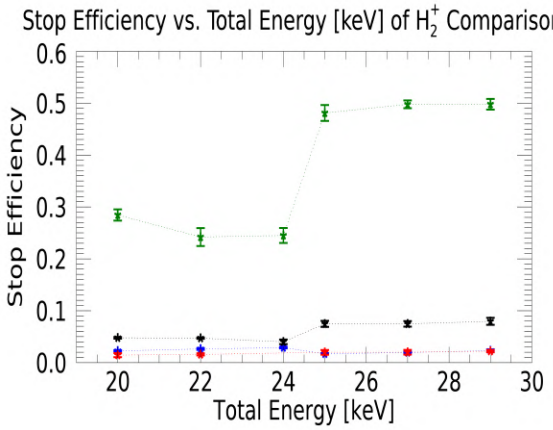

(b) Stop efficiency of H_2^+ vs. total ion kinetic energy.

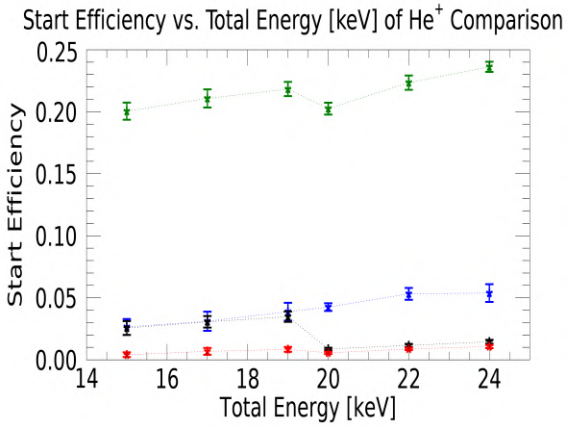

(c) Start efficiency of He^+ vs. total ion kinetic energy.

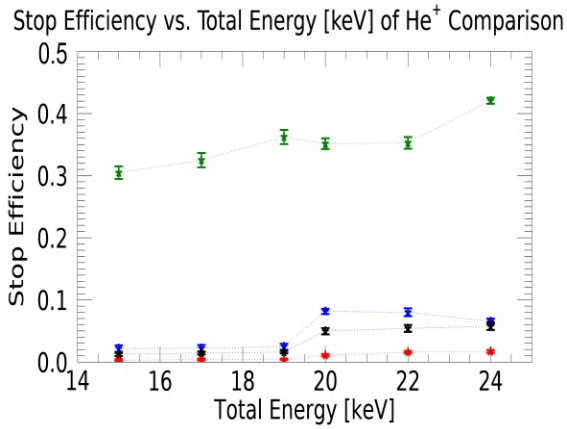

(d) Stop efficiency of He^+ vs. total ion kinetic energy.

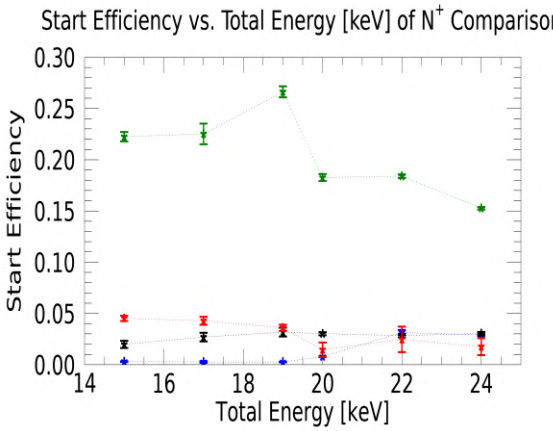

(e) Start efficiency of N^+ vs. total ion kinetic energy.

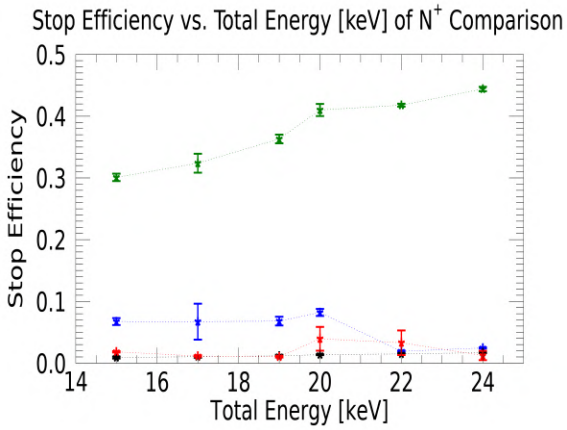

(f) Stop efficiency of N^+ vs. total ion kinetic energy.

Figure 6.11: Start and Stop efficiency of the less massive ions when compared to the carbon foil (green) for an $^L/_D$ 20 uncoated MCP (black), aluminum oxide coated $^L/_D$ 20 MCP (blue), and an $^L/_D$ 40 uncoated MCP (red).

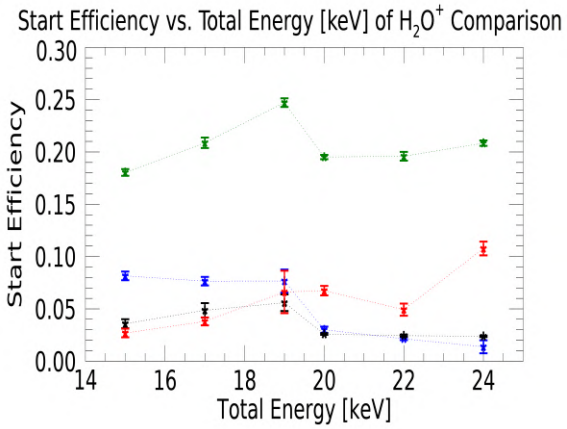

(a) Start efficiency of H_2O^+ vs. total ion kinetic energy.

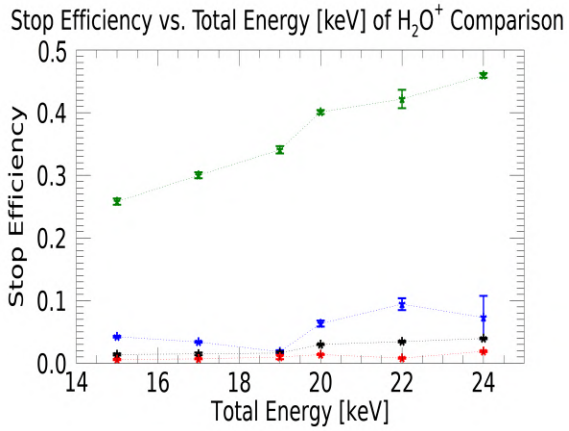

(b) Stop efficiency of H_2O^+ vs. total ion kinetic energy.

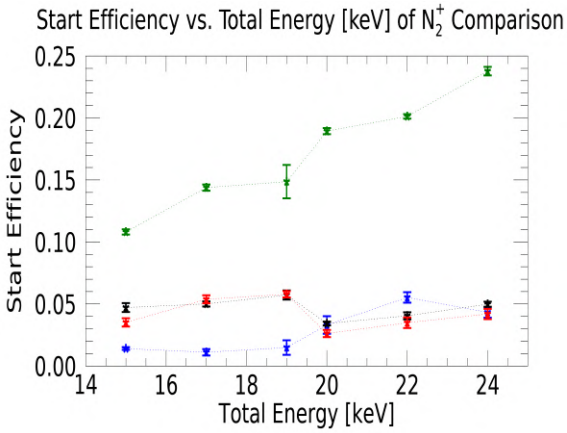

(c) Start efficiency of N_2^+ vs. total ion kinetic energy.

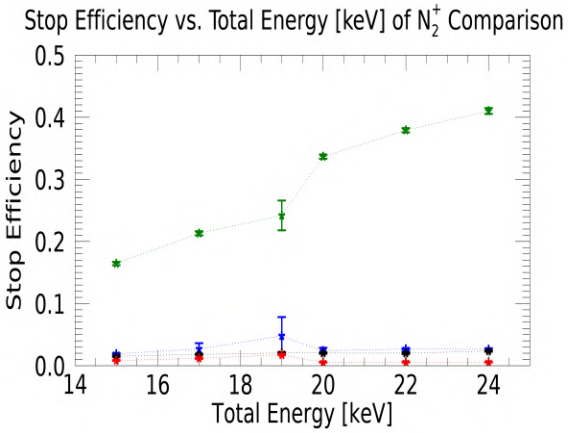

(d) Stop efficiency of N_2^+ vs. total ion kinetic energy.

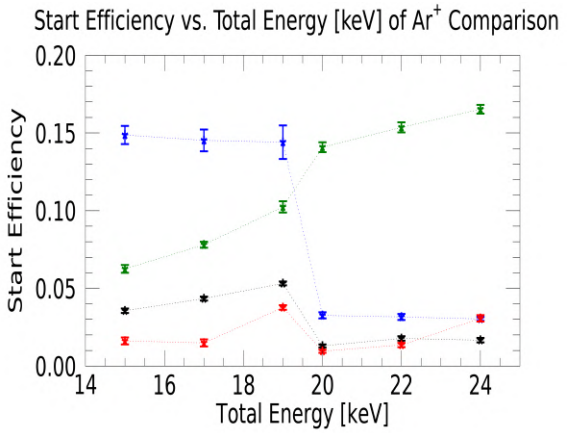

(e) Start efficiency of Ar^+ vs. total ion kinetic energy.

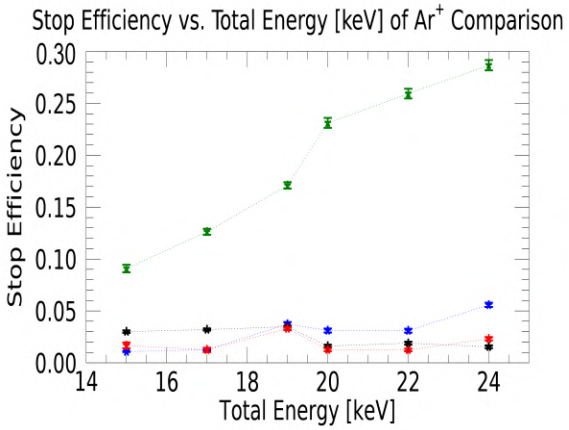

(f) Stop efficiency of Ar^+ vs. total ion kinetic energy.

Figure 6.12: Start and Stop efficiency of the heavy ions when compared to the carbon foil (green) for an $^L/_D$ 20 uncoated MCP (black), aluminum oxide coated $^L/_D$ 20 MCP (blue), and an $^L/_D$ 40 uncoated MCP (red).

Mentioned previously, MCP geometries affect the allowed angles of incidence for the particles. Furthermore, from the studies of Wang et al. (2018 and Bruining et al. (2016), the volume of the MCP material it can interact with [91, 8]. Within this volume of interaction, secondary electrons can only be detected if they escape the surface to vacuum. Depending on where inside this volume of interaction a secondary electron is formed, it must then diffuse to the surface following a probability distribution $P(x) = P(0)\, e^{-x/L}$ with diffusion length L[83, 26, 6]. Therefore, this defines the effective depth to which secondary electrons can form and be emitted. Shallower angles of incidence effectively decrease the time the ion spends within this "escape zone" as well as reduce the penetration depth of the ion. This is evidenced by Sternglass et al. (1957) which expresses the SEY as $\gamma(\theta) = \gamma_0 sec(\theta)$, which is a function of incident angle[83]. This can also be seen in the works of Lennard et al. (1986) in their angular dependence of argon's electronic stopping power[48]. Furthermore, MCPs exhibit a gain dependence on the L/D ratio[88, 39]. Recall Figure 2.9 depicts the trends observed by Ivanov et al.

Consequently, the purely geometric component also governs the yield of secondary electrons streaming off the surface of the MCP. One would think an increase of secondary electrons for the Start signal to improve the Start efficiencies. However, this is not the case. As can be seen, there is a roughly constant offset of the L/D 20 to the L/D 40 MCP's Start efficiencies for all ions, with the L/D 20 performing better. Given the larger SEY for the L/D 40, more electrons per incident projectile are liberated. This daisy chains on each secondary electron collision, producing an end result of very large charge pulses. Due to the resulting stream of secondaries and their distribution, multiple Starts are detected per singular incident ion, leading to false Starts. Additionally, the larger SEY (and subsequently larger gain) allow for more electron cascades to be detected. Finally, this manifests as a distinct drop in efficiency due to the increased gain. Furthermore, this efficiency can be reduced if ions are implanted in the MCP, or observe multiple separate collisions with the MCP channels, leading to no associated Stop signal while still generating a Start.

Stop efficiency is different still. While also comparatively low compared to carbon foils for the heavier ions and similar to Start efficiency, there are more sporadic variations. Stop efficiencies are similar between the L/D ratios, but the L/D 20 has slightly higher Stop efficiency more often than the L/D 40. Minus the variations, there is a very slight upward trend with energy as well. These outliers are low energy argon, high energy water, low energy helium, and hydrogen. Water and hydrogen mark the worst offending outliers, which are most likely due to ion source optics.

These Stop efficiencies will be low in general due to the grazing incidence model, coupled with these straight channel MCPs. The bulk of the plasma exiting the ESA will be close to parallel with the MCP channel axis. With straight MCPs which have $> 60\%$ open area, only a very small fraction of the initial flux will interact and produce a Start signal. Meanwhile, the flux of ions that is transmitted will create a Stop signal. As can be seen, it is on average marginally easier to get a Start with an associated Stop with the L/D 20 than the L/D 40.

Start efficiencies being so close to each other suggests the production mechanism of the Start signals are similar. Start efficiency focuses on the ratio of events that produce a Stop, meaning it filters out the possible implantation of ions in the MCP. Therefore, for every ion that produces a Stop, there are approximately the same percentage of Valids (and by extension, Starts) between the L/D ratios, barring the outliers. These outliers mark the cases where implantation in the MCPs as well as multiple scattering effects hinder the signals. For example, due to the light masses of hydrogen and helium, multiple scattering is more likely to occur in the L/D 40 as well as implantation, reducing the number of Valids accordingly.

6.3.3 MCP Coating

Similar to the previous section, the coated L/D 20 has superior Start efficiency to the uncoated L/D 20 for all ions. Both exhibit a very slight upward trend in energy, as the increase ever so slightly improves the probability to sputter off an electron from inside the MCPs. Even so, the improvement over the uncoated MCP is marginal, with nitrogen and water ions being

the most pronounced.

The coating of alumina with the same geometry is correlated with a slightly higher, constant increase in both Start and Stop efficiency. Therefore, the flux of Valid events is a larger fraction of the Starts with the coating than for the uncoated MCP. Furthermore, to achieve this increase, that means a bigger percentage of the plasma that produced a Start goes on to to produce a Stop, and thereby a Valid event. This requirement implies a larger fraction of the plasma undergoes specular reflection with the coating; or in other words, less particles are multiply scattered or implanted with the coating present.

More of the plasma observing specular reflection is partly due to the coating process itself. The process of ALD coating of these materials produces a very uniform, smooth layer on top of the substrate. ALD allows for controlled thin film growth. Thin films prepared this way are very uniform, and its density can also be controlled to an extent. All of these mechanisms culminate in a very smooth surface for the ions to specularly reflect off of, which in turn also increases the SEY[85]. The combination of these increases both respective efficiencies in CODIF, more so for the light ions than heavier ions. Light ions are more apt to be heavily scattered due to their light masses during the momentum exchange on collisions, which is alleviated by the smooth coatings.

6.3.4 Summary

There are a few mechanisms occurring all at once for ion detection efficiencies. For the carbon foil, both the Start and Stop efficiencies increase with energy for all ions, with the exception of nitrogen and water. All of these effects are from the energy per nucleon transfer from the ion to the carbon foil, as well as the total experienced stopping power. Increase in mass reduces the energy per nucleon, leading to secondary electrons without enough energy to cross the surface potential barrier of the carbon foil. Meanwhile, the additional mass likewise inhibits the transmission of the ion through the foil, leading to an efficiency increase for the light and heavy ions, but the intermediate ions are much more likely to be transmitted,

so the Start efficiency decreases.

For the MCP geometry, the resulting stream of secondaries and their distributions allow multiple Starts observed, leading to false Starts. Furthermore, the larger SEY (and subsequently larger gain) allow for more electron cascades to be detected. Finally, this manifests as a distinct drop in efficiency due to the increased gain. Furthermore, this efficiency can be reduced if ions are implanted in the MCP, or observe multiple separate collisions with the MCP channels, leading to no associated Stop signal while still generating a Start. Angles of incidence effectively alter the time the ion spends within the material as well as change the penetration depth of the ion.

For the MCP coatings, the flux of Valid events is a larger proportion of the Starts than for the uncoated MCP, due to a relative increase in specular reflection. ALD techniques ensure a smooth and very uniform thin film for these ions to scatter off of. Specular reflections off smooth surfaces like this reduce the energy deposited into the material, and increase the SEY. For the $^{L}/_{D}$ 20 coated MCP, this improved the efficiencies, but the $^{L}/_{D}$ 40 was for the most part unable to produce a spectra, due to how large the SEY was, causing so many non-Valid events that the noise floor swamps the system.

6.4 Angular Dependence

Hinted at from the ESA simulation results with SIMION in Section 5.2 and the SRIM/TRIM simulation angular response in Section 5.4, there should be a noticeable dependence of the incident plasma with angular trajectory, with respect to the MCP surface. Targets tested include one MCP without a coating and $^{L}/_{D}$ ratio 20 as well as a $60\mathring{A}\, Al_2O_3$ layer coating on a MCP with $^{L}/_{D}$ 20. A monoenergetic beam of $5 \pm 0.1\, keV\, N_2^+$illuminated the straight-channel MCP in question for three increasing PAC voltages, $V_{PAC} \in \{10, 12, 14\}\ kV$.

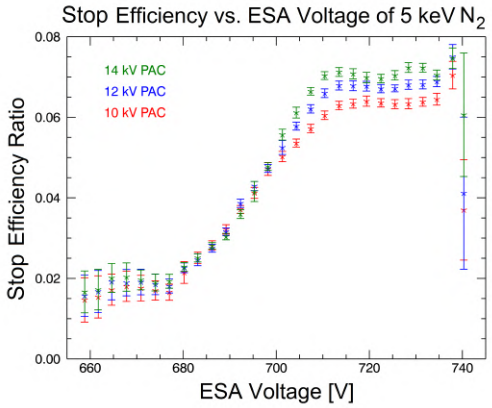

(a) Uncoated $^{L}/_{D}$ 20 angular response.

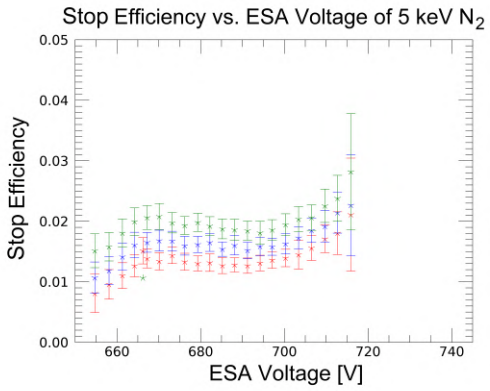

(b) Aluminum oxide coated $^{L}/_{D}$ 20 MCP angular response.

Figure 6.13: Angular response of MCPs with $^{L}/_{D}$ 20, with and without an aluminum oxide film. As the ESA voltage changes, so does the trajectory of exiting ions.

Depicted in Figure 6.13 are the responses in Stop efficiency seen by CODIF while using a specific MCP as the ESA potential is changed. Due to the ESA and PAC affecting angular trajectories of ions, there is a clear trend on the uncoated MCP. The angle caused by the ESA potential impacts the observed Stop efficiencies. Highest ESA settings for the plasma (more radially inward trajectories) are much more efficient than at the lowest ESA settings, by about a factor of three.

Applied ESA voltage governs the trajectory for the ion within, and exits at a certain angle dependent on the position and energy the particle had at the entrance. As the ESA potential is adjusted to higher voltages, the range of ions it accepts shifts to higher initial energies. For a monoenergetic beam, this manifests as a change in deflection; larger ESA potentials at the same ion energy causes the same ions to be deflected inwards radially, and the converse is also true. The magnitude of the PAC also works to "straighten"

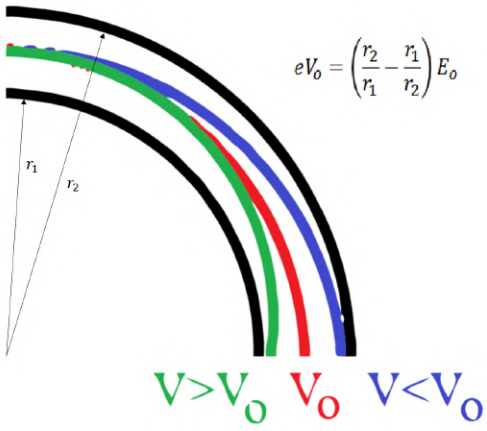

Figure 6.14: Trajectories of an ion through a spherical or top-hat Electrostatic Analyzer for kinetic energies greater (green), less than (blue), or equal to (red) the selected energy range.

the final flight paths since the PAC is comparable, if not greater than, the ion's initial energy. As a result, the iteration through ESA and PAC potentials deflects the plasma beam at different angles by the time the ion impacts the MCP. Then, the ion experiences an acceleration due to PAC towards the MCP. Acceleration subsequently experienced alters the final trajectory more towards normal to the MCP face.

Depicted in Figure 6.14 are the trajectories of some charged particles in the presence of an Electrostatic Analyzer with applied voltage. Based on the initial kinetic energy E_o of the charged particle, the potential required to deflect these particles along the center follows the formula

$$eV_o = \left(\frac{r_2}{r_1} - \frac{r_1}{r_2}\right) E_o \tag{6.4}$$

where r_1, r_2 are the inner and outer radii, respectively, of the ESA apparatus (assuming spherical symmetry)[24]. Therefore, an energy "bandwidth" is selectively transmitted based on the physical dimensions and the applied potential of the ESA. Those charged particles with higher energies than the mean energy selected by the parameters (or lower ESA voltage than the particle's mean energy) will be deflected less, following the blue trajectory in Figure 6.14. Inversely, ions with lower energies than the ESA's selective potential allows (or greater ESA voltage than the particle's mean energy) will have a greater deflection, following the green trajectory in Figure 6.14. All of these trajectories are circular; therefore changes in ESA voltage change the radius of curvature of these trajectories with the kinetic energy of the ion beam held constant. Consequently, the angular component of the ion can be controlled as it leaves the ESA by varying the voltage applied.

For CODIF, the ESA was constructed such that Equation 6.4 reduces to $eV_o = 0.13E_o$ and has a particular energy discrimination of $\Delta E/E \approx 0.16$ [73]. In addition, each sector has a geometric factor associated for the high resolution and low resolution sides. For the geometric factor, recall that $G_{ESA} = \Delta E/E \cdot A \cdot \Delta\Theta \cdot \Delta\Phi$ where A is the aperture area, $\Delta\Theta$ is the acceptance in azimuthal angle, and $\Delta\Phi$ is the acceptance in polar angle . For CODIF, it was constructed such that the high resolution side has $G_{ESA} = 2.16 \times 10^{-3}\, cm^2 \cdot sr$ and the

low resolution side has $G_{ESA} = 2.3 \times 10^{-5}\, cm^2 \cdot sr$, with each sector being 22.5^o in azimuth and 8^o in polar acceptance angles, respectively [73].

6.5 Error Analysis

6.5.1 Duoplasmatron Variance and Counting Statistics

Counting statistics dominates the observations from CODIF. The combined ESA and choice of MCPs/carbon foils in the ToF drift chamber suitably change the total geometric factor. Included is the response to energies and masses. Subsequently, only a fraction of the total ion flux is observed as a result. CODIF observes individual samples of this ensemble of particles, which originate at the duoplasmatron source with a Gaussian distribution profile. As each measurement does not affect subsequent (or prior) measurements, they follow a Poisson counting statistics scheme.

Standard error induced from Poisson statistics behaves as $\sigma = \sqrt{N}$ with the number of samples N. Subsequently, the statistical variations are reduced with larger sample sizes, provided the duoplasmatron source plasma remains in a steady state. Duoplasmatron extraction voltage actually varies a small margin, ranging $E \pm 500\ eV$ induced from the frequently changing parameters required to create a stable beam of plasma from argon impact ionization. Similar variation of the PAC voltage $U_{PAC} \pm 500\ V$ leads to a margin of error in the initial energy of the plasma. Therefore, the total plasma energy variation upon first collision has an energy error margin of $\sigma_T = \pm 707\, eV$.

Additionally, some of the helium ion spectra show residual energies after collision above the initial energy supplied, such as Figure 6.2. This is due to the effects of background noise manifesting within the centroid calculations. Background noise has two main sources, as either crosstalk from one signal line to another (e.g. Starts inducing a Stop via capacitive coupling), or as sporadic and randomly coincident thermal emissions from the MCP. Crosstalk produces a low ToF pedestal in the ToF spectra with significant count rates. The sporadic emissions accumulate and produce a nearly constant, uniform floor across all times.

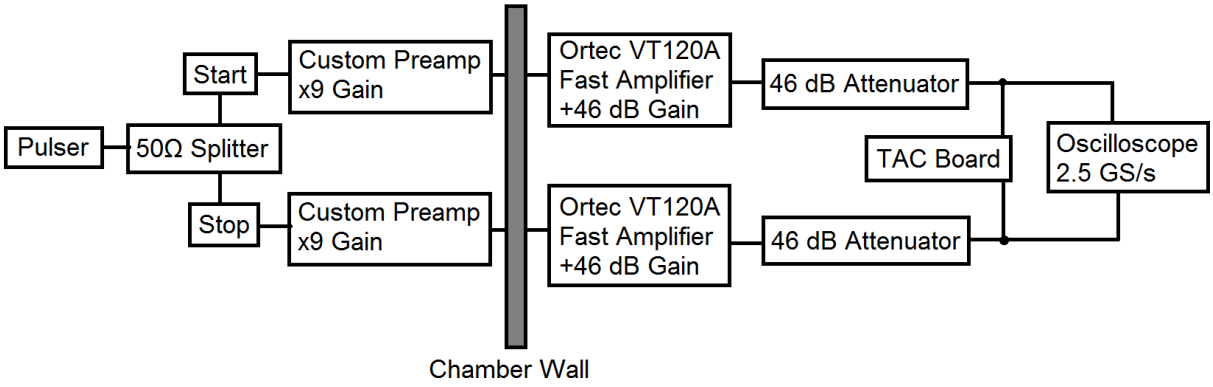

Figure 6.15: Setup diagram for the cable delay testing for CODIF. The oscilloscope measures the delay between the inputs of Start and Stop as the TAC board observes it.

The combination of both these effects lead to a minor skew towards the lower times of flight and consequently inflate the energy of the ion after collision. Predominantly, this becomes significant for light ions such as helium, where the flight times are already small and correspond to high energies.

6.5.2 Temporal Resolution

The prototype electronics used in calculating ToF are resolved and calibrated to 100 picoseconds per bit. As a result, the major impacting factor affecting ToF resolution arises from the induced signal delay from the mismatched lengths of coaxial cable between the detector output and the timing electronics. Cable-induced delays are measured via the setup in Figure 6.15. A pulsing signal is generated by a source with appropriate signal profile for a MCP pulse, subsequently split and injected into both the Start and Stop signal lines. Electronics and oscilloscope then output a time profile for the delayed pulsed.

These signals have equal and minimal added delays from the split of the signal, so only the cable's delay is measured. Since the signals originate at the same time for both signal lines (via splitter) the resulting time difference between the pulses is purely due to the extra time required for the signal to propagate over the mismatched lengths of cable. This cable delay is measured by a 2.5 GS/s oscilloscope and a sample distribution of pulses were

collected. The resulting cable delay is subtly different between the different configurations of CODIF because of differences in installations between the versions. The calculated standard deviation in the delay timing due to cable length is subsequently $\sigma_t = \pm 0.5\, ns$. Therefore, the derived error in the resulting energy is

$$\frac{\sigma_E}{E} = 2\,\frac{\sigma_t}{t} \tag{6.5}$$

As can be seen in Equation 6.5 is that the error in energy is proportional to the fraction of the timing error to the ensemble averaged peak in time. Therefore lighter ions, which travel faster than more massive particles, have a greater fraction in Equation 6.5 and have a larger variance in energy detected. In addition, this error is added in quadrature to the inherent error of the duoplasmatron source.

7 Concluding Remarks

7.1 Conclusions

Observed with CODIF over the full range of ions and energies, we found that:

- $^{L}/_{D}$ 40 preserves more initial energy than $^{L}/_{D}$ 20 (improved energy resolution) with the same coating arising from geometrical differences
- MCP response is heavily dependent on impinging angle, and comes at the cost of severely decreased ion throughput flux for the narrower pore sizes (larger $^{L}/_{D}$ ratios)
- Coatings produced via ALD results in smooth surfaces that increase the probabilities of specular reflection occurring
- At grazing angles the MCP coating improves energy resolution and angular dispersion is approximately the same as uncoated
- MCP coating vastly improves the light ion spectra, with marginal improvement to heavy ions

Therefore, as seen in Figure 6.4, the reduced angular range improves the FWHM, at the cost of the flux of particles that successfully traverse the MCP. This can be caused by a variety of situations. First, a shallower angle of incidence imparts less energy into the MCP from the ion. The MCP receives less energy to initiate an electron cascade for a Start signal, while the ion retains most of its initial energy. Retaining a larger portion of the ion's energy results in the reduced spreading in energy (and subsequently, time) in the ToF spectra. However, that also means the MCP must be able to initiate an electron cascade that is detectable, and is dependent on many external factors. Without significant energy to launch an appreciable cascade, the signal will not be detected and appear in the data as a reduced flux rate for the Start signal.

Additionally, the flight path for the ion is assumed to be linear and normal to the MCP plates; any deviations in angle to normal will cause some ions to "straggle" and take longer than average due to its trajectory. This shows up in the long, exponential decay "tail" in the ToF spectra, and increase the FWHM. Therefore, due to the smaller acceptance range of the $^{L}/_{D} = 40$, the angular spread is also smaller than the $^{L}/_{D} = 20$ MCP, which works to reduce the FWHM and keep the ions relatively well correlated at the expense of ion flux. Interestingly, the carbon foil starts to become the most resolved spectra for light ions on the higher range of energies.

The coating of aluminum oxide creates a very smooth surface for the plasma to scatter off of. Therefore more specular reflections of ions will occur, and by extension less energy is deposited into the MCPs. Material properties of the thin films also improve the base SEY, which will improve signal detection flux rates caused by the secondary electron cascades. Provided the system does not have too much gain, this is a major improvement over the carbon foil. When there is too much SEY, the MCP becomes swamped with junk data, and spectra become very difficult to obtain, like the coated $^{L}/_{D}$ 40 MCP exhibited.

7.2 Future Work

7.2.1 Research Potential

MCP gain is highly sensitive to the applied voltage across the MCP assembly, so care was taken to ensure in our tests that this voltage was the same between the different sets of MCPs. However, we were limited by spacial concerns to using the internal high voltage distribution board, and as such the applied voltage was dependent on the PAC. One further refining experiment would be to see if the applied MCP voltage alone directly influences the ToF spectra and/or detection efficiencies. Since we tied the voltage to the PAC, applying more potential changes both the initial energy of the plasma seen by the MCP, and the gain of the MCP.

The straight channel MCPs used are also subject to the same common issues concerning

their use. First is the implantation (and subsequent re-ionization) of ions inside the MCP channel, contributing to the "Ion Feedback" effect. In addition, the huge combined surface area of these pores allow for a significant absorption of water vapor. Combined, there is the constant concern of implanting plasma beam particles into the walls of the MCP channels at a grazing angle. These adsorbed particles can be ionized again by electron cascades under normal operation. However, the newly liberated ion travels to the entrance face of the MCP instead of the exit, and causes another electron cascade associated with this spurious event. These would be directly proportional to the gain of the MCP, and as such are predicted to increase in frequency of occurrence as the applied MCP voltage increases. In addition, the MCP was operated at low applied voltages ($<$400 V) and not tested at values closer to MCP saturation, around 800-1000 V. The effects of saturation were not tested due to the lack of control over the applied MCP voltage, but are expected to increase the spurious ion feedback. We suspect that under saturation, the exiting electron cascade will have an increased energy, and as such conflict with the current steering electrodes designed for the low energy electrons emitted from a carbon foil. A very small but effectively constant fraction of the plasma will collide at grazing incidence with the MCP resulting in kinetic ionization, but the potential ionization rate is expected to increase at these voltages. It is uncertain what will be the result if the dominant emission mechanism was through potential ionization inside the MCP.

During the experiments, we found a stark angular dependence on the ions by adjusting the voltage range on the ESA, which in turn governs the trajectory of the exiting ions. Each MCP had a region where the efficiency of the Start signals reached a maximum and then decays. Evidently, there is an angle dependent on the work function of the MCP material and $^{L}/_{D}$ ratio where production of secondary electrons is maximized, but this is different for various dopant coatings, and $^{L}/_{D}$ ratios. Further examination of this angular effect is beyond the capabilities of the copy of CODIF used in this study, but would be worthwhile in future instrument studies.

7.2.2 Applications Towards Detector Designs

Depicted in Figure 7.1 is an example hybrid ToF instrument that can benefit from the grazing incidence scattering employed by straight channel MCPs. The whole unit would be physically similar to other ToF mass spectrometers: a spherical or top-hat style ESA leading to a cylindrically symmetric ToF drift chamber, followed by an anode. Drift path length can be adjusted as needed to suit the resolution required without adding too much mass. If a high fidelity measurement of mass is required, it might be beneficial to increase the ToF distance from about 3 cm of CODIF to around 5-8 cm for added distinction.

The instrument is also split into a high sensitivity and a low sensitivity side. These sensitivity regions differ in geometric factor of ions exiting the ESA. In other words, the ESA imposes a reduction in the geometric factor of the transmitted ions onto the low sensitivity side to accommodate a large dynamic range of fluxes. The low side, depending on application, is designed to reduce the geometric factor by a factor between about 100-10000 as needed.

Each junction is illustrated in Sub-figures 7.1b-7.1d. Sub-figures 7.1c-7.1d are similar to other heritage detectors like CODIF and FAST. A Chevron configuration of MCPs with uniform gain ensure a very high detection efficiency for particles arriving at the exit of the drift chamber, picked up by the charge deposition onto the anode. The anode is segmented similar to the heritage missions as well, in 22.5^o segments and spatial resolution governed by spacecraft pin rate. Higher spacecraft spin can increase the spatial resolution if needed due to the increased input acceptance rate of the electronics. Secondaries from the Start signals are directed towards the inner radius of the structure.

The major difference is from the drift chamber entrance, in Sub-figure 7.1b. Each sensitivity sector is split into a thin carbon foil array quadrant and a MCP quadrant. Carbon foils allow for clearer detection of light ion energy and mass. Additionally, carbon foils are more probable to produce a ToF spectra; MCPs using grazing incidence transmit the vast majority of impinging flux without interacting with the MCP. The MCP quadrant is there for mass separation. To aid the reduced geometric factor, ions that exit the ESA and illu-

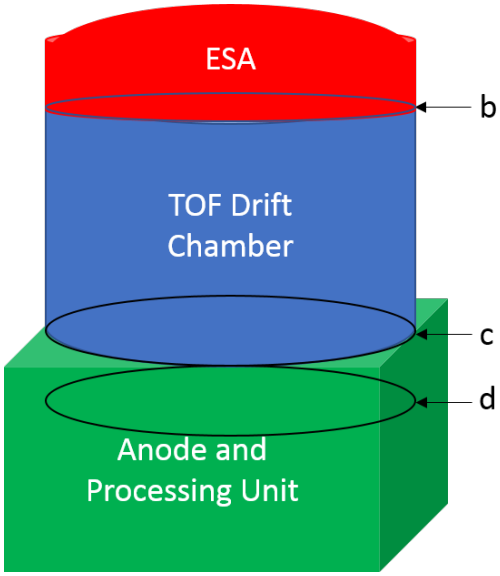

(a) Depicted is a potential setup for a hybrid application of a ToF mass spectrometer. The height of the drift chamber can vary a few cm, depending on the required resolution. Each major junction of the instrument is labeled and shown in the respective sub-figure.

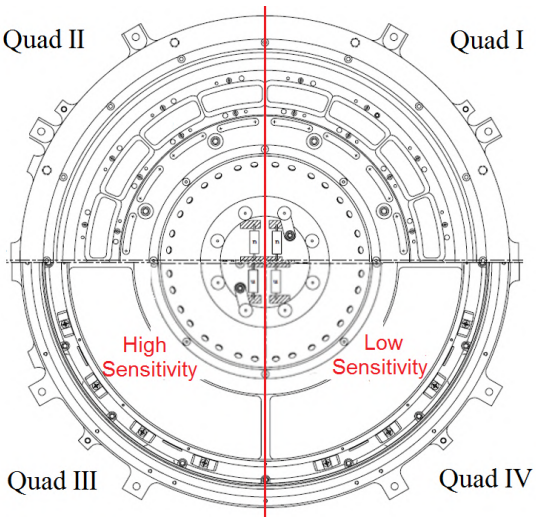

(b) Potential hybrid application for the ToF entrance. The cylindrical canister is split into two sections that differ in geometric factor (from the ESA) by a factor of $\sim 100 - 10000$ to accommodate both large and small fluxes. One quadrant per section is thin carbon foil, and the other is a MCP chosen for the ions in question.

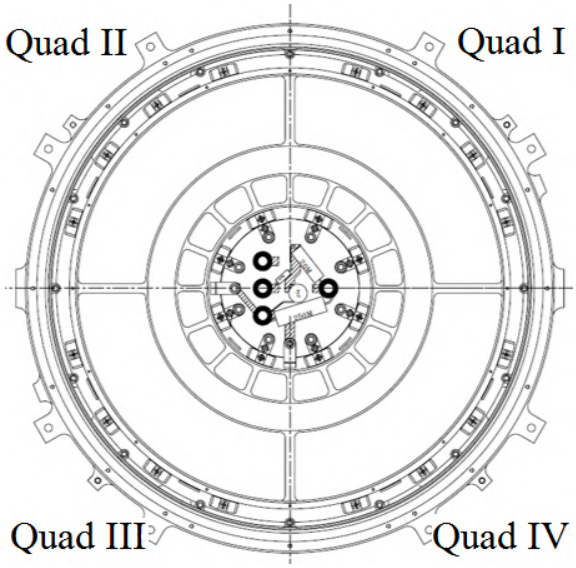

(c) Potential hybrid application for the ToF drift chamber exit. Each quadrant is populated by electrically similar MCPs in Chevron configuration, to provide a uniform amplification and detection efficiency for each ion.

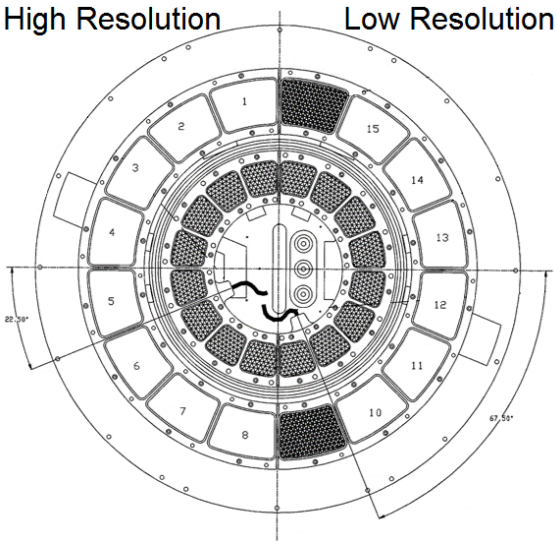

(d) Potential hybrid application of the anode. Each anode is 22.5^o wide for the same angular resolution as CODIF at launch. Start secondary electrons are deposited onto the inner ring of electrodes, and the ion initiated cascades along the outer ring. The low sensitivity side is separated from the high sensitivity side by an empty pixel on each side, to avoid crossover events from the high side.

Figure 7.1: Example layout of a hybrid prototype of a ToF mass spectrometer, utilizing the grazing incidence onto MCPs. Adapted from CODIF mechanical drawings, UNH.

minate the MCPs pass through a collimator aligned with the angle of grazing incidence to be used. The small flux rate that does produce a spectra will have increased probability of interaction this way. Additionally, plasma ions will retain much more energy information, and clean up otherwise overlapping spectra.

In the scheme of high voltage requirements, the MCP sections do not have to apply a PAC to get a signal, while the carbon foils do. If the mission can operate with a full MCP complement, then the power supply can be reduced accordingly without the PAC requirement. Otherwise, it will still be on the order of previous heritage missions that were flown.

Choices of aspect ratio and coating to use are pliable, and depend on the intended application. Higher aspect ratios reduce the energy deposited into the MCP at the cost of the creation of Start secondary electrons. Coatings can be used to combat the decrease in emitted electrons as well. Under current NASA solicitations and upcoming missions, a few combinations of parameters can currently meet the criteria. First, uncoated $^{L}/_{D} = 20$ provide a good balance of detection rate and energy resolution. If further separation of mass is needed, then aluminum oxide layer on top of $^{L}/_{D} = 40$ or even $^{L}/_{D} = 60$ would significantly improve resolution. This layer is preferred due to the large drop in secondary electron emission due to the angular effects of the MCP, and should help alleviate this by increasing electronic gain. Increasing the drift length as well will improve separation of ions close in mass.

Appendices

A Time of Flight Spectra

A.1 Time of Flight Progression

This portion of the Appendix investigates the spectral trends of ions as the total kinetic energy is varied, hereby referred to as the ToF progression. All these following plots are normalized over the total count rate observed to eliminate the effects of statistical error of differing sample sizes. Figures A.1-A.4 depict these ToF progressions for H_2^+, He^+, N^+, H_2O^+, N_2^+, and Ar^+ over the entire energy range of the experiment.

Energy ranges include 15, 17, 19, 20, 22, 24 keV total energy for all ions, except H_2^+ due to difficulty of production in the ion source, and instead are measured over the range 20, 22, 24, 25, 27, 29 keV total energy.

Notice that for each of the ion species and for all MCPs, increased total energy is correlated with both a shift of the spectra to lower time of flight, and a subtle decrease in the FWHM of the spectra. The increase in energy allows the ion to transfer a smaller fraction of its energy to the colliding target due to stopping powers experienced. Additionally, the more energy retained is manifested as a faster velocity in the drift chamber of CODIF, so the ToF observed is faster than at lower energies, causing the shift.

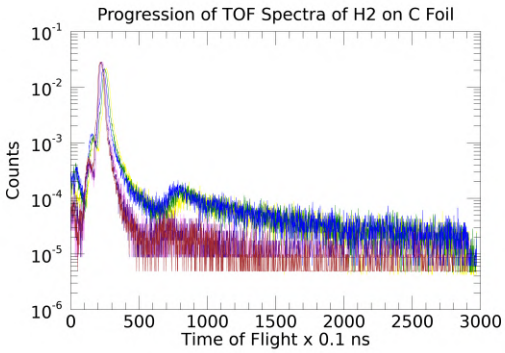

(a) H_2^+ ToF progression on carbon foil.

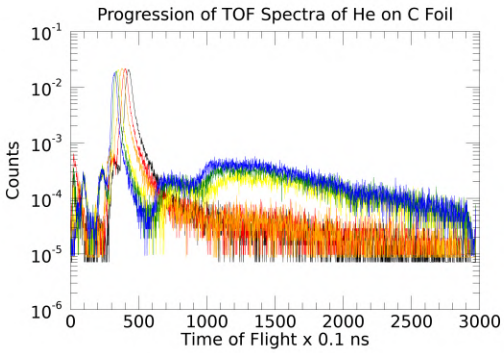

(b) He^+ ToF progression on carbon foil.

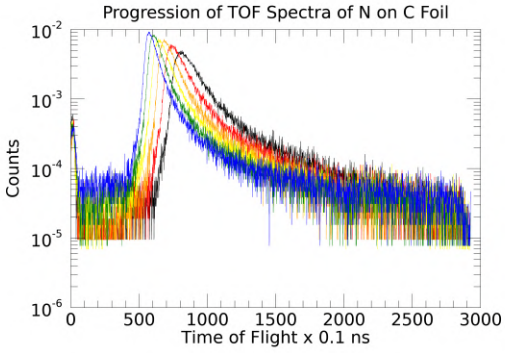

(c) N^+ ToF progression on carbon foil.

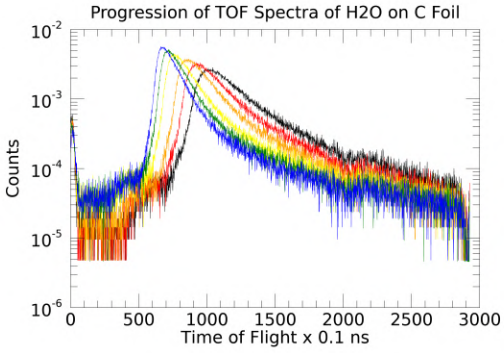

(d) H_2O^+ ToF progression on carbon foil.

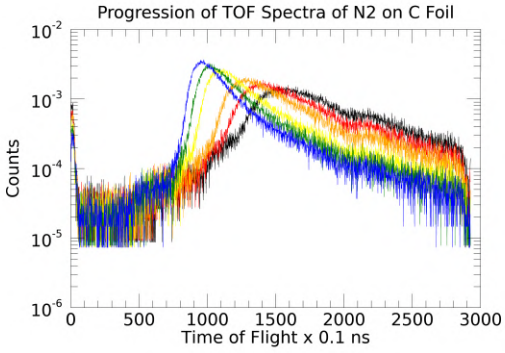

(e) N_2^+ ToF progression on carbon foil.

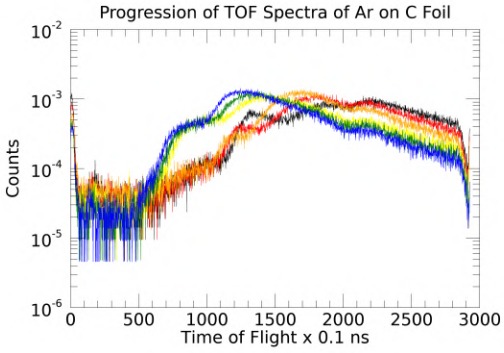

(f) Ar^+ ToF progression on carbon foil.

Figure A.1: Time of Flight progression due to total energy available to the ion, for various species. Energies included are 15 keV (black), 17 keV (red), 19 keV (orange), 20 keV (yellow), 22 keV (green), 24 keV (blue), 25 keV (violet), 27 keV (indigo), 29 keV (brown). Note only H_2^+ and protons range from 20 - 29 keV in energy, and all the others range from 15 - 24 keV.

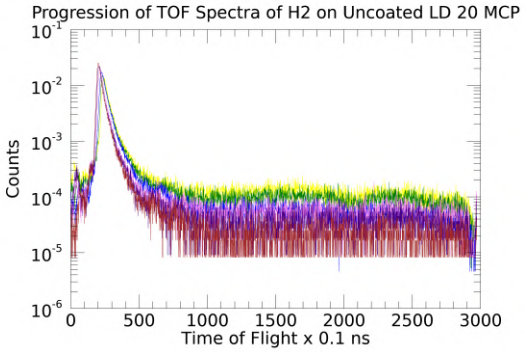

(a) H_2^+ ToF progression on uncoated $^L/_D$ 20 MCP.

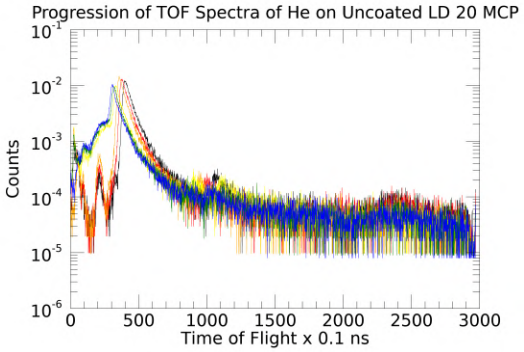

(b) He^+ ToF progression on uncoated $^L/_D$ 20 MCP.

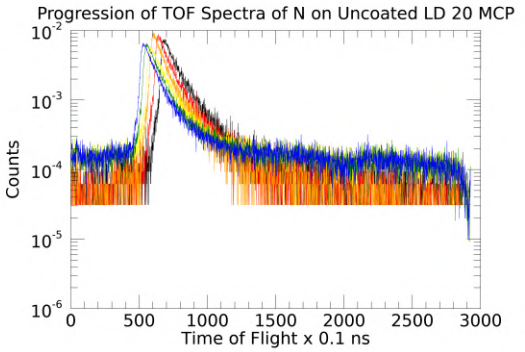

(c) N^+ ToF progression on uncoated $^L/_D$ 20 MCP.

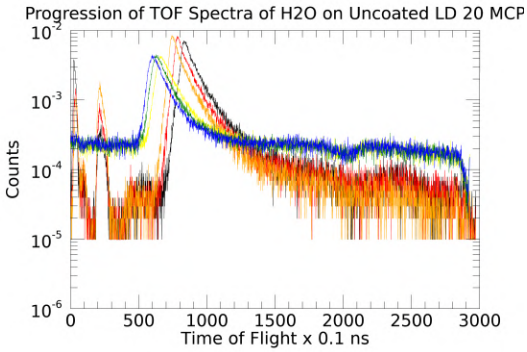

(d) H_2O^+ ToF progression on uncoated $^L/_D$ 20 MCP.

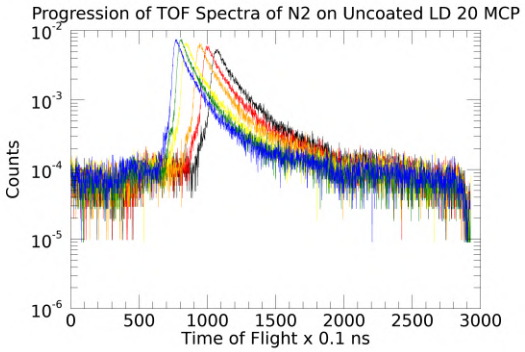

(e) N_2^+ ToF progression on uncoated $^L/_D$ 20 MCP.

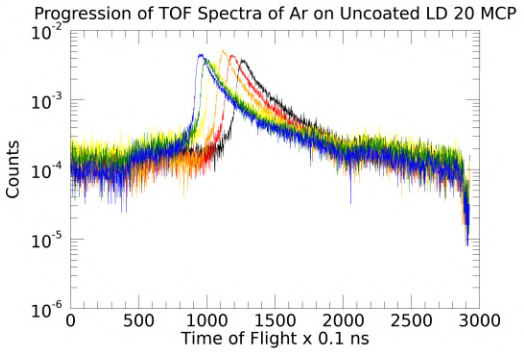

(f) Ar^+ ToF progression on uncoated $^L/_D$ 20 MCP.

Figure A.2: Time of Flight progression on uncoated $^L/_D$ 20 MCP due to total energy available to the ion, for various species. Energies included are 15 keV (black), 17 keV (red), 19 keV (orange), 20 keV (yellow), 22 keV (green), 24 keV (blue), 25 keV (violet), 27 keV (indigo), 29 keV (brown). Note only H_2^+ and protons range from 20 - 29 keV in energy, and all the others range from 15 - 24 keV.

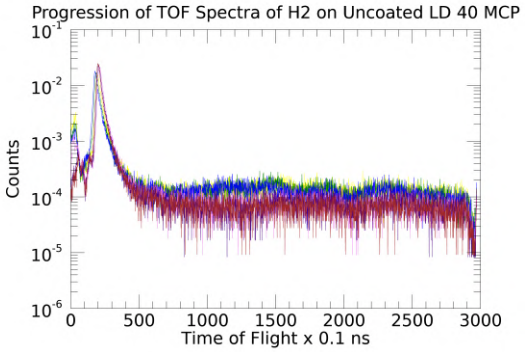

(a) H_2^+ ToF progression on uncoated L/D 40 MCP.

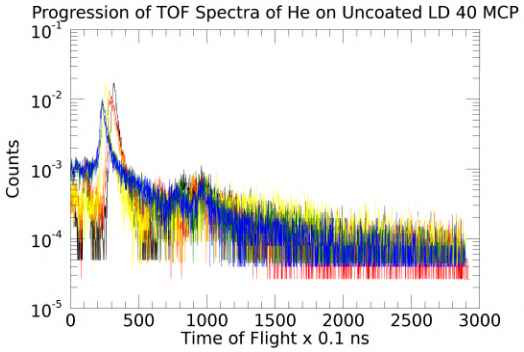

(b) He^+ ToF progression on uncoated L/D 40 MCP.

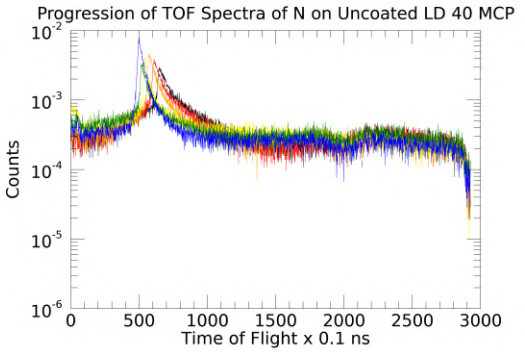

(c) N^+ ToF progression on uncoated L/D 40 MCP.

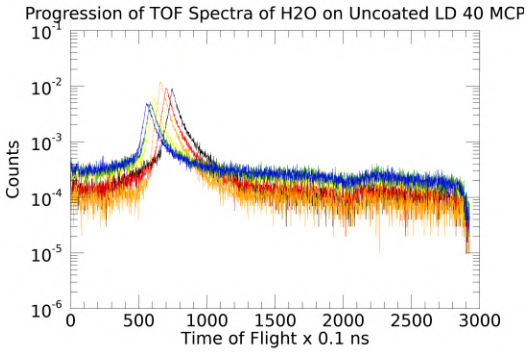

(d) H_2O^+ ToF progression on uncoated L/D 40 MCP.

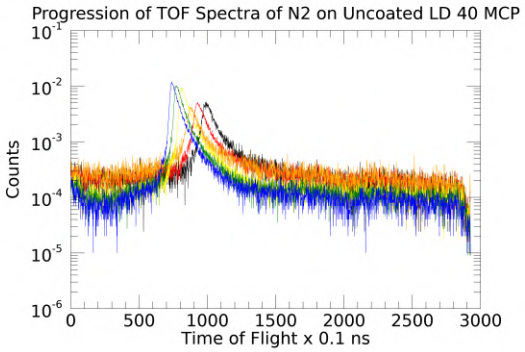

(e) N_2^+ ToF progression on uncoated L/D 40 MCP.

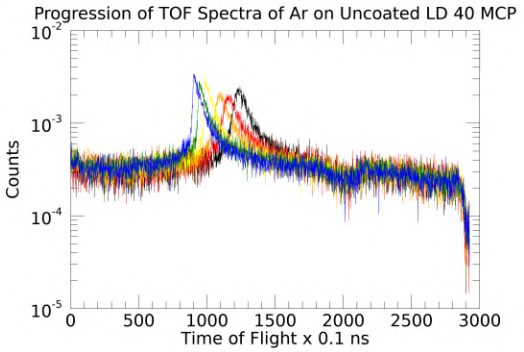

(f) Ar^+ ToF progression on uncoated L/D 40 MCP.

Figure A.3: Time of Flight progression on uncoated L/D 40 MCP due to total energy available to the ion, for various species. Energies included are 15 keV (black), 17 keV (red), 19 keV (orange), 20 keV (yellow), 22 keV (green), 24 keV (blue), 25 keV (violet), 27 keV (indigo), 29 keV (brown). Note only H_2^+ and protons range from 20 - 29 keV in energy, and all the others range from 15 - 24 keV.

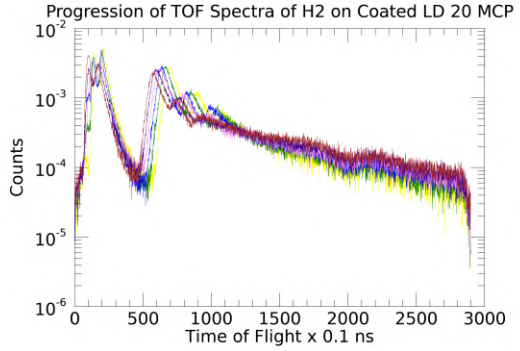

(a) H_2^+ ToF progression on Al_2O_3 coated $^L/_D$ 20 MCP.

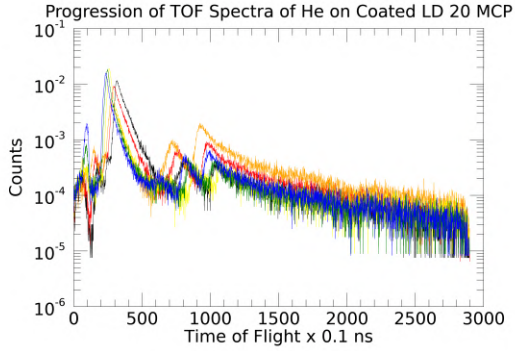

(b) He^+ ToF progression on Al_2O_3 coated $^L/_D$ 20 MCP.

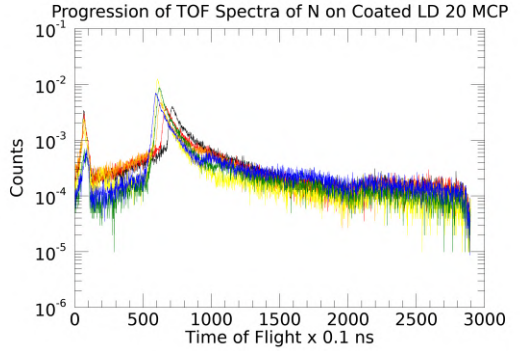

(c) N^+ ToF progression on Al_2O_3 coated $^L/_D$ 20 MCP.

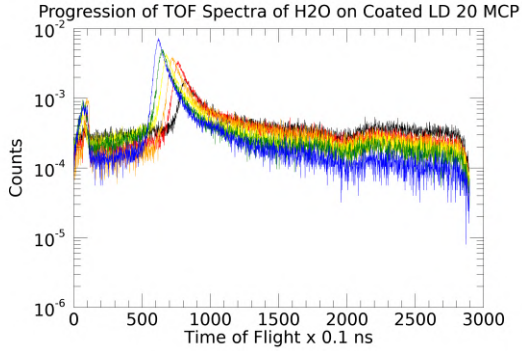

(d) H_2O^+ ToF progression on Al_2O_3 coated $^L/_D$ 20 MCP.

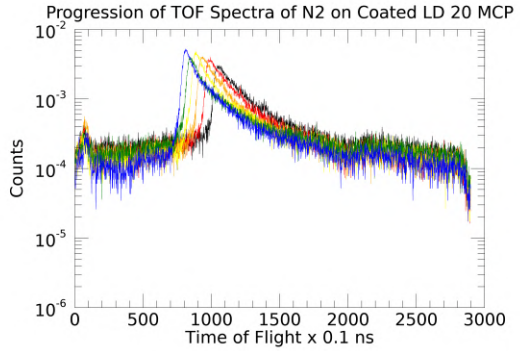

(e) N_2^+ ToF progression on Al_2O_3 coated $^L/_D$ 20 MCP.

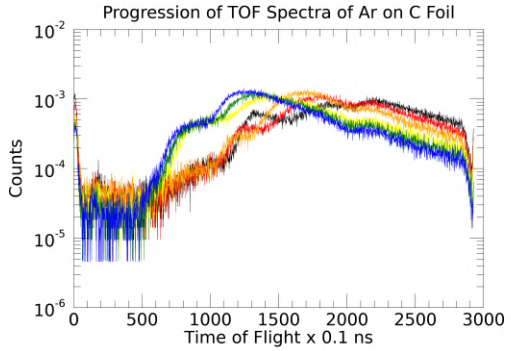

(f) Ar^+ ToF progression on Al_2O_3 coated $^L/_D$ 20 MCP.

Figure A.4: Time of Flight progression due to total energy available to the ion, for various species. Energies included are 15 keV (black), 17 keV (red), 19 keV (orange), 20 keV (yellow), 22 keV (green), 24 keV (blue), 25 keV (violet), 27 keV (indigo), 29 keV (brown). Note only H_2^+ and protons range from 20 - 29 keV in energy, and all the others range from 15 - 24 keV.

A.2 Time of Flight Carbon Foil-MCP Comparisons

This portion of the Appendix investigates the comparison of ions between all the MCPs tested. Figures A.5-A.10 compare the normalized MCP spectra taken to that of the carbon foil for all ions and energy ranges. Key parameters of each of these spectra include the FWHM of the ToF, indicative of the scattering observed by the ion, as well as the position in time of the centroid of the distribution, indicative of the mean energy after scattering. Geometrical effects of the MCPs operating under grazing incidence drastically improve both these quantities for almost all ions. The light ions are comparable to the carbon foil, while the heavy ions are drastically improved in mass resolution. Coatings marginally affect these parameters, while geometry is much more significant.

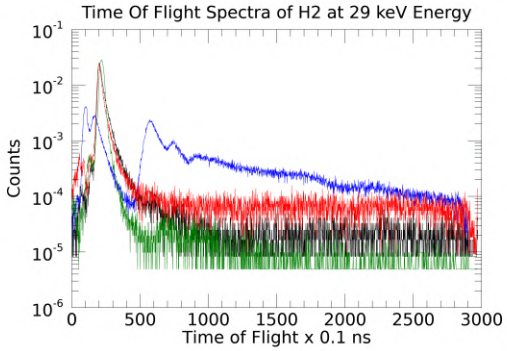

(a) ToF spectra for a total energy 29 keV H_2^+ ion beam.

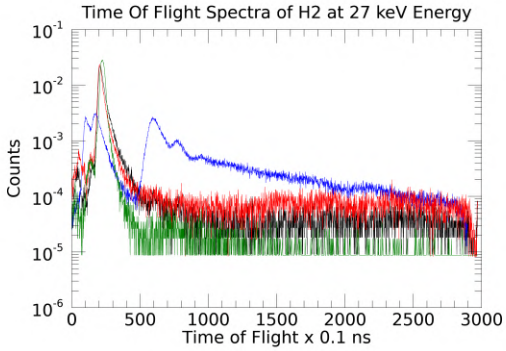

(b) ToF spectra for a total energy 27 keV H_2^+ ion beam.

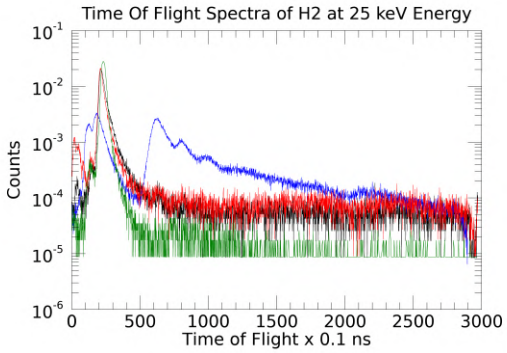

(c) ToF spectra for a total energy 25 keV H_2^+ ion beam.

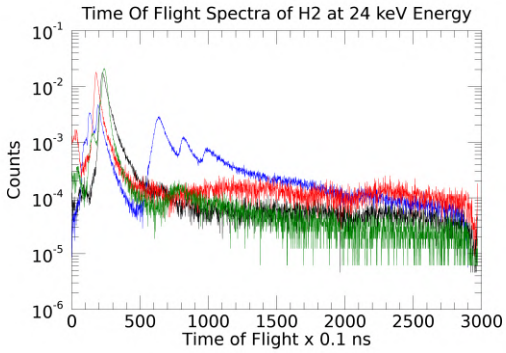

(d) ToF spectra for a total energy 24 keV H_2^+ ion beam.

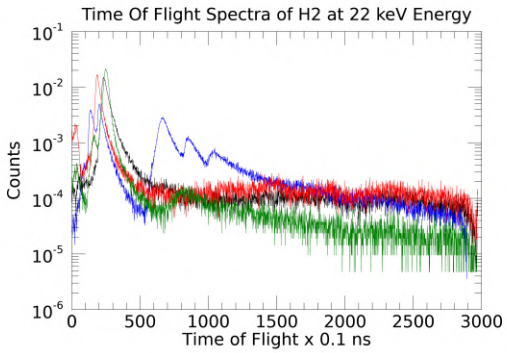

(e) ToF spectra for a total energy 22 keV H_2^+ ion beam.

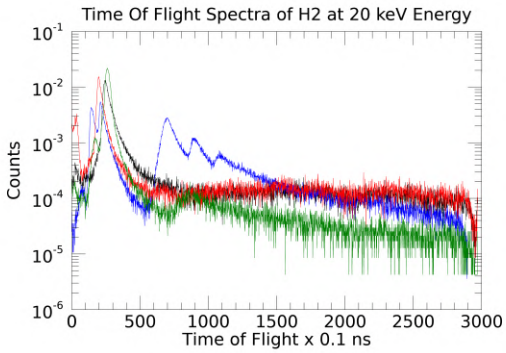

(f) ToF spectra for a total energy 20 keV H_2^+ ion beam.

Figure A.5: Time-of-Flight spectra comparison of H_2^+ between an uncoated L/D 20 MCP (black), uncoated L/D 40 MCP (red), aluminum oxide coated L/D 20 MCP (blue), and a traditional carbon foil (green). Note that the coated L/D 20 MCP spectra has much more sputtering involved; the H_2^+ has been more easily broken apart and a proton peak is visible, as well as heavier sputtered elements from the beamline.

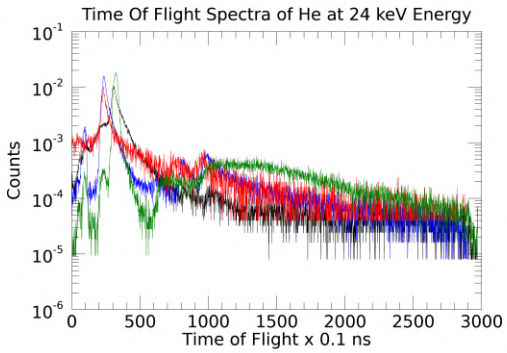

(a) ToF spectra for a total energy 24 keV He^+ ion beam.

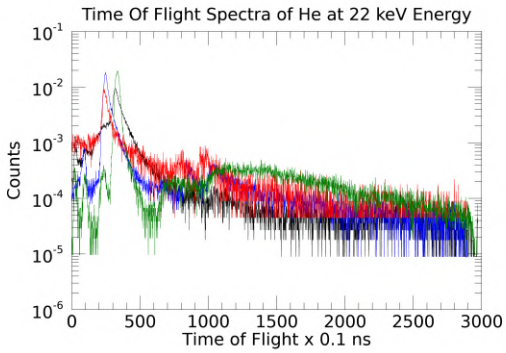

(b) ToF spectra for a total energy 22 keV He^+ ion beam.

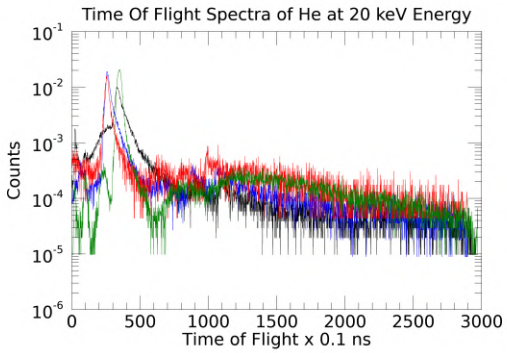

(c) ToF spectra for a total energy 20 keV He^+ ion beam.

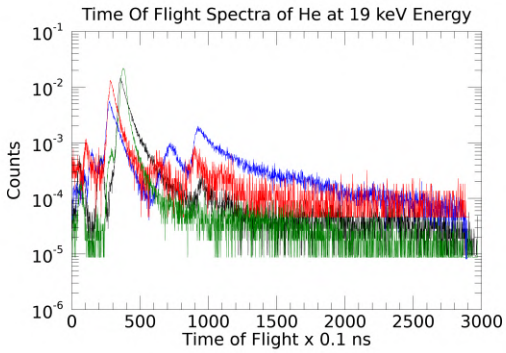

(d) ToF spectra for a total energy 19 keV He^+ ion beam.

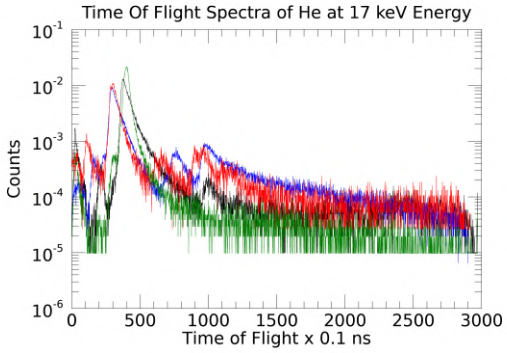

(e) ToF spectra for a total energy 17 keV He^+ ion beam.

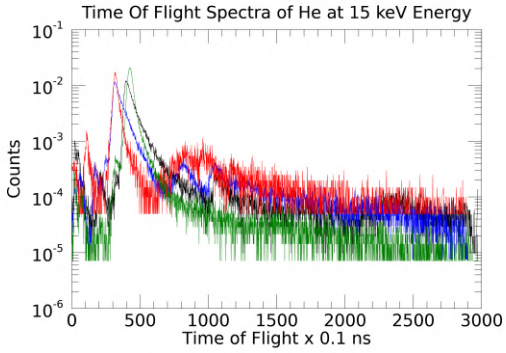

(f) ToF spectra for a total energy 15 keV He^+ ion beam.

Figure A.6: Time-of-Flight spectra comparison of He^+ between an uncoated $^L/_D$ 20 MCP (black), uncoated $^L/_D$ 40 MCP (red), aluminum oxide coated $^L/_D$ 20 MCP (blue), and a traditional carbon foil (green).

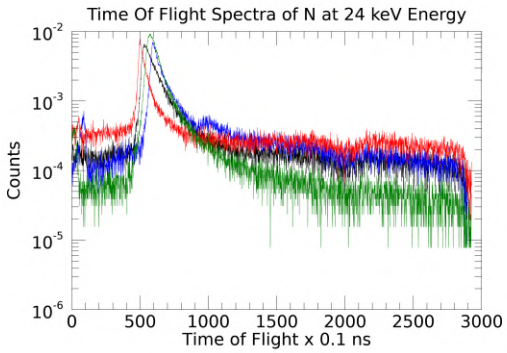

(a) ToF spectra for a total energy 24 keV N^+ ion beam.

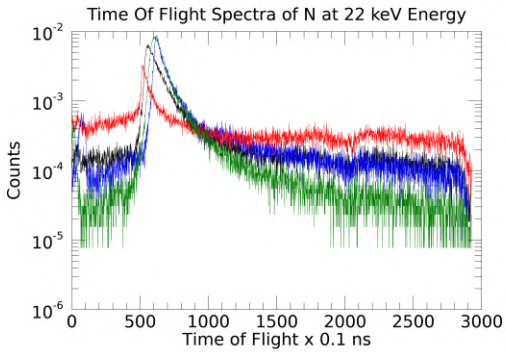

(b) ToF spectra for a total energy 22 keV N^+ ion beam.

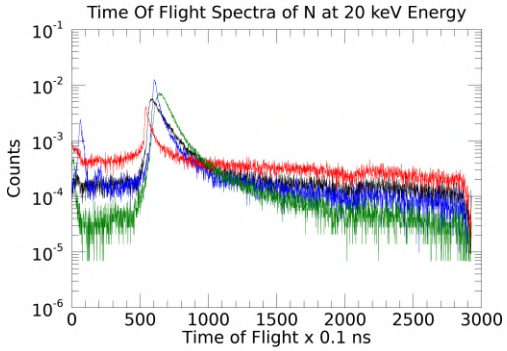

(c) ToF spectra for a total energy 20 keV N^+ ion beam.

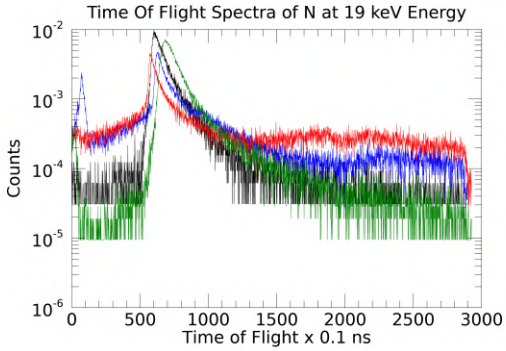

(d) ToF spectra for a total energy 19 keV N^+ ion beam.

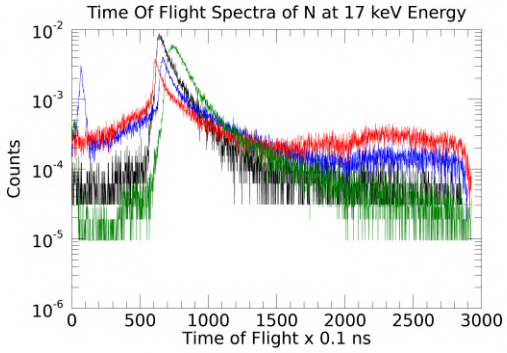

(e) ToF spectra for a total energy 17 keV N^+ ion beam.

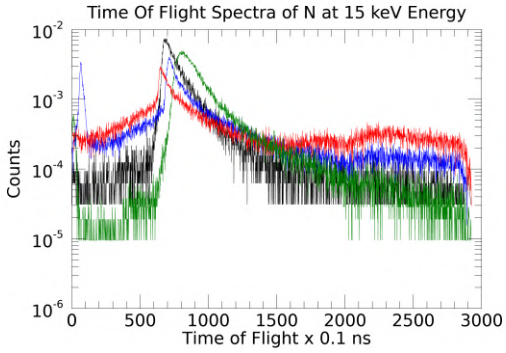

(f) ToF spectra for a total energy 15 keV N^+ ion beam.

Figure A.7: Time-of-Flight spectra comparison of N^+ between an uncoated $^L/_D$ 20 MCP (black), uncoated $^L/_D$ 40 MCP (red), aluminum oxide coated $^L/_D$ 20 MCP (blue), and a traditional carbon foil (green).

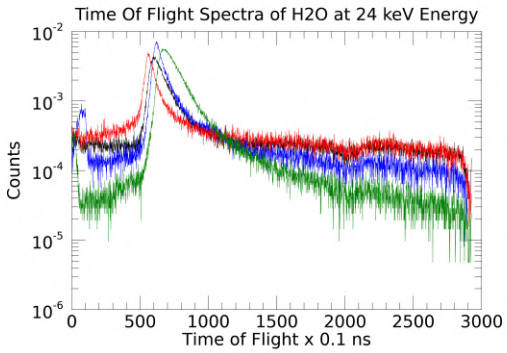

(a) ToF spectra for a total energy 24 keV H_2O^+ ion beam.

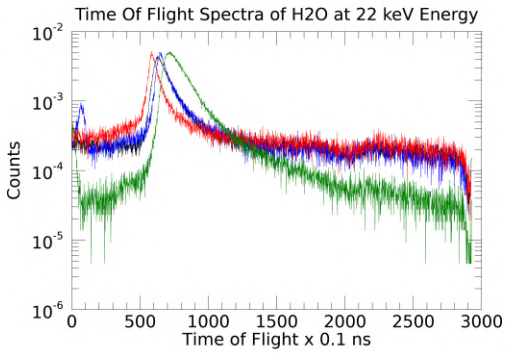

(b) ToF spectra for a total energy 22 keV H_2O^+ ion beam.

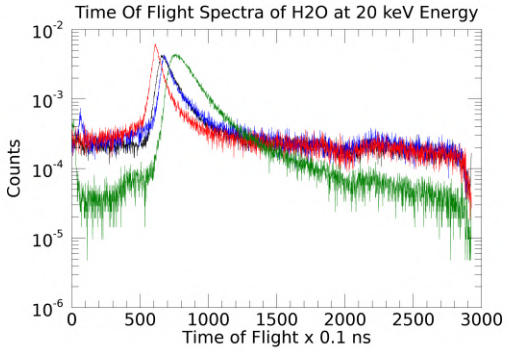

(c) ToF spectra for a total energy 20 keV H_2O^+ ion beam.

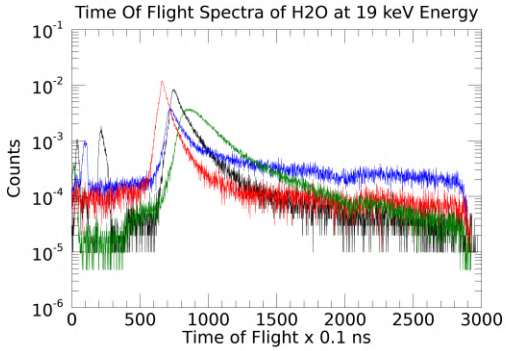

(d) ToF spectra for a total energy 19 keV H_2O^+ ion beam.

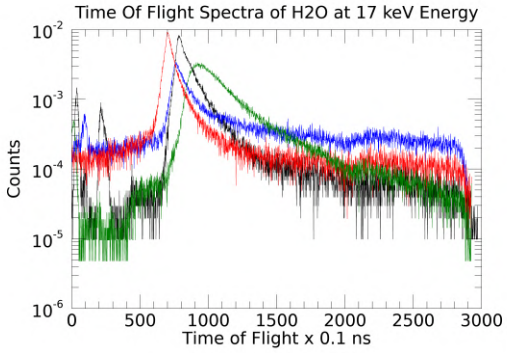

(e) ToF spectra for a total energy 17 keV H_2O^+ ion beam.

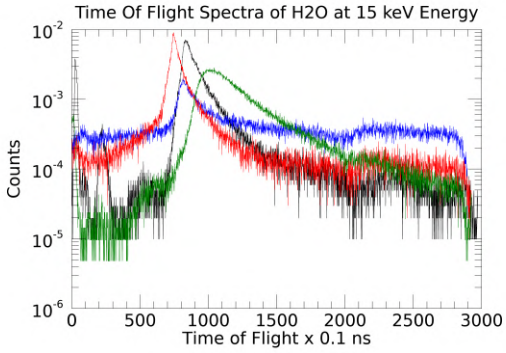

(f) ToF spectra for a total energy 15 keV H_2O^+ ion beam.

Figure A.8: Time-of-Flight spectra comparison of H_2O^+ between an uncoated $^L/_D$ 20 MCP (black), uncoated $^L/_D$ 40 MCP (red), aluminum oxide coated $^L/_D$ 20 MCP (blue), and a traditional carbon foil (green).

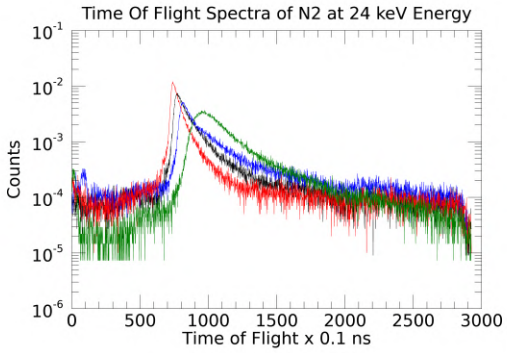

(a) ToF spectra for a total energy 24 keV N_2^+ ion beam.

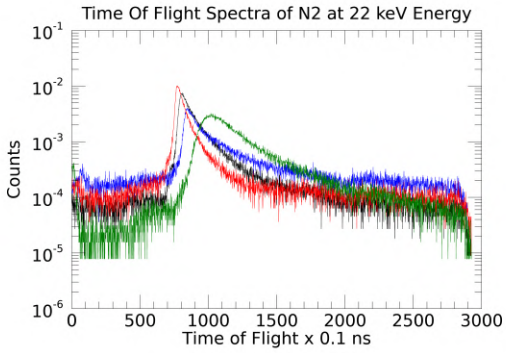

(b) ToF spectra for a total energy 22 keV N_2^+ ion beam.

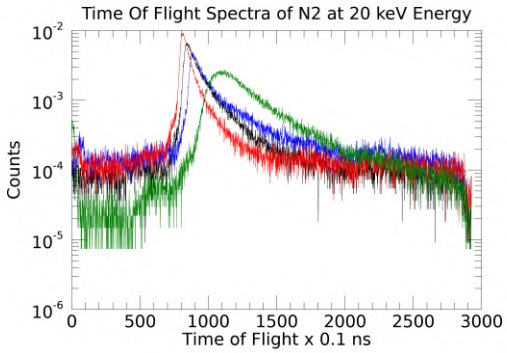

(c) ToF spectra for a total energy 20 keV N_2^+ ion beam.

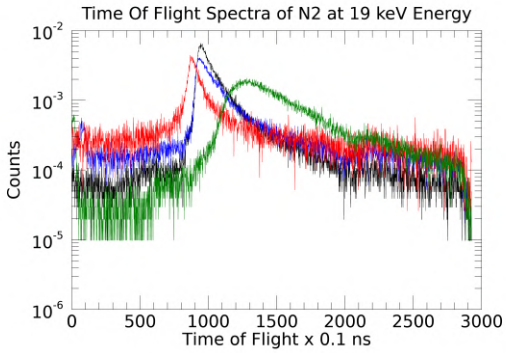

(d) ToF spectra for a total energy 19 keV N_2^+ ion beam.

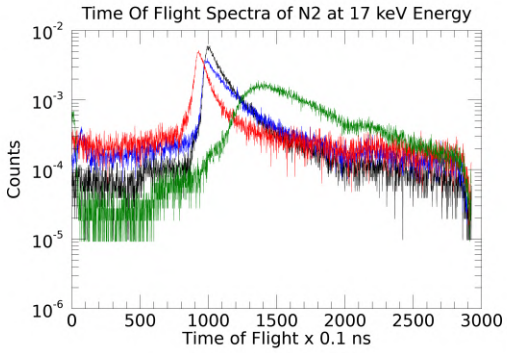

(e) ToF spectra for a total energy 17 keV N_2^+ ion beam.

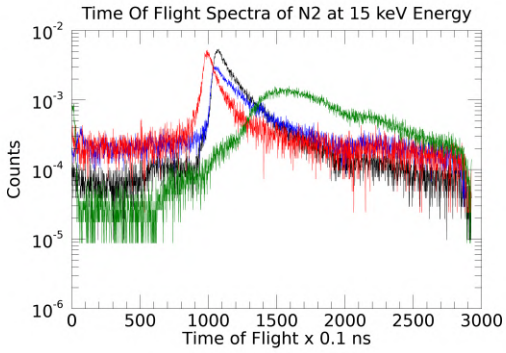

(f) ToF spectra for a total energy 15 keV N_2^+ ion beam.

Figure A.9: Time-of-Flight spectra comparison of N_2^+ between an uncoated L/D 20 MCP (black), uncoated L/D 40 MCP (red), aluminum oxide coated L/D 20 MCP (blue), and a traditional carbon foil (green).

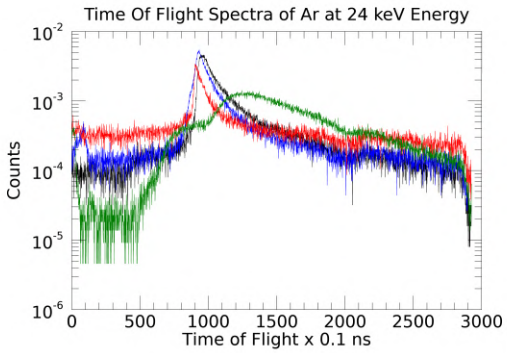

(a) ToF spectra for a total energy 24 keV Ar^+ ion beam.

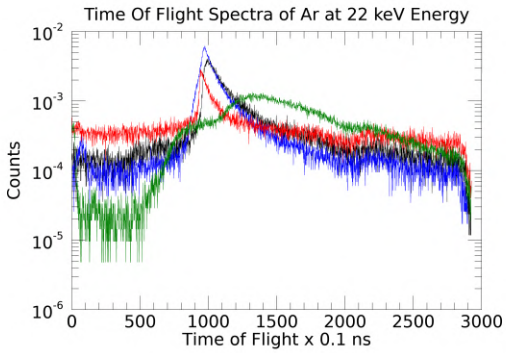

(b) ToF spectra for a total energy 22 keV Ar^+ ion beam.

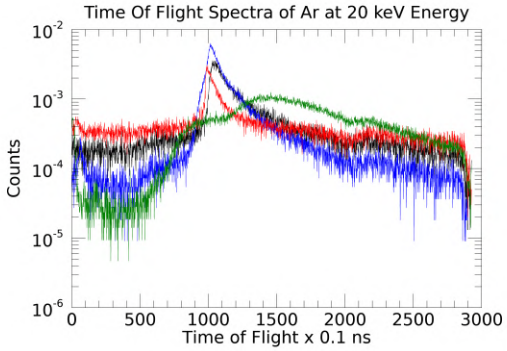

(c) ToF spectra for a total energy 20 keV Ar^+ ion beam.

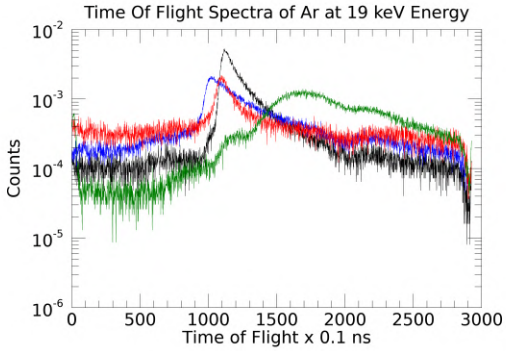

(d) ToF spectra for a total energy 19 keV Ar^+ ion beam.

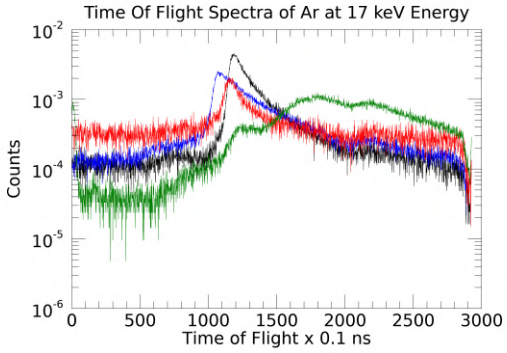

(e) ToF spectra for a total energy 17 keV Ar^+ ion beam.

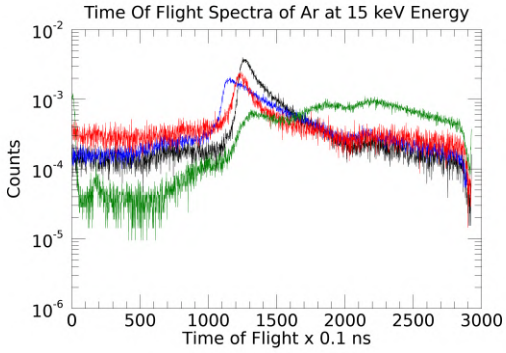

(f) ToF spectra for a total energy 15 keV Ar^+ ion beam.

Figure A.10: Time-of-Flight spectra comparison of Ar^+ between an uncoated $^L/_D$ 20 MCP (black), uncoated $^L/_D$ 40 MCP (red), aluminum oxide coated $^L/_D$ 20 MCP (blue), and a traditional carbon foil (green).

B SRIM/TRIM Spectra

This portion of the Appendix investigates the trends of SRIM/TRIM simulated ions as the total kinetic energy and the angle of incidence is varied. Figures B.1-B.12 cover all the derived parameters important for a detector after simulated scattering of 50000 ions occurs, per each surface and energy. Included are the angular induced change in the centroid position in time, FWHM, and scattering fluxes. These fluxes include the total number observed specularly reflecting, backscattered back out the entrance, and those scattered beyond recognition (larger ToF than 300 ns) respectively. These quantities are used to determine the energy and angular responses that were depicted in Section 5.

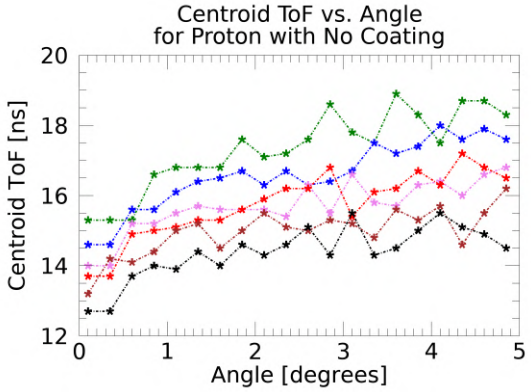

(a) Centroid of Time of Flight spectra of protons as a function of incident angle, using SRIM.

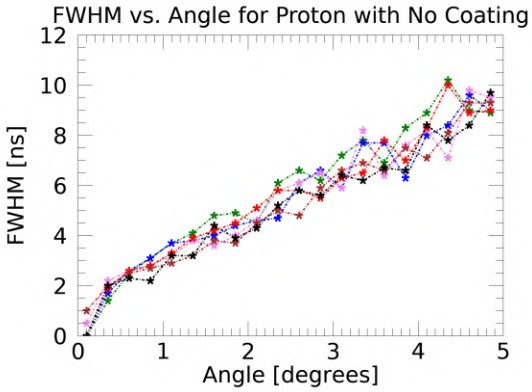

(b) FWHM of protons as a function of incident angle, using SRIM.

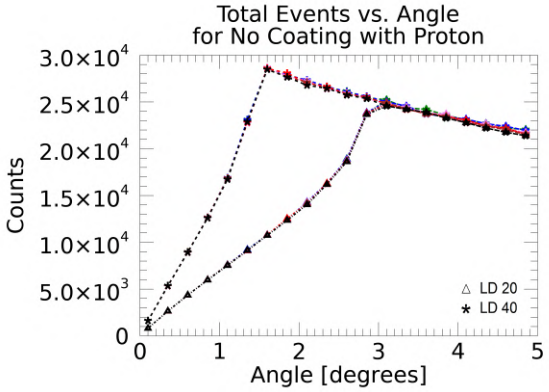

(c) Flux of successful specularly reflected protons using SRIM.

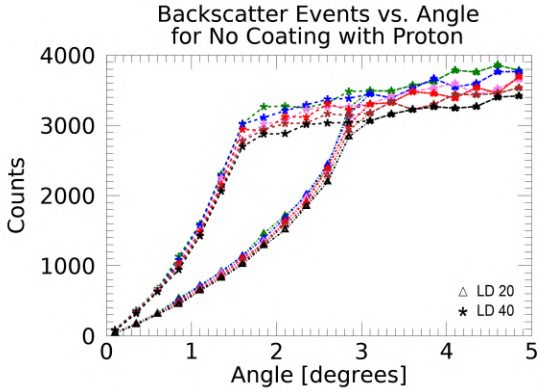

(d) Flux of protons backscattered back out the entrance of the MCP, using SRIM.

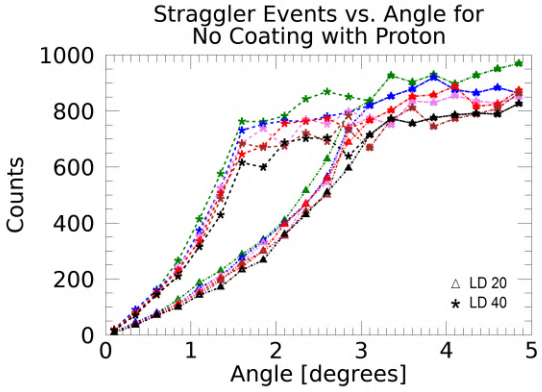

(e) SRIM simulated flux of protons that are scattered to the point of non-detection using CODIF, which are time of flights longer than 300 ns.

Figure B.1: Centroid time of flight, spectra FWHM, and various geometry-corrected rate data of proton ions for 29 keV (black), 27 keV (brown), 25 keV (red), 24 keV (violet), 22 keV (blue), 20 keV (green) impinging on an uncoated MCP.

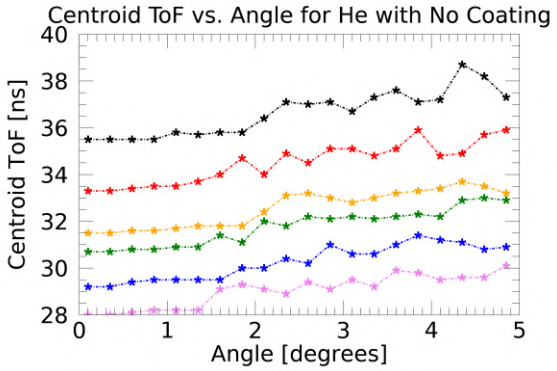

(a) Centroid of Time of Flight spectra of helium as a function of incident angle, using SRIM.

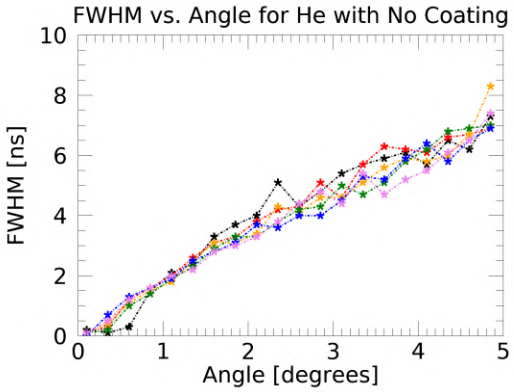

(b) FWHM of helium as a function of incident angle, using SRIM.

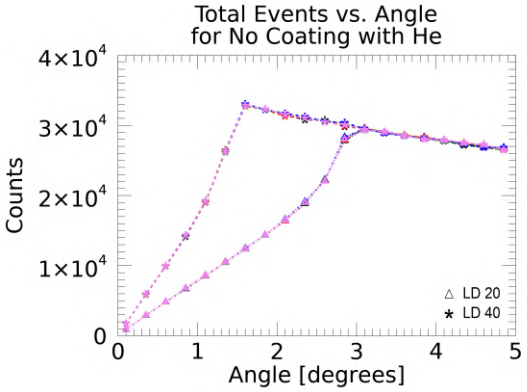

(c) Flux of successful specularly reflected helium ions using SRIM.

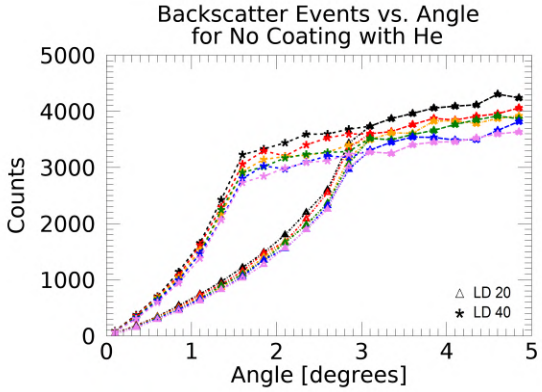

(d) Flux of helium ions backscattered back out the entrance of the MCP, using SRIM.

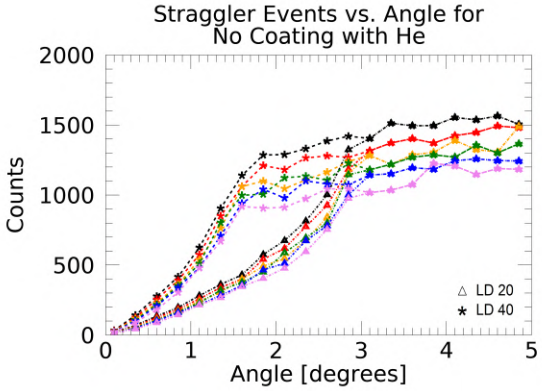

(e) SRIM simulated flux of helium ions that are scattered to the point of non-detection using CODIF, which are time of flights longer than 300 ns.

Figure B.2: Centroid time of flight, spectra FWHM, and various geometry-corrected rate data of helium ions for 24 keV (black), 22 keV (purple), 20 keV (blue), 19 keV (green), 17 keV (orange), 15 keV (red) impinging on an uncoated MCP.

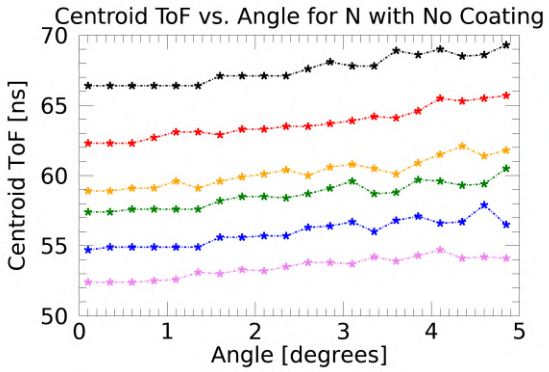

(a) Centroid of Time of Flight spectra of nitrogen as a function of incident angle, using SRIM.

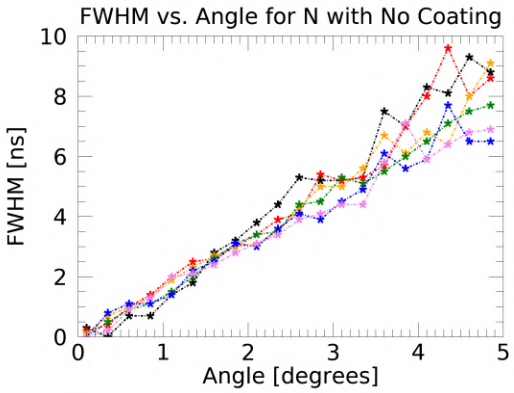

(b) FWHM of nitrogen as a function of incident angle, using SRIM.

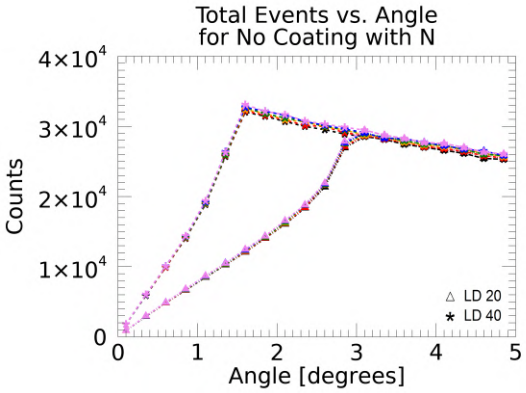

(c) Flux of successful specularly reflected nitrogen ions using SRIM.

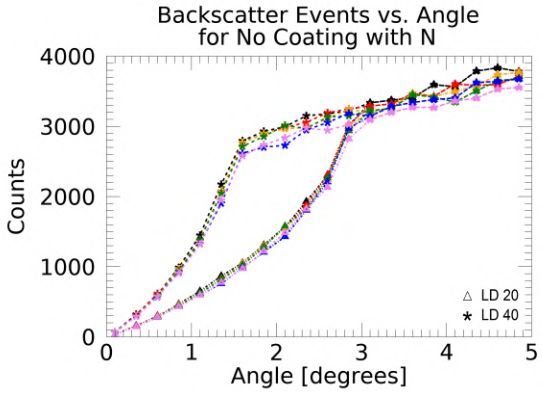

(d) Flux of nitrogen ions backscattered back out the entrance of the MCP, using SRIM.

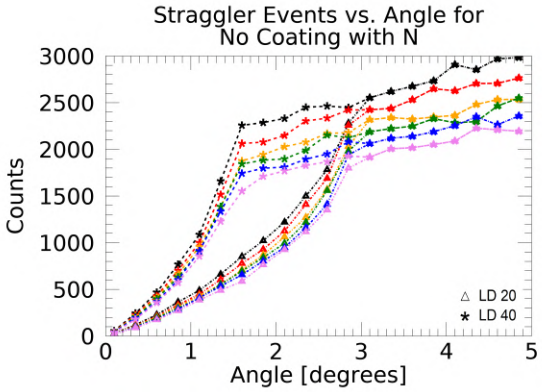

(e) SRIM simulated flux of nitrogen ions that are scattered to the point of non-detection using CODIF, which are time of flights longer than 300 ns.

Figure B.3: Centroid time of flight, spectra FWHM, and various geometry-corrected rate data of nitrogen ions for 24 keV (black), 22 keV (purple), 20 keV (blue), 19 keV (green), 17 keV (orange), 15 keV (red) impinging on an uncoated MCP.

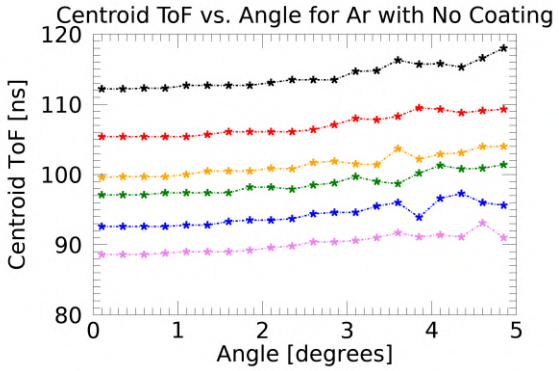

(a) Centroid of Time of Flight spectra of argon ions as a function of incident angle, using SRIM.

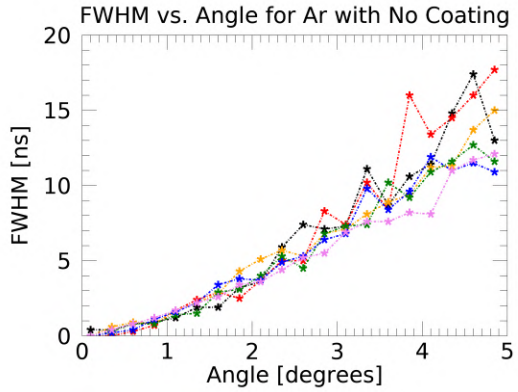

(b) FWHM of argon ions as a function of incident angle, using SRIM.

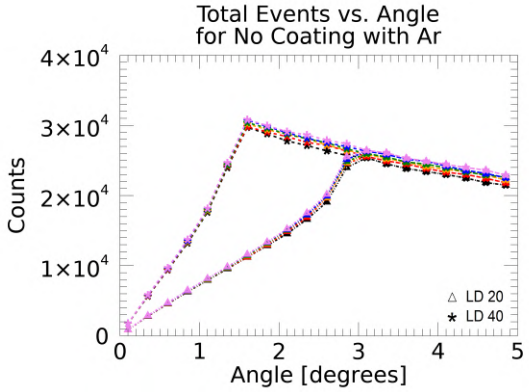

(c) Flux of successful specularly reflected argon ions using SRIM.

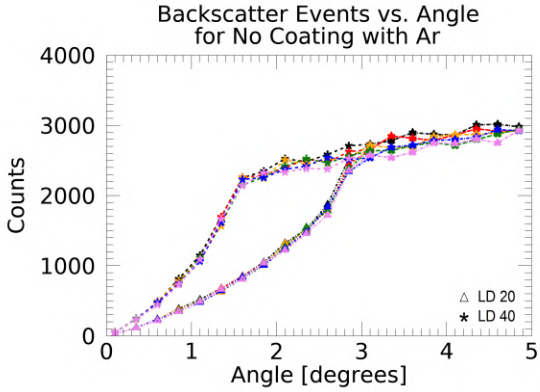

(d) Flux of argon ions backscattered back out the entrance of the MCP, using SRIM.

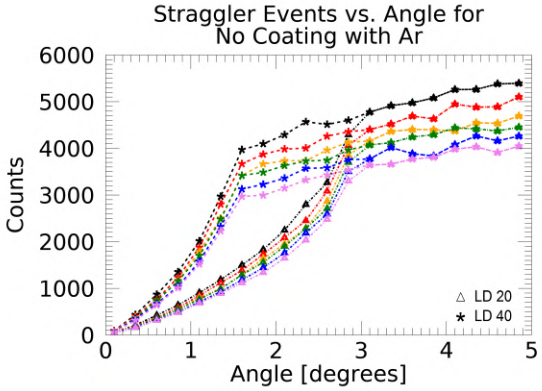

(e) SRIM simulated flux of argon ions that are scattered to the point of non-detection using CODIF, which are time of flights longer than 300 ns.

Figure B.4: Centroid time of flight, spectra FWHM, and various geometry-corrected rate data of argon ions for 24 keV (black), 22 keV (purple), 20 keV (blue), 19 keV (green), 17 keV (orange), 15 keV (red) impinging on an uncoated MCP.

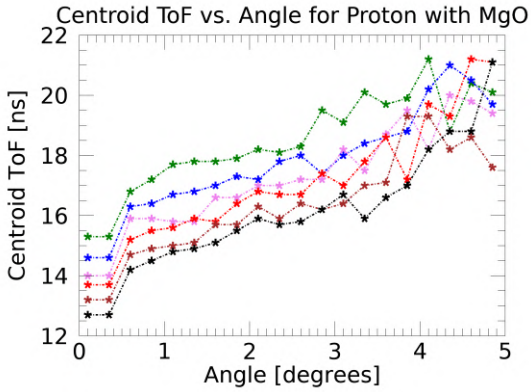

(a) Centroid of Time of Flight spectra of protons as a function of incident angle, using SRIM.

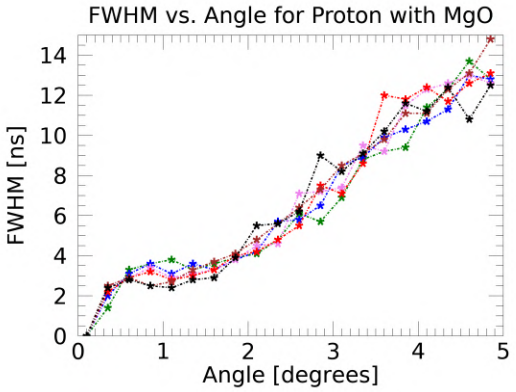

(b) FWHM of protons as a function of incident angle, using SRIM.

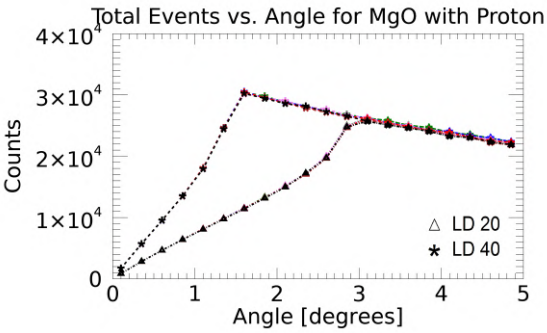

(c) Flux of successful specularly reflected protons using SRIM.

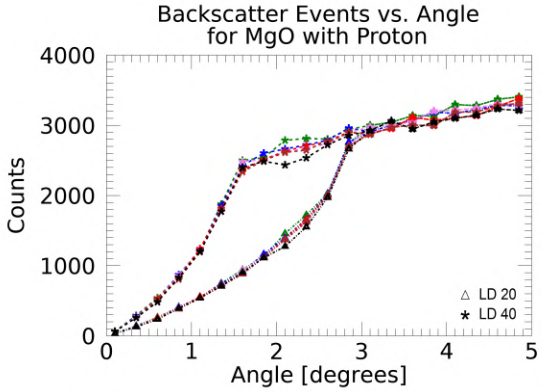

(d) Flux of protons backscattered back out the entrance of the MCP, using SRIM.

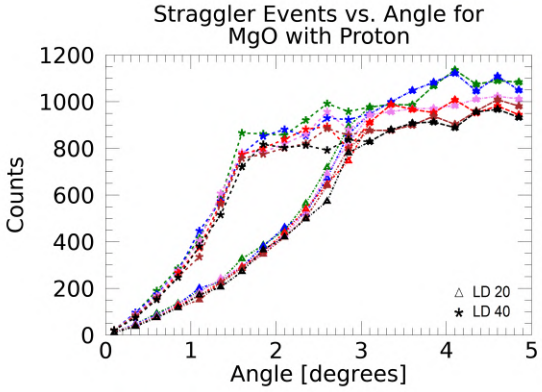

(e) SRIM simulated flux of protons that are scattered to the point of non-detection using CODIF, which are time of flights longer than 300 ns.

Figure B.5: Centroid time of flight, spectra FWHM, and various geometry-corrected rate data of proton ions for 29 keV (black), 27 keV (brown), 25 keV (red), 24 keV (violet), 22 keV (blue), 20 keV (green) impinging on a 60 $\mathring{A}$ layer of MgO.

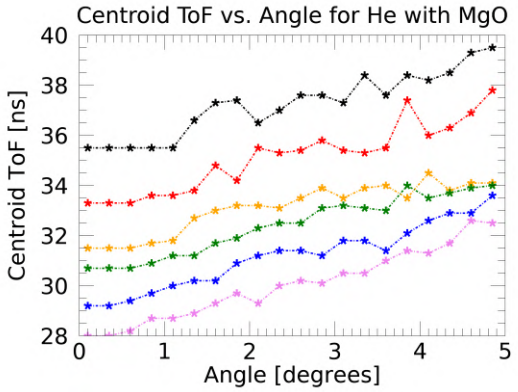

(a) Centroid of Time of Flight spectra of helium as a function of incident angle, using SRIM.

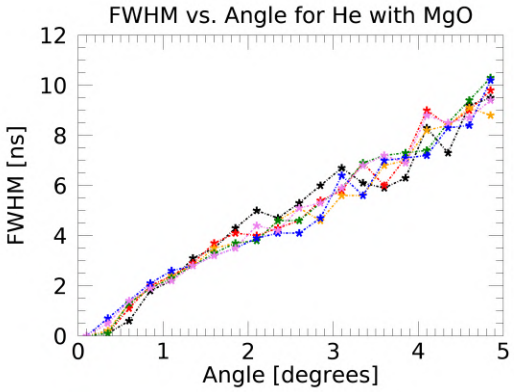

(b) FWHM of helium as a function of incident angle, using SRIM.

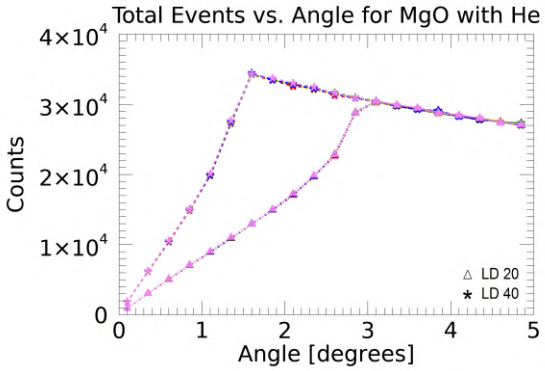

(c) Flux of successful specularly reflected helium ions using SRIM.

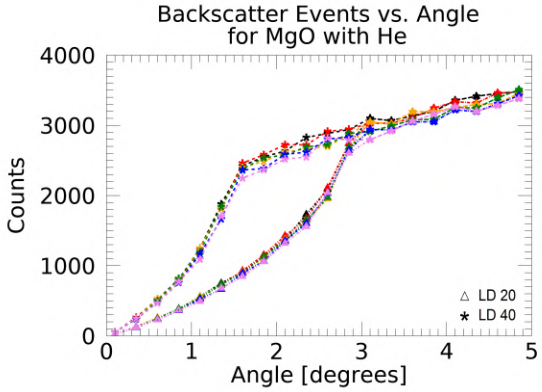

(d) Flux of helium ions backscattered back out the entrance of the MCP, using SRIM.

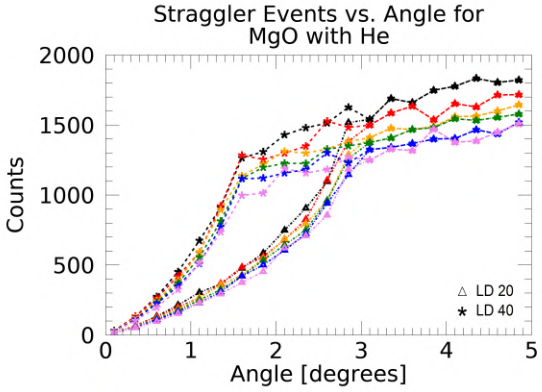

(e) SRIM simulated flux of helium ions that are scattered to the point of non-detection using CODIF, which are time of flights longer than 300 ns.

Figure B.6: Centroid time of flight, spectra FWHM, and various geometry-corrected rate data of helium ions for 24 keV (black), 22 keV (purple), 20 keV (blue), 19 keV (green), 17 keV (orange), 15 keV (red) impinging on a 60 $\AA$ layer of MgO.

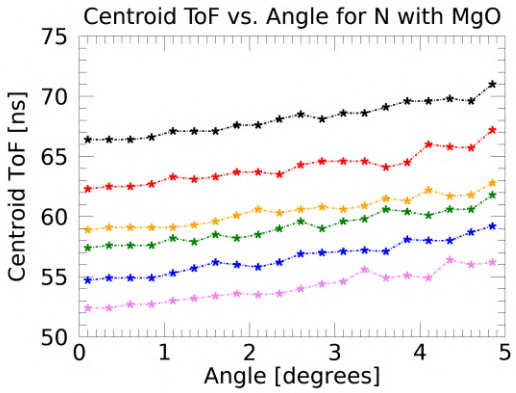

(a) Centroid of Time of Flight spectra of nitrogen as a function of incident angle, using SRIM.

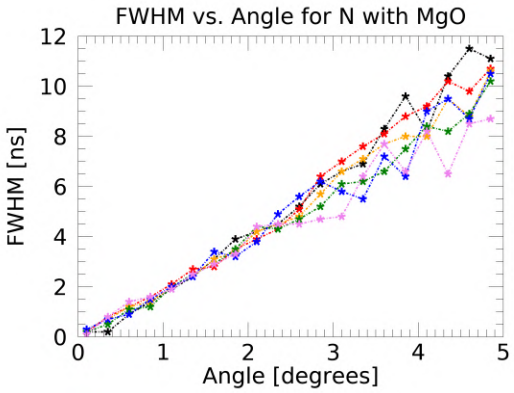

(b) FWHM of nitrogen as a function of incident angle, using SRIM.

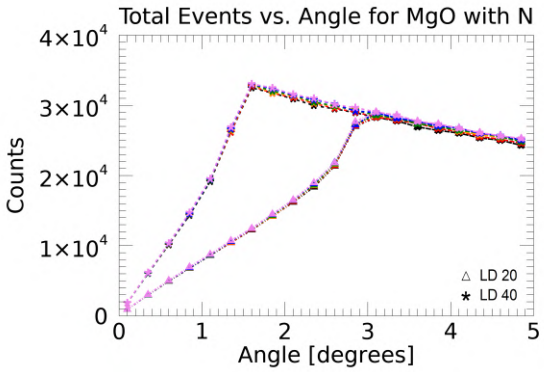

(c) Flux of successful specularly reflected nitrogen ions using SRIM.

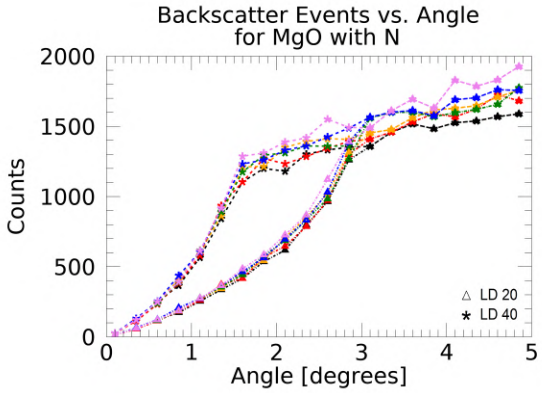

(d) Flux of nitrogen ions backscattered back out the entrance of the MCP, using SRIM.

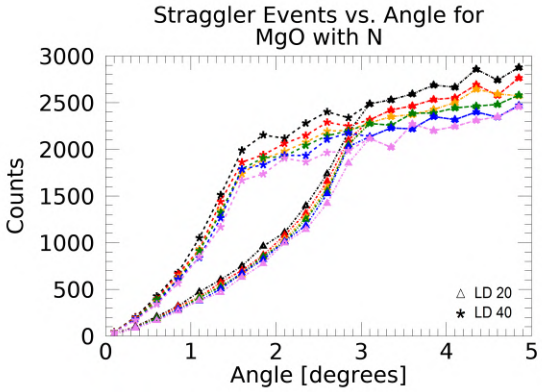

(e) SRIM simulated flux of nitrogen ions that are scattered to the point of non-detection using CODIF, which are time of flights longer than 300 ns.

Figure B.7: Centroid time of flight, spectra FWHM, and various geometry-corrected rate data of nitrogen ions for 24 keV (black), 22 keV (purple), 20 keV (blue), 19 keV (green), 17 keV (orange), 15 keV (red) impinging on a 60 $\AA$ layer of MgO.

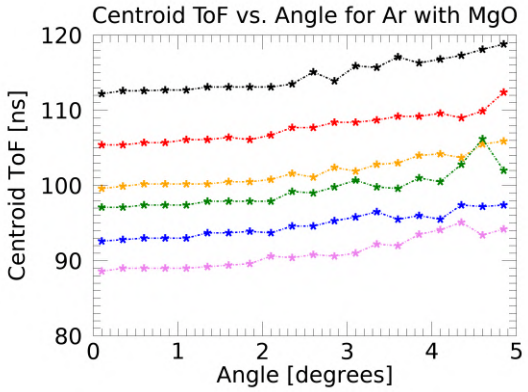

(a) Centroid of Time of Flight spectra of argon ions as a function of incident angle, using SRIM.

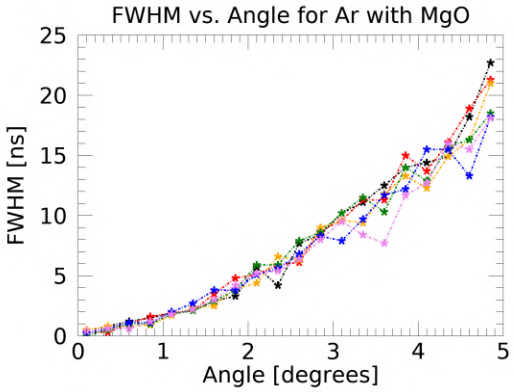

(b) FWHM of argon ions as a function of incident angle, using SRIM.

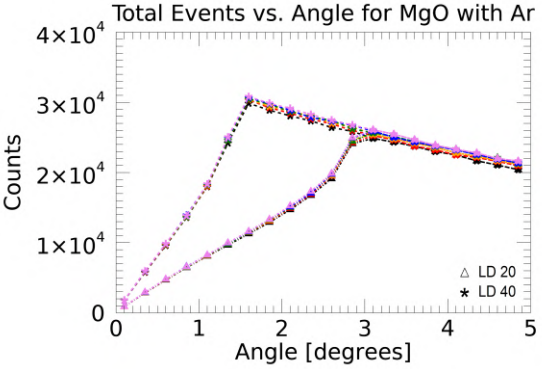

(c) Flux of successful specularly reflected argon ions using SRIM.

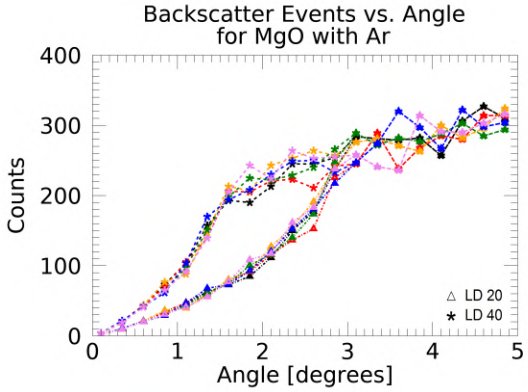

(d) Flux of argon ions backscattered back out the entrance of the MCP, using SRIM.

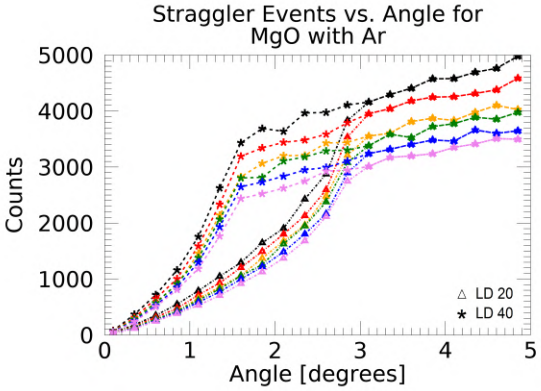

(e) SRIM simulated flux of argon ions that are scattered to the point of non-detection using CODIF, which are time of flights longer than 300 ns.

Figure B.8: Centroid time of flight, spectra FWHM, and various geometry-corrected rate data of argon ions for 24 keV (black), 22 keV (purple), 20 keV (blue), 19 keV (green), 17 keV (orange), 15 keV (red) impinging on a 60 $\mathring{A}$ layer of MgO.

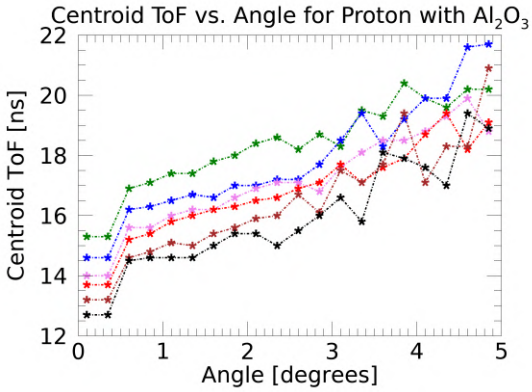

(a) Centroid of Time of Flight spectra of protons as a function of incident angle, using SRIM.

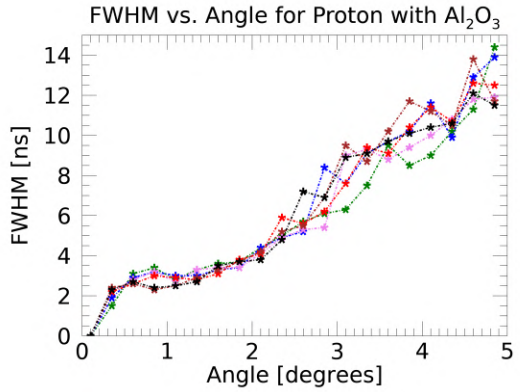

(b) FWHM of protons as a function of incident angle, using SRIM.

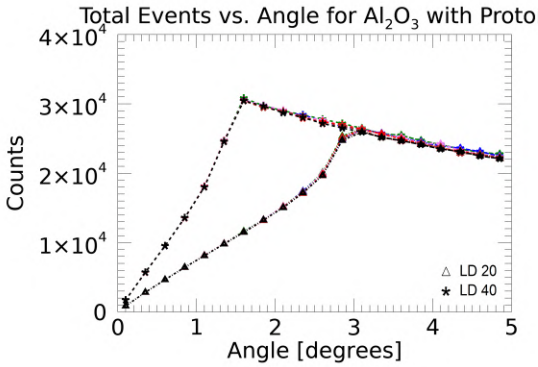

(c) Flux of successful specularly reflected protons using SRIM.

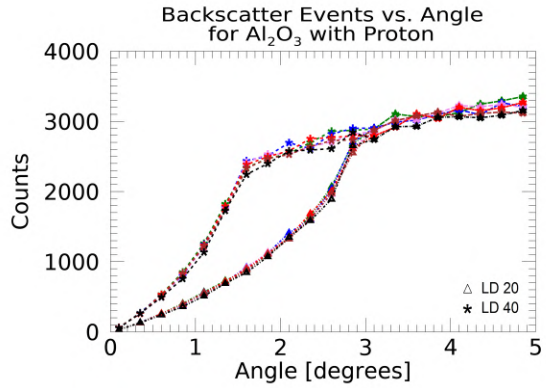

(d) Flux of protons backscattered back out the entrance of the MCP, using SRIM.

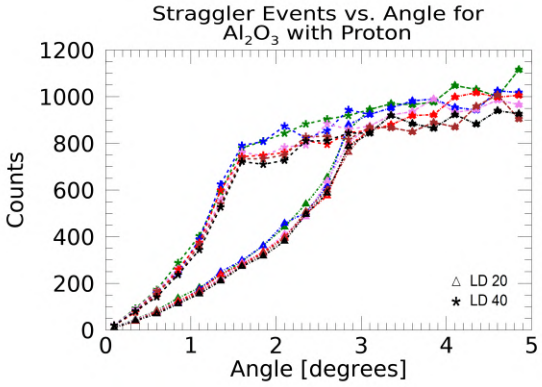

(e) SRIM simulated flux of protons that are scattered to the point of non-detection using CODIF, which are time of flights longer than 300 ns.

Figure B.9: Centroid time of flight, spectra FWHM, and various geometry-corrected rate data of proton ions for 29 keV (black), 27 keV (brown), 25 keV (red), 24 keV (violet), 22 keV (blue), 20 keV (green) impinging on a 60 $\AA$ layer of Al_2O_3.

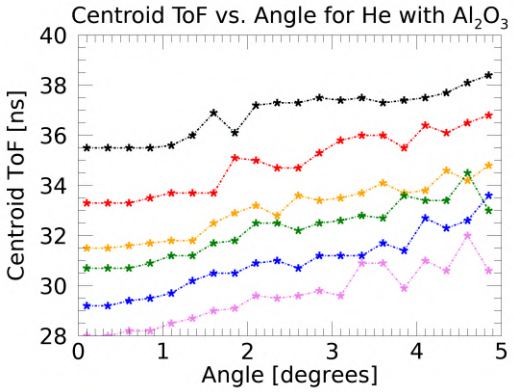

(a) Centroid of Time of Flight spectra of helium as a function of incident angle, using SRIM.

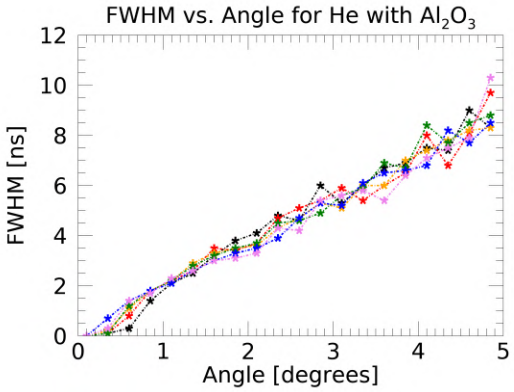

(b) FWHM of helium as a function of incident angle, using SRIM.

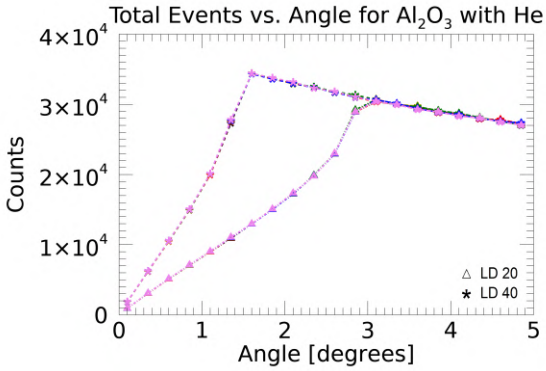

(c) Flux of successful specularly reflected helium ions using SRIM.

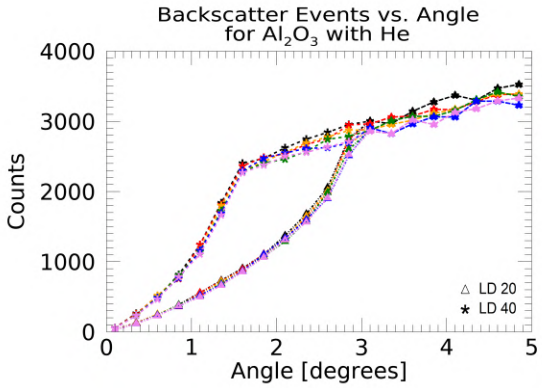

(d) Flux of helium ions backscattered back out the entrance of the MCP, using SRIM.

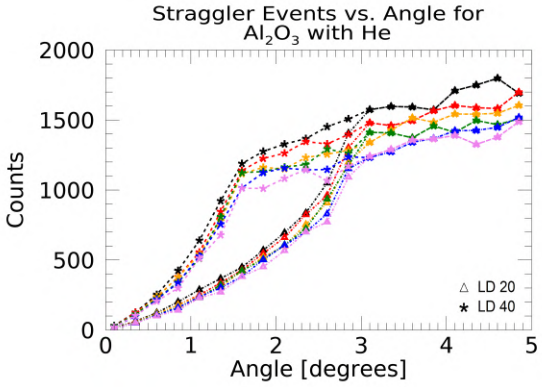

(e) SRIM simulated flux of helium ions that are scattered to the point of non-detection using CODIF, which are time of flights longer than 300 ns.

Figure B.10: Centroid time of flight, spectra FWHM, and various geometry-corrected rate data of helium ions for 24 keV (black), 22 keV (purple), 20 keV (blue), 19 keV (green), 17 keV (orange), 15 keV (red) impinging on a 60 $\mathring{A}$ layer of Al_2O_3.

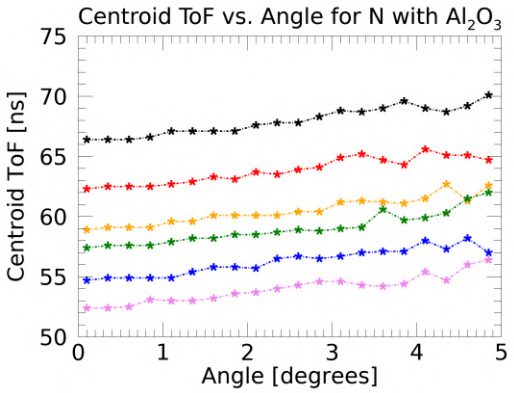

(a) Centroid of Time of Flight spectra of nitrogen as a function of incident angle, using SRIM.

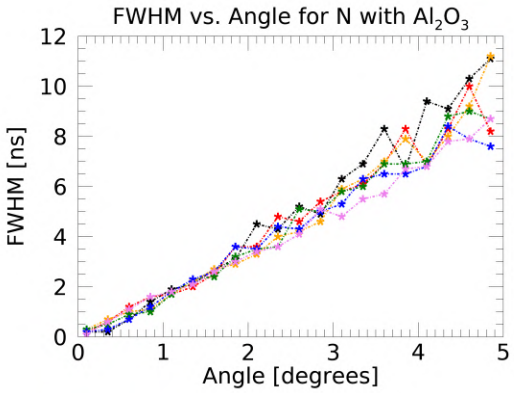

(b) FWHM of nitrogen as a function of incident angle, using SRIM.

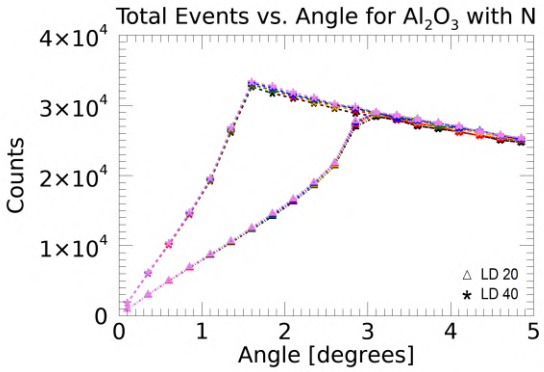

(c) Flux of successful specularly reflected nitrogen ions using SRIM.

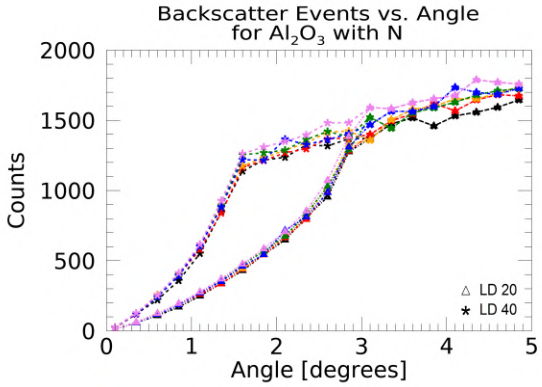

(d) Flux of nitrogen ions backscattered back out the entrance of the MCP, using SRIM.

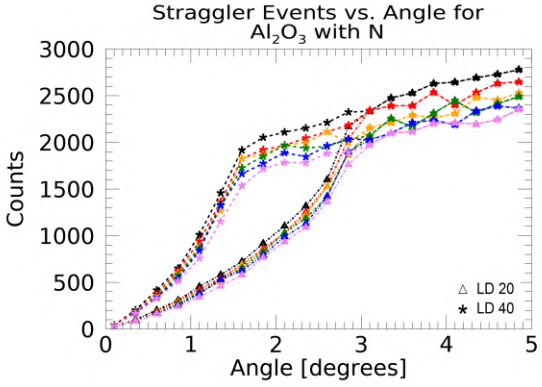

(e) SRIM simulated flux of nitrogen ions that are scattered to the point of non-detection using CODIF, which are time of flights longer than 300 ns.

Figure B.11: Centroid time of flight, spectra FWHM, and various geometry-corrected rate data of nitrogen ions for 24 keV (black), 22 keV (purple), 20 keV (blue), 19 keV (green), 17 keV (orange), 15 keV (red) impinging on a 60 $\mathring{A}$ layer of Al_2O_3.

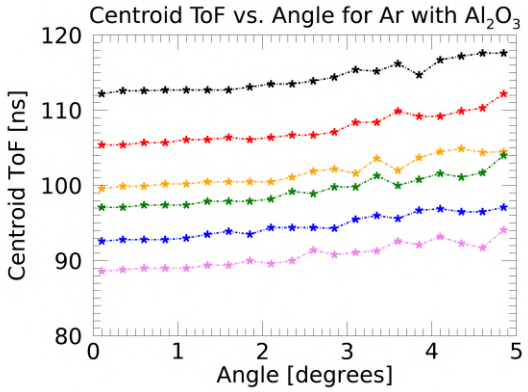

(a) Centroid of Time of Flight spectra of argon ions as a function of incident angle, using SRIM.

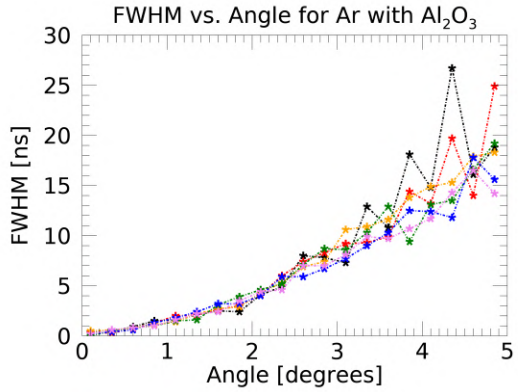

(b) FWHM of argon ions as a function of incident angle, using SRIM.

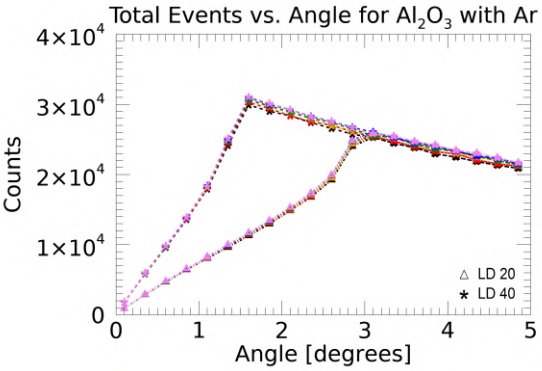

(c) Flux of successful specularly reflected argon ions using SRIM.

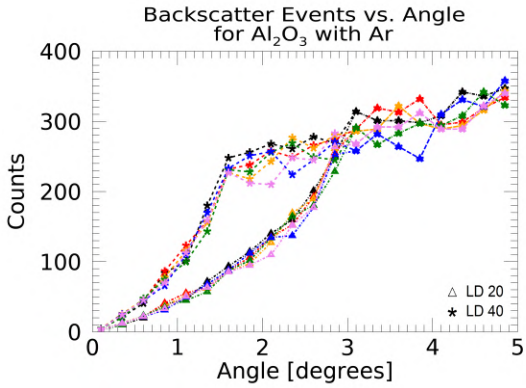

(d) Flux of argon ions backscattered back out the entrance of the MCP, using SRIM.

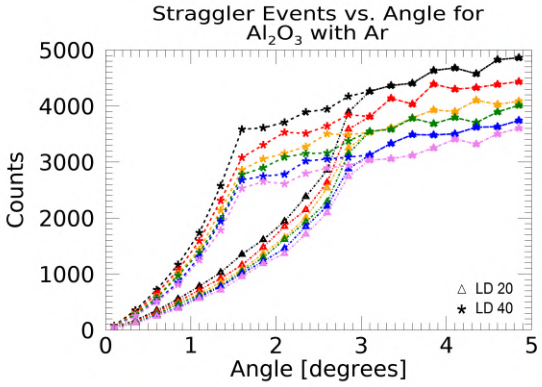

(e) SRIM simulated flux of argon ions that are scattered to the point of non-detection using CODIF, which are time of flights longer than 300 ns.

Figure B.12: Centroid time of flight, spectra FWHM, and various geometry-corrected rate data of argon ions for 24 keV (black), 22 keV (purple), 20 keV (blue), 19 keV (green), 17 keV (orange), 15 keV (red) impinging on a 60 $\mathring{A}$ layer of Al_2O_3.

References

[1] Frederic Allegrini, Robert W Ebert, Stephen A Fuselier, Georgios Nicolaou, Peter V Bedworth, Steve W Sinton, and Karlheinz J Trattner. Charge state of 1 to 50 kev ions after passing through graphene and ultrathin carbon foils. *Optical Engineering*, 53(2):024101, 2014.

[2] Friedrich Aumayr and Hannspeter Winter. Potential electron emission from metal and insulator surfaces. In *Slow Heavy-Particle Induced Electron Emission from Solid Surfaces*, pages 79–112. Springer, 2007.

[3] Stephan BH Bach and Stephen W McElvany. Determination of the ionization potentials of aluminum oxides via charge transfer. *The Journal of Physical Chemistry*, 95(23):9091–9094, 1991.

[4] J Barnstedt. Advanced practical course: Microchannel plate detectors. *Kepler Center for Astro and Particle Physics*, 2009.

[5] Willard H Bennett. Radiofrequency mass spectrometer. *Journal of Applied Physics*, 21(2):143–149, 1950.

[6] RJ Beuhler and L Friedman. A model of secondary electron yields from atomic and polyatomic ion impacts on copper and tungsten surfaces based upon stopping-power calculations. *Journal of Applied Physics*, 48(9):3928–3936, 1977.

[7] C Bouchard and JD Carette. The secondary electron emission coefficient of disordered surfaces. *Surface Science*, 100(1):241–250, 1980.

[8] Hajo Bruining. *Physics and Applications of Secondary Electron Emission: Pergamon Science Series: Electronics and Waves, a Series of Monographs*. Elsevier, 2016.

[9] J. L. Burch, R. B. Torbert, T. D. Phan, L.-J. Chen, T. E. Moore, R. E. Ergun, J. P. Eastwood, and et al. Electron-scale measurements of magnetic reconnection in space. *Science*, 352(6290), 2016.

[10] JL Burch, TE Moore, RB Torbert, and BL Giles. Magnetospheric multiscale overview and science objectives. *Space Science Reviews*, 199(1-4):5–21, 2016.

[11] A Cadu, P Devoto, P Louarn, and J-A Sauvaud. Development of grazing incidence devices for space-borne time of flight mass spectrometry. In *EGU General Assembly Conference Abstracts*, volume 14, page 3390, 2012.

[12] SA Canney, VA Sashin, MJ Ford, and AS Kheifets. Electronic band structure of magnesium and magnesium oxide: experiment and theory. *Journal of Physics: Condensed Matter*, 11(39):7507, 1999.

[13] CW Carlson and JP McFadden. Design and application of imaging plasma instruments. *Measurement Techniques in Space Plasmas: Particles*, pages 125–140, 1998.

[14] CR Chappell, RC Olsen, JL Green, JFE Johnson, and JH Waite. The discovery of nitrogen ions in the earth's magnetosphere. *Geophysical Research Letters*, 9(9):937–940, 1982.

[15] YS Choi and JM Kim. Monte carlo simulations for tilted-channel electron multipliers. *IEEE Transactions On electron devices*, 47(6):1293–1296, 2000.

[16] Robert B Cody, Jun Tamura, and Brian D Musselman. Electrospray ionization/magnetic sector mass spectrometry: calibration, resolution, and accurate mass measurements. *Analytical Chemistry*, 64(14):1561–1570, 1992.

[17] Ioannis A Daglis, Richard M Thorne, Wolfgang Baumjohann, and Stefano Orsini. The terrestrial ring current: Origin, formation, and decay. *Reviews of Geophysics*, 37(4):407–438, 1999.

[18] David A Dahl. Simion for the personal computer in reflection. *International Journal of Mass Spectrometry*, 200(1-3):3–25, 2000.

[19] NF Dalleska and PB Armentrout. Guided ion beam studies of reactions of alkaline earth ions with o2. *International Journal of Mass Spectrometry and Ion Processes*, 134(2-3):203–212, 1994.

[20] P Devoto, J-L Médale, and J-A Sauvaud. Secondary electron emission from distributed ion scattering off surfaces for space instrumentation. *Review of Scientific Instruments*, 79(4):046111, 2008.

[21] Donald J Douglas, Aaron J Frank, and Dunmin Mao. Linear ion traps in mass spectrometry. *Mass spectrometry reviews*, 24(1):1–29, 2005.

[22] Edward H Eberhardt. Gain model for microchannel plates. *Applied Optics*, 18(9):1418–1423, 1979.

[23] C Ertley, OHW Siegmund, J Schwarz, AU Mane, MJ Minot, A O'Mahony, CA Craven, and M Popecki. Characterization of borosilicate microchannel plates functionalized by atomic layer deposition. In *UV, x-ray, and gamma-ray space instrumentation for astronomy XIX*, volume 9601, page 96010S. International Society for Optics and Photonics, 2015.

[24] Casey C Farnell, Cody C Farnell, Shawn C Farnell, and John D Williams. Electrostatic analyzers with application to electric propulsion testing. 2013.

[25] Elena O Filatova and Aleksei S Konashuk. Interpretation of the changing the band gap of al2o3 depending on its crystalline form: connection with different local symmetries. *The Journal of Physical Chemistry C*, 119(35):20755–20761, 2015.

[26] GW Fraser. The ion detection efficiency of microchannel plates (mcps). *International Journal of Mass Spectrometry*, 215(1):13–30, 2002.

[27] SY Fu, Q-G Zong, B Wilken, and ZY Pu. Temporal and spatial variation of the ion composition in the ring current. *Space Science Reviews*, 95(1-2):539–554, 2001.

[28] SY Fu, QG Zong, TA Fritz, ZY Pu, and B Wilken. Composition signatures in ion injections and its dependence on geomagnetic conditions. *Journal of Geophysical Research: Space Physics*, 107(A10), 2002.

[29] AJ Guest. A computer model of channel multiplier plate performance. *Acta Electronica*, 14(1):79–97, 1971.

[30] Emil Julius Gumbel. Statistical theory of extreme values and some practical applications. *National Bureau of Standards Applied Mathematics Series*, 33, 1954.

[31] Douglas C Hamilton, G Gloeckler, FM Ipavich, W Stüdemann, B Wilken, and G Kremser. Ring current development during the great geomagnetic storm of february 1986. *Journal of Geophysical Research: Space Physics*, 93(A12):14343–14355, 1988.

[32] Linnea Hesslow, Ola Embréus, Adam Stahl, Tim C DuBois, Gergely Papp, Sarah L Newton, and Tünde Fülöp. Effect of partially screened nuclei on fast-electron dynamics. *Physical review letters*, 118(25):255001, 2017.

[33] G Holmén, B Svensson, and A Burén. Ion induced electron emission from polycrystalline copper. *Nuclear Instruments and Methods in Physics Research*, 185(1-3):523–532, 1981.

[34] JL Horwitz. Velocity filter mechanism for ion bowl distributions (bimodal conics). *Journal of Geophysical Research: Space Physics*, 91(A4):4513–4523, 1986.

[35] R Ilie, MW Liemohn, G Toth, N Yu Ganushkina, and LKS Daldorff. Assessing the role of oxygen on ring current formation and evolution through numerical experiments. *Journal of Geophysical Research: Space Physics*, 120(6):4656–4668, 2015.

[36] R Ilie, RM Skoug, P Valek, HO Funsten, and A Glocer. Global view of inner magnetosphere composition during storm time. *Journal of Geophysical Research: Space Physics*, 118(11):7074–7084, 2013.

[37] Raluca Ilie and Michael W Liemohn. The outflow of ionospheric nitrogen ions: A possible tracer for the altitude-dependent transport and energization processes of ionospheric plasma. *Journal of Geophysical Research: Space Physics*, 121(9):9250–9255, 2016.

[38] J Illgen, R Kirchner, and J Schulte. Duoplasmatron ion sources. *IEEE Transactions on Nuclear Science*, 19(2):35–47, 1972.

[39] Z Insepov, V Ivanov, S Jokela, and M Wetstein. Comparison of back-scattering properties of electron emission materials. Proceedings of 2011 Particle Accelerator Conference, New York, 2011.

[40] Raymond E Kaiser Jr, R Graham Cooks, George C Stafford Jr, John EP Syka, and Philip H Hemberger. Operation of a quadrupole ion trap mass spectrometer to achieve high mass/charge ratios. *International journal of mass spectrometry and ion processes*, 106:79–115, 1991.

[41] Margaret G Kivelson and Christopher T Russell. *Introduction to space physics*. Cambridge university press, 1995.

[42] D.M. Klumpar, E. Möbius, L.M. Kistler, M. Popecki, E. Hertzberg, K. Crocker, M. Granoff, Li Tang, C.W. Carlson, J. McFadden, B. Klecker, F. Eberl, E. Künneth, H. Kästle, M. Ertl, W.K. Peterson, E.G. Shelly, and D. Hovestadt. The time-of-flight energy, angle, mass spectrograph (teams) experiment for fast. *Space Science Reviews*, 98(1):197–219, 2001.

[43] Nobuyoshi Koshida and Masato Hosobuchi. Energy distribution of output electrons from a microchannel plate. *Review of scientific instruments*, 56(7):1329–1331, 1985.

[44] JU Kozyra, MW Liemohn, CR Clauer, AJ Ridley, MF Thomsen, JE Borovsky, JL Roeder, VK Jordanova, and WD Gonzalez. Multistep dst development and ring current composition changes during the 4–6 june 1991 magnetic storm. *Journal of Geophysical Research: Space Physics*, 107(A8):SMP–33, 2002.

[45] Scott E Kruger, Dalton D Schnack, and Carl R Sovinec. Dynamics of the major disruption of a diii-d plasma. *Physics of Plasmas*, 12(5):056113, 2005.

[46] G Le, JA Slavin, and RJ Strangeway. Space technology 5 observations of the imbalance of regions 1 and 2 field-aligned currents and its implication to the cross-polar cap pedersen currents. *Journal of Geophysical Research: Space Physics*, 115(A7), 2010.

[47] C Lemon, RA Wolf, TW Hill, S Sazykin, RW Spiro, FR Toffoletto, J Birn, and M Hesse. Magnetic storm ring current injection modeled with the rice convection model and a self-consistent magnetic field. *Geophysical research letters*, 31(21), 2004.

[48] WN Lennard, H Geissel, DP Jackson, and D Phillips. Electronic stopping values for low velocity ions ($9 < z1, < 92$) in carbon targets. *Nuclear Instruments and Methods in Physics Research Section B: Beam Interactions with Materials and Atoms*, 13(1-3):127–132, 1986.

[49] B Leskovar. Microchannel plates. *Physics Today*, 30:42–49, 1977.

[50] J Liao, LM Kistler, CG Mouikis, Berndt Klecker, I Dandouras, and J-C Zhang. Statistical study of o+ transport from the cusp to the lobes with cluster codif data. *Journal of Geophysical Research: Space Physics*, 115(A12), 2010.

[51] J Lienemann, D Blauth, S Wethekam, M Busch, H Winter, Peter Wurz, SA Fuselier, and E Hertzberg. Negative ion formation during scattering of fast ions from diamond-like carbon surfaces. *Nuclear Instruments and Methods in Physics Research Section B: Beam Interactions with Materials and Atoms*, 269(9):915–918, 2011.

[52] J Lindhard and M Scharff. Energy dissipation by ions in the kev region. *Physical Review*, 124(1):128, 1961.

[53] Jens Lindhard, Morten Scharff, and Hans E Schiøtt. *Range concepts and heavy ion ranges*. Munksgaard Copenhagen, 1963.

[54] Horst W Loeb. Plasma-based ion beam sources. *Plasma physics and controlled fusion*, 47(12B):B565, 2005.

[55] Alexander Makarov, Eduard Denisov, Alexander Kholomeev, Wilko Balschun, Oliver Lange, Kerstin Strupat, and Stevan Horning. Performance evaluation of a hybrid linear ion trap/orbitrap mass spectrometer. *Analytical chemistry*, 78(7):2113–2120, 2006.

[56] Raymond E March. An introduction to quadrupole ion trap mass spectrometry. *Journal of mass spectrometry*, 32(4):351–369, 1997.

[57] BH Mauk, JB Blake, DN Baker, JH Clemmons, GD Reeves, Harlan E Spence, SE Jaskulek, CE Schlemm, LE Brown, SA Cooper, et al. The energetic particle detector (epd) investigation and the energetic ion spectrometer (eis) for the magnetospheric multiscale (mms) mission. *Space Science Reviews*, 199(1-4):471–514, 2016.

[58] JP McCollough, JL Gannon, DN Baker, and M Gehmeyr. A statistical comparison of commonly used external magnetic field models. *Space Weather*, 6(10), 2008.

[59] A Mertens and H Winter. Energy transfer from fast atomic projectiles to a crystal lattice under channeling conditions. *Physical review letters*, 85(13):2825, 2000.

[60] James S Milnes and J Howorth. Picosecond time response characteristics of microchannel plate pmt detectors. In *26th International Congress on High-Speed Photography and Photonics*, volume 5580, pages 730–741. International Society for Optics and Photonics, 2005.

[61] CG Mouikis, LM Kistler, G Wang, and Y Liu. Background subtraction for the cluster/codif plasma ion mass spectrometer. *Geoscientific Instrumentation, Methods and Data Systems*, 3(1):41–48, 2014.

[62] Alankrita Isha Mrigakshi. Study and test of micro-channel plates used in the dual ion spectrometer of the mms mission by nasa, 2008.

[63] M Nosé, S Taguchi, K Hosokawa, SP Christon, RW McEntire, TE Moore, and MR Collier. Overwhelming o+ contribution to the plasma sheet energy density during the october 2003 superstorm: Geotail/epic and image/lena observations. *Journal of Geophysical Research: Space Physics*, 110(A9), 2005.

[64] Aileen O'Mahony, Christopher A Craven, Michael J Minot, Mark A Popecki, Joseph M Renaud, Daniel C Bennis, Justin L Bond, Michael E Stochaj, Michael R Foley, Bernhard W Adams, et al. Atomic layer deposition of alternative glass microchannel plates. *Journal of Vacuum Science & Technology A: Vacuum, Surfaces, and Films*, 34(1):01A128, 2016.

[65] Sae-Hoon Park and Yu-Seok Kim. Simulation study on duoplasmatron with optimization of ion beam extraction system. *IEEE Transactions on Plasma Science*, 45(6):955–958, 2017.

[66] R Pfaff, C Carlson, J Watzin, D Everett, and T Gruner. An overview of the fast auroral snapshot (fast) satellite. In *The FAST Mission*, pages 1–32. Springer, 2001.

[67] C Pollock, T Moore, A Jacques, J Burch, U Gliese, Y Saito, T Omoto, L Avanov, A Barrie, V Coffey, et al. Fast plasma investigation for magnetospheric multiscale. *Space Science Reviews*, 199(1-4):331–406, 2016.

[68] MA Popecki, B Adams, CA Craven, T Cremer, MR Foley, A Lyashenko, A O'Mahony, MJ Minot, M Aviles, JL Bond, et al. Microchannel plate fabrication using glass cap-

illary arrays with atomic layer deposition films for resistance and gain. *Journal of Geophysical Research: Space Physics*, 121(8):7449–7460, 2016.

[69] NR Rajopadhye, SV Bhoraskar, and D Chakravorty. Electron emissive properties of pb and bi containing glasses. *Journal of non-crystalline solids*, 105(1-2):179–184, 1988.

[70] Ranjan Ramachandra. A study of helium ion induced secondary electron production. 2009.

[71] Balveer S Rathore, Dinesh C Gupta, and Subhash C Kaushik. Effect of solar wind plasma parameters on space weather. *Research in Astronomy and Astrophysics*, 15(1):85, 2015.

[72] H Reme, C Aoustin, JM Bosqued, I Dandouras, B Lavraud, JA Sauvaud, A Barthe, J Bouyssou, Th Camus, O Coeur-Joly, et al. First multispacecraft ion measurements in and near the earth's magnetosphere with the identical cluster ion spectrometry (cis) experiment. In *Annales Geophysicae*, volume 19, pages 1303–1354, 2001.

[73] H. Rème, J. M. Bosqued, E. Möbius, K. Crocker, M. Granoff, L. M. Kistler, M. Popecki, D. Hovestadt, B. Klecker, G. Paschmann, M. Scholer, C. W. Carlson, D. W. Curtis, and et al. *The Cluster Ion Spectrometry (CIS) Experiment*, pages 303–350. Springer Netherlands, Dordrecht, 1997.

[74] SM Ritzau and RA Baragiola. Electron emission from carbon foils induced by kev ions. *Physical Review B*, 58(5):2529, 1998.

[75] P Roncin, J Villette, JP Atanas, and H Khemliche. Energy loss of low energy protons on lif (100): surface excitation and h- mediated electron emission. *Physical review letters*, 83(4):864, 1999.

[76] Jørgen Schou. Transport theory for kinetic emission of secondary electrons from solids. *Physical Review B*, 22(5):2141, 1980.

[77] RWj Schunk and WJ Raitt. Atomic nitrogen and oxygen ions in the daytime high-latitude f region. *Journal of Geophysical Research: Space Physics*, 85(A3):1255–1272, 1980.

[78] Jae C Schwartz, Michael W Senko, and John EP Syka. A two-dimensional quadrupole ion trap mass spectrometer. *Journal of the American Society for Mass Spectrometry*, 13(6):659–669, 2002.

[79] Chuan-Chou Shen, R Lawrence Edwards, Hai Cheng, Jeffrey A Dorale, Rebecca B Thomas, S Bradley Moran, Sarah E Weinstein, and Henrietta N Edmonds. Uranium and thorium isotopic and concentration measurements by magnetic sector inductively coupled plasma mass spectrometry. *Chemical Geology*, 185(3-4):165–178, 2002.

[80] Oswald HW Siegmund, Camden Ertley, J Vallerga, and S Ryan. High speed large format photon counting microchannel plate imaging sensors. In *Proceedings of the Advanced Maui Optical and Space Surveillance Technologies Conference*, volume 94, page 94, 2015.

[81] PC Snijders, LPH Jeurgens, and WG Sloof. Structure of thin aluminium-oxide films determined from valence band spectra measured using xps. *Surface science*, 496(1-2):97–109, 2002.

[82] Dalton T Snyder, Wen-Ping Peng, and R Graham Cooks. Resonance methods in quadrupole ion traps. *Chemical Physics Letters*, 668:69–89, 2017.

[83] EJ Sternglass. Theory of secondary electron emission by high-speed ions. *Physical Review*, 108(1):1, 1957.

[84] James R Stevenson and Eugene B Hensley. Thermionic and photoelectric emission from magnesium oxide. *Journal of Applied Physics*, 32(2):166–172, 1961.

[85] Sikandar H Tamboli, Chandra Bhal Singh, RB Patil, Vijaya Puri, RK Puri, Vandana Singh, and Meng Fan Luo. Enhanced secondary electron emission yield of mgo thin films by vapor chopping technique for plasma display panels. *Journal of Nanoelectronics and Optoelectronics*, 6(2):156–161, 2011.

[86] JG Timothy and RL Bybee. Preliminary results with microchannel array plates employing curved microchannels to inhibit ion feedback. *Review of Scientific Instruments*, 48(3):292–299, 1977.

[87] Andris Vaivads, A Retinò, J Soucek, Yu V Khotyaintsev, F Valentini, CP Escoubet, O Alexandrova, Mats André, SD Bale, M Balikhin, et al. Turbulence heating observer–satellite mission proposal. *Journal of Plasma Physics*, 82(5), 2016.

[88] Zeke Insepov" Valentin Ivanov. Numerical simulation of the micro-channel plates". Argonne National Laboratory", 2009.

[89] Frank Vanhaecke, Luc Moens, Richard Dams, and Philip Taylor. Precise measurement of isotope ratios with a double-focusing magnetic sector icp mass spectrometer. *Analytical chemistry*, 68(3):567–569, 1996.

[90] Allen Leoraj Victor. *Design and Utilization of a Top Hat Analyzer for Hall Thruster Plume Diagnostics*. PhD thesis, Ph. D. Dissertation, 2006.

[91] Feifei Wang, Fan Zhou, Jinshu Wang, Wei Liu, Quan Zhang, and Qiao Yin. Characterization of mgo/al 2 o 3 composite film prepared by dc magnetron sputtering and its secondary electron emission properties. *Journal of Electronic Materials*, 47:4116–4123, 2018.

[92] S Wang, LM Kistler, CG Mouikis, Y Liu, and KJ Genestreti. Hot magnetospheric o+ and cold ion behavior in magnetopause reconnection: Cluster observations. *Journal of Geophysical Research: Space Physics*, 119(12):9601–9623, 2014.

[93] Shan Wang, Lynn M Kistler, Christopher G Mouikis, and Steven M Petrinec. Dependence of the dayside magnetopause reconnection rate on local conditions. *Journal of Geophysical Research: Space Physics*, 120(8):6386–6408, 2015.

[94] BA Whalen, JR Burrows, AW Yau, EE Budzinski, AM Pilon, I Iwamoto, K Marubashi, S Watanabe, H Mori, and E Sagawa. The suprathermal ion mass spectrometer (sms) onboard the akebono (exos-d) satellite. *Journal of geomagnetism and geoelectricity*, 42(4):511–536, 1990.

[95] RM Winglee, D Chua, M Brittnacher, GK Parks, and Gang Lu. Global impact of ionospheric outflows on the dynamics of the magnetosphere and cross-polar cap potential. *Journal of Geophysical Research: Space Physics*, 107(A9):SMP–11, 2002.

[96] Helmut Winter. *Kinetic Electron Emission for Grazing Scattering of Atoms and Ions from Surfaces*, pages 113–151. Springer Berlin Heidelberg, Berlin, Heidelberg, 2007.

[97] Joseph Ladislas Wiza. Microchannel plate detectors. *Nuclear Instruments and Methods*, 162(1-3):587–601, 1979.

[98] Masatoshi Yamauchi, Iannis Dandouras, and Peter Rathsman. Nitrogen ion tracing observatory (nitro) esa's m-class call. In *EGU General Assembly Conference Abstracts*, volume 17, 2015.

[99] AW Yau and BA Whalen. Auroral ion composition during large magnetic storms. *Canadian journal of physics*, 70(7):500–509, 1992.

[100] Mohsen Yazdanmehr, Saeid Jalali Asadabadi, Abolghasem Nourmohammadi, Majid Ghasemzadeh, and Mahmood Rezvanian. Electronic structure and bandgap of γ-al 2 o 3 compound using mbj exchange potential. *Nanoscale research letters*, 7(1):488, 2012.

[101] DT Young, H Balsiger, and J Geiss. Correlations of magnetospheric ion composition with geomagnetic and solar activity. *Journal of Geophysical Research: Space Physics*, 87(A11):9077–9096, 1982.

[102] DT Young, RP Bowman, RK Black, TL Booker, PJ Casey, GJ Dirks, DR Guerrero, KE Smith, JH Waite, and MP Wüest. Miniaturized optimized smart sensor (moss) for space plasma diagnostics. *GEOPHYSICAL MONOGRAPH-AMERICAN GEOPHYSICAL UNION*, 102:313–318, 1998.

[103] AN Zavilopulo, FF Chipev, and OB Shpenik. Ionization of nitrogen, oxygen, water, and carbon dioxide molecules by near-threshold electron impact. *Technical physics*, 50(4):402–407, 2005.

[104] James F Ziegler, Matthias D Ziegler, and Jochen P Biersack. *SRIM: the stopping and range of ions in matter*. Cadence Design Systems, 2008.

[105] James F Ziegler, Matthias D Ziegler, and Jochen P Biersack. Srim–the stopping and range of ions in matter (2010). *Nuclear Instruments and Methods in Physics Research Section B: Beam Interactions with Materials and Atoms*, 268(11-12):1818–1823, 2010.